İSTANBUL TECHNICAL UNIVERSITY ★ INSTITUTE OF SCIENCE AND TECHNOLOGY

CORRELATING FIBER DISPERSION, RHEOLOGY, AND MECHANICAL PERFORMANCE FOR FIBER-REINFORCED CEMENT-BASED MATERIALS

Ph.D. Thesis by

Nilüfer Özyurt, M.Sc.

(501002106)

Date of submission : 6 October 2005

Date of defence examination: 21 February 2006

Supervisor (Chairman): Prof. Dr. Mehmet Ali Taşdemir
Co-Supervisor : Prof. Dr. Surendra P. Shah (Northwestern U.)

Members of the Examining Committee : Prof. Dr. Turan Özturan (B.Ü.)
Prof. Dr. Halit Yaşa Ersoy (M.S.Ü.)
Prof. Dr. Abdurrahman Güner (T.Ü.)
Prof. Dr. Saim Akyüz (İ.T.Ü)
Doç. Dr. Yılmaz Akkaya (İ.T.Ü)

FEBRUARY 2006

FOREWORD

First, I would like to thank my advisors, Professor Mehmet Ali Taşdemir and Professor Surendra P. Shah for being not only advisors, but also mentors during my graduate studies. They have guided me through the academic path with their support and experience.

I would also like to thank Professor Thomas Mason of Northwestern University and Dr. Leta Yar-Li Woo for all of our collaborations during my study.

I want to express my special thanks to Prof. Canan Taşdemir for her continiuous help and support during my academic life. I also want to thank the professors of ITU Structural Materials Department for teaching and sharing their experiences.

Special thanks to my close friend, ally and colleague Dr. Katherine Kuder. I was very lucky to have her with me during my study at the Center for Advanced Cement-Based Materials (ACBM). I have very much enjoyed all of our scientific discussions, coffee breaks, dinner and drink conversations.

I want to gratefully recognize ACBM administrative team - Richard Garza and Marcia Hilliard - for not only helping me out with every little administrative detail, but also for being very good friends. It was great to have them at ACBM office. Thank you! I would also like to mention Richard's responsibility for my addiction to coffee and wine.

I wish to thank the staff of both ACBM and Istanbul Technical University. Special thanks to John Chirayil and Steve Albertson for patiently helping me with my experiments during my stay at Northwestern. They have also cheered me up with lively conversations in the lab.

It is very important to have smiling faces at graduate school. Thanks to my office mates, and colleagues at both Northwestern and Istanbul Technical University for their cheerful faces and the help that they provided. Thanks to Nathan Tregger, Dave Ey, Dave Corr, Raissa Douglas, Zhihui Sun, Thomas Voigt, Edward Mu, Van Bui, Paramita Mondal, Jae-Suk Ryou, Ivan Vlahinic, Priscilla Cynthia Fonseca, Jean Juste Jules Mbele, Yanhua Ye, Supaporn Wansom, Sandy Yoon, Melissa Mendez, Amedeo Gregori, David Jolivet, Michele Cyr, Brian Ingram, Yılmaz Akkaya, Özkan Şengül, Hakan N. Atahan, Burcu Akçay, Şafak Ağar, Bekir Pekmezci, Anıl Doğan, Cengiz Şengül and Özgür Ekincioğlu.

I would like to especially recognize those who made my staying in the United States particularly fun with their friendship. Thanks to Deniz Aray, Umut Aytekin, Murat Güvendiren, Katherine Kuder, Richard and Kim Garza, Marcia and Andre Hilliard, Aalia Thobani, Dorothy Shah, Moreen and Jim Jacobs for sharing this experience with me. I'm grateful for all they have done for me.

Financial support of The Scientific and Technological Research Council of Turkey (TÜBİTAK), İstanbul Technical University, Northwestern University and Tinçel Cultural Foundation is gratefully appreciated.

I dedicate this thesis to my family. None of this would have been possible without them. Thanks to my father and my mother, Ahmet and Hikmet Özyurt, for their endless love and support. I will never fear of anything as long as you are with me. Thanks to my beloved sister, Nigar, and her husband, Cem, and my dear brother, Sait, for being my very close friends, for always loving, listening, and watching over me. I'm very lucky to have them all.

October, 2005 **Nilüfer Özyurt**

CONTENTS

LIST OF FIGURES

Page No

LIST OF TABLES

CORRELATING FIBER DISPERSION, RHEOLOGY, AND MECHANICAL PERFORMANCE FOR FIBER-REINFORCED CEMENT-BASED MATERIALS

SUMMARY

Fibers are used to enhance various properties of cement-based materials such as ductility, toughness, flexural strength and shear strength, along with reduced shrinkage cracking, and enhanced fatigue and impact resistances. With these improvements in mechanical performance, fiber-reinforced concrete (FRC) materials are increasingly employed in a wide variety of applications such as pavements, overlays, patching, floor slabs, hydraulic structures, thin shells, tunnel linings, refractory materials, etc. These applications are mostly semi-structural. Recently, it has been shown that fiber-reinforced cement-based materials can be employed for further load-carrying applications such as bridges or high rise buildings (curtain walls). Fibers have also been used as replacement of shear reinforcement in structural members. However, the use of FRC is still limited in spite of the advantageous features of fiber reinforcement. Further research is required for a comprehensive understanding and a more widespread use of fiber-reinforced cement-based materials. Quality control and quality assurance should be provided. New non-destructive techniques should be developed to monitor material properties in both the fresh and hardened states.

Considering these factors, a comprehensive study is conducted in this thesis to better understand the material properties of FRCs in the fresh and hardened states. The challenges in this thesis are threefold.

1) *To develop a non-destructive technique* to monitor various fiber dispersion issues in the fresh and hardened states of FRCs.
2) *To design, build and utilize a rheometer* that is specifically suited to evaluate the flow behavior of stiff fiber-reinforced cement-based materials.
3) *To find a relationship between the fresh and hardened state properties* by using the methods and equipments mentioned above.

A short review of contents of this thesis is given below:

A non-destructive technique - Alternating Current – Impedance Spectroscopy (AC-IS) – is employed to monitor fiber dispersion in both the fresh and hardened states of FRCs. AC-IS is found to be sensitive to various dispersion phenomena. First, AC-IS is used on small-scale fiber-reinforced cement-based specimens to understand the ability of AC-IS for monitoring different dispersion problems such as fiber orientation, fiber segregation and fiber clumping. Various experimental set-ups are used. An intrinsic conductivity approach is applied to define dispersion

characteristics from experimental data. Techniques of image analysis are employed to understand the extent to which AC-IS predicts fiber dispersion issues. The results of the two methods are compared to understand the ability of AC-IS to monitor different dispersion issues.

A large-scale application of AC-IS is made on a structural, pre-cast self compacting FRC beam, which was supplied by a precast concrete company. Fiber orientation in the beam is studied using AC-IS and image analysis, respectively. Results are compared. Preferred orientation of fibers in the plane vertical to the casting direction is detected and splitting tensile tests and three-point bending tests are performed to understand the effect of fiber orientation on the mechanical performance of the beam. Mechanical performance is found to be affected by the preferred orientation of fibers.

A rheometer with parallel plate configuration is designed and experimentally verified to study the fresh state properties of fiber-reinforced stiff cementitious materials (Rheometer design is done by Dr. Edward Mu). A plexiglass wall is included in the parallel-plate configuration to prevent test material from flowing away. The wall effect is taken into account using an existing rheological characterization model. The ability of the parallel-plate rheometer to evaluate flow behavior is verified using a commercial rheometer, a standardized high viscosity oil and values that are reported in the literature. Experiments are conducted to study the effects of water/cement ratio, sand content and fiber volume content on the rheological characteristics of cement-based materials. The Bingham model is used to calculate the rheological parameters from experimental data. Results are discussed and a comparative analysis conducted with other methods currently used to characterize flow behavior.

Finally, a series of experiments are performed to correlate the fresh and hardened state properties of FRCs by means of fiber dispersion. FRC specimens are cast using different mix designs and vibration is applied. Vibration times are varied to understand the effects of vibration on fiber segregation. Various concrete mixes are studied. An SCC mix is cast to compare conventional concrete and SCC by means of fiber segregation. Vertical fiber distributions are evaluated by cutting fresh specimens (immediately after intial set) into slices, washing the fibers out and then quantifying the amount of fibers in each section. AC-IS is used for the hardened state measurements. Splitting tensile tests are done to study the effects of segregation on mechanical performance. Fiber content distribution, matrix-normalized conductivity and splitting tensile strength profiles of specimens are plotted. Similar tendencies are observed, suggesting that fiber segregation in FRCs can be monitored using AC-IS. To correlate the fresh and hardened state properties by means of fiber dispersion, rheological parameters of the mixes are measured using the custom-built parallel-plate rheometer. Yield stress and viscosity values are calculated for cement pastes of each concrete design. A good correlation is found between fiber content distribution, mechanical performance and fresh state properties.

LİF DONATILI ÇİMENTO ESASLI MALZEMELERDE, LİF DAĞILIMI, REOLOJİ VE MEKANİK BAŞARIMLILIĞIN KORELASYONU

ÖZET

Lifler, çimento esaslı malzemelerde süneklik, enerji yutma kapasitesi, eğilme dayanımı ve kayma dayanımlarının arttırılması, rötre çatlaklarının azaltılması, yorulma ve çarpma dayanımlarının arttırılması gibi birçok özeliğin iyileştirilmesi için kullanılırlar. Mekanik davranışta elde edilen bu gelişmelerle, lif donatılı çimento esaslı malzemeler yol betonları, yüzey kaplamaları ve onarımları, yer döşemeleri, su yapıları, ince kabuk yapılar, tüneller, ve yangına dayanıklı malzemeler gibi birçok alanda yaygın bir şekilde kullanılmaktadırlar. Yakın zamanda, lif donatılı çimento esaslı malzemelerden köprüler ve yüksek katlı binalar (perde duvarlar) gibi daha fazla taşıyıcılık gerektiren uygulamalarda faydalanılabileceği gösterilmiştir. Lifler, ayrıca yapısal elemanlarda kayma donatısı yerine de kullanılmaktadır. Lifler ile elde edilen bütün avantajlara rağmen lifli beton uygulamaları halen sınırlıdır. Lif donatılı çimento esaslı malzeme davranışının daha iyi anlaşılması ve daha yaygın kullanımın sağlanması için ileri düzeyde araştırmalar yapılması gerekmektedir. Kalite kontrol ve kalite güvencesi sağlanabilmelidir. Malzeme özeliklerinin taze ve sertleşmiş halde kontrolü için yeni ve tahribatsız deney metodları geliştirilmelidir.

Bu tezde, yukarıda belirtilen etkenler göz önünde tutularak, lif donatılı malzeme davranışının taze ve sertleşmiş halde daha iyi anlaşılabilmesi için kapsamlı bir çalışma yürütüldü. Bu tez çalışması ile hedeflenen yenilikler üç başlık altında verilebilir:

1) Lifli betonlarda, taze ve sertleşmiş halde farklı lif dağılımı problemlerinin ölçümü için *tahribatsız bir deney metodunun geliştirilmesi*.
2) Özellikle, yüksek viskoziteli lif donatılı çimento esaslı malzemelerin reolojik özeliklerinin ölçümü ve değerlendirilmesi için *yeni bir reometrenin tasarlanması, inşaa edilmesi ve kullanılması.*
3) Yukarıda bahsedilen yöntem ve ekipmanların kullanımı ile *taze ve sertleşmiş beton özeliklerinin ilişkilendirilmesi*

Aşağıda bu tez çalışmasının içeriğinin kısa bir özeti verilmektedir:

Lif donatılı betonlarda, taze ve sertleşmiş halde lif dağılımının ölçülmesi için, tahribatsız bir deney metodu, Alternatif Akım – Empedans Spektroskopi (AA-ES) kullanıldı. Önce, AA-ES'in lif yönlenmesi, segregasyonu ve topaklanması gibi farklı problemlerin tesbit edilmesi amacıyla kullanılabilirliğinin anlaşılması için küçük boyutlu, lif donatılı çimento esaslı numuneler üzerinde çeşitli deney düzenekleri kullanılarak ölçümler yapıldı. Elde edilen deney verilerinden lif dağılımı karakteristiklerinin belirlenebilmesi için bünyesel iletkenlik yaklaşımı kullanıldı. Ardından, AA-ES'in lif dağılımı problemlerini ne doğrulukta tesbit edebildiğinin

ölçülebilmesi için imaj analizi tekniklerinden faydalanıldı. İki metod ile elde edilen sonuçlar AA-ES'in lif dağılımının karakterize edilebilmesi için kullanılabilirliğinin anlaşılabilmesi için karşılaştırıldı.

AA-ES'in endüstriyel bir uygulaması, bir prekast beton firması tarafından sağlanan, kendiliğinden yerleşen lif donatılı betondan imal edilmiş yapı kirişi üzerinde gerçekleştirildi. Kiriş içerisindeki liflerin yönlenmesi AA-ES ve imaj analizleri kullanılarak ölçüldü ve sonuçlar karşılaştırıldı. Liflerin betonun döküm yönüne dik düzlemde yönlendiği tesbit edildi ve lif yönlenmesinin mekanik davranış üzerindeki etkilerinin anlaşılabilmesi için yarma deneyleri ve 3 noktalı eğilme deneyleri yapıldı. Mekanik özeliklerin liflerin yönlenmesinden olumsuz yönde etkilendiği görüldü.

Yüksek viskozitede, lif donatılı malzemelerin taze halde özeliklerinin belirlenebilmesi için, paralel diskli bir reometre tasarlandı ve reometre ile elde edilen sonuçlar deneysel olarak doğrulandı. (Reometrenin tasarımı Dr. Bin Mu tarafından gerçekleştirildi). Malzemenin deney sırasında diskler arasından akmasını engellemek için pleksiglass bir duvar kullanıldı. Reolojik özeliklerin karakterizasyonu için uygulanan bir model kullanılarak duvar etkisi hesaplara dahil edildi. Paralel diskli reometre ile elde edilen sonuçların kontrolü için ticari bir reometreden elde edilen sonuçlar, standard kalibrasyon yağı ve literatürde verilmiş değerler kullanıldı. Su/çimento oranı, kum miktarı ve lif miktarının çimento esaslı malzemelerin reolojik özelikleri üzerindeki etkilerinin araştırılması için deneyler yapıldı. Deneysel verilerden reolojik parametrelerin hesaplanabilmesi için Bingham modeli kullanıldı. Sonuçlar değerlendirildi ve akma davranışının karakterize edilmesi için kullanılan diğer bazı metodlar ile karşılaştırmalı analizler yapıldı.

Son olarak, lif donatılı betonlarda taze ve sertleşmiş hal özeliklerinin lif dağılımı karakteristiklerinden faydalanılarak birbirine ilişkilendirilmesi amacıyla bir seri deney yapıldı. Farklı beton tasarımları kullanılarak lif donatılı beton numuneler üretildi ve bu numunelere vibrasyon uygulandı. Vibrasyonun liflerin segregasyonu üzerindeki etkilerinin anlaşılması için farklı vibrasyon süreleri uygulandı. Normal beton ile kendiliğinden yerleşen betonun lif segregasyonu yönünden karşılaştırılması amacıyla kendiliğinden yerleşen beton üretildi. Numunelerin taze halde parçalara kesilmesi (priz başladıktan hemen sonra), kesilen parçalardan beton matrisinin yıkanarak liflerin çıkarılması ve her parçadaki lif miktarının ölçülmesi suretiyle liflerin dikey yöndeki dağılımları tesbit edildi. Sertleşmiş haldeki lif dağılımına bakılması için AA-ES kullanıldı. Segregasyonun mekanik davranış üzerindeki etkilerinin araştırılması için yarma testleri yapıldı. Numunelerin lif içeriği dağılımı, matrise göre normalize edilmiş iletkenlik değerleri dağılımı ve yarma dayanımı dağılımları grafik olarak elde edildi. AA-ES'in lif donatılı betonlarda, lif segregasyonunun tesbiti için kullanılabileceğini gösterir şekilde benzer dağılımlar elde edildi. Taze ve sertleşmiş haldeki özeliklerin lif dağılımı kullanılarak ilişkilendirilmesi amacıyla kullanılan çimento hamurlarının reolojik özelikleri paralel diskli reometre kullanılarak ölçüldü. Bütün beton karışımları için çimento hamurlarının akma gerilmesi ve viskozite değerleri elde edildi. Lif içeriği dağılımı, mekanik performans, ve taze hal özelikleri arasında kuvvetli bir ilişki olduğu görüldü.

1. INTRODUCTION

The use of fiber reinforcement in the concrete industry began in the early 1960's, and has steadily developed along with our understanding of structure-property relationships in fiber-reinforced concretes (FRCs). The major contribution of fibers is to significantly improve the weak tensile properties of the cement/concrete matrix. The addition of fibers leads to improvements in ductility, toughness, and flexural strength[1-3]. Enhanced shear strength [4], reduced shrinkage cracking [5-7], improved fatigue resistance, and greater impact/blast resistances [1, 8] have also been attributed to the addition of fibers. Various researchers have confirmed that the relative effectiveness of fibers at performing these tasks is dependent upon the degree of fiber dispersion throughout the material [9-12]. The degree of dispersion affects both the fresh and hardened state properties of concrete. Improper dispersion can negatively impact the flow characteristics of fresh concrete, and poorly dispersed fibers in the hardened state can severely limit the otherwise beneficial effects of fibers.

The fresh state properties (rheology) of cementitious materials are important, either for the resulting performance, or for ease of placement during construction. Unfortunately, the study of the fresh concrete structure is highly complicated due to the large variations in the material properties and testing artifacts. Many researchers have emphasized that there is no definite method to measure the fresh state properties [13]. With the addition of fibers, the fresh concrete structure becomes more complex, making the determination of the rheological parameters more difficult. Considering the wide range of materials and other variables, an optimization of the fresh state properties of FRC is needed to achieve good mechanical performance and durability. An optimization of FRC performance can be achieved by taking into consideration the interactions between rheology and fiber dispersion.

The overall goal of this study is to find a correlation between rheology, fiber dispersion and the mechanical performance of FRCs, connecting fresh state material properties to the hardened state properties. For this purpose a comprehensive study on rheology, fiber dispersion and mechanical performance of FRCs is conducted.

2. LITERATURE REVIEW

In this section a short review of the literature related to this research is given. Fiber dispersion and rheology are discussed under two sections.

2.1 Fiber Dispersion

Effectiveness of fiber reinforcement is highly dependent on fiber dispersion characteristics [10]. Monitoring and control of fiber dispersion characteristics is crucial for material performance.

Crack formation in the cementitious materials starts from the micro-level with fine discontinuous microcracks distributed throughout the material. These cracks coalesce to form larger cracks with increasing stress and finally the matrix fails when the ultimate stress is reached. The main role of fibers is to control the initiation, growth and coalescence of these cracks. Fibers control the cracks from the micro to the macro scale, depending on the size of fibers, by bridging cracks and delaying the sudden formation of larger cracks by coalescence [6]. Composite performance can be directly related to the effectiveness of fibers to control cracks. For example, Naaman [14] recently proposed a performance-based classification of FRCs based upon multiple cracking ability. In the case of random dispersion fiber-free areas will be minimized and material performance will be uniform throughout. Fiber-free areas in poorly dispersed FRCs can act as flaws; crack initiation and propagation is favored in these areas, leading to reduced strength and toughness. Thus, the control and characterization of fiber dispersion characteristics is important to obtain good mechanical performance.

Various techniques have been employed to characterize fiber dispersion in composites. Chermant and co-workers [15] used X-rays on iron ribbon fibers to establish their locations within the matrix. They suggested a covariance function of nearest-neighbor fibers to characterize their distribution. Yang [16] and Rapoport [17] have employed wash-out tests to inspect fiber dispersion. Akkaya [18] and

Lawler [19] used SEM/optical microscopy to locate short fibers and then applied statistical analysis to quantify fiber dispersion, with good results.

All these methods are valid but the processes are either destructive or/and time -and labor- intensive. Furthermore, they are not suited for inspection and quality control of fiber dispersion during mixing or in the fresh state. Over the past decade there has been increased interest in the electrical properties of fiber-reinforced cement-based materials. Various researchers showed that DC and Alternating Current-Impedance Spectroscopy (AC-IS) measurements can be employed to monitor characteristics of cement-based materials [20-23]. Recently Torrents and co-workers showed that the addition of conductive fibers (steel, carbon) to cement matrices results in unique "dual-cusp" behavior in plots of imaginary vs. real impedance, as measured by AC-IS [24, 25]. In this study fiber dispersion will be studied using AC-IS and Image Analysis.

2.1.1 AC-impedance spectroscopy

AC-IS is a non-destructive testing technique, which is widely used in the last decades to characterize the microstructural properties of composites. This method basically measures certain electrical parameters of materials. The use of AC-IS to study material properties of cement-based materials shows considerable promise. It has been reported by many researchers that AC-IS can be used to characterize various assets of cement-based materials.

Christensen and his colleagues [26] used AC-IS to calculate permeability and diffisuvity of composite materials. For that purpose, they related the conductivity of cement paste to the volume fraction of porosity, the conductivity of the pore solution, and the interconnectivity of the porosity. They succesfully used these data to predict the ionic diffisuvity and water permeability of cementitious material.

Park and his colleagues [27] employed AC-IS for structural health monitoring of civil structures and they reported that impedance measurements can effectively be used to detect real-time damage in civil structures. They also investigated robustness of the method to changes in environmental conditions and found good results.

Dotelli and Mari [28] pointed out the possibility of using AC-IS to follow the evolution of the hydration process of the cement-based materials. They have also used x-ray diffraction and thermogravimetry to confirm the ability of IS to non-destructively detect the evolution of the cement paste hydration.

Gu et al. [29] employed AC-IS to study micro-cracking of cement systems under compressive loading and showed that AC-IS is sensitive to the micro-cracking of cement-based materials. They also employed IS to investigate the features of transition zone in cement-based materials. They used silica fume, slag, fly ash, and latex aggregate coatings to enhance the microstructure of the transition zone and utilized the features of AC-IS to describe the density of the transition zone. They reported that the AC-IS has the potential to be used to study the microstructural properties of the transition zone in cementitious materials.

Peled et al. [30] also studied electrical and mechanical property relationship of extruded fiber-reinforced specimens under tensile loading and found a strong relationship.

In this study AC-IS is employed to characterize dispersion properties of FRCs.

2.1.2 Image analysis

Image analysis is a fundamental method to study micro-structural characteristics of various materials. It can be employed to investigate fiber-dispersion characteristics of FRCs. The method is based on obtaining micrographs of sections to study dispersion of fibers. Two dimensional or three dimensional micrographs of specimens can be taken and analyzed using appropriate equipment and image analysis program.

Stroeven and Shah [31] used radiography image analysis to investigate fiber distribution characteristics. They have reported a strong relation between the major crack locations and fiber density in the FRC specimens.

Clarke and Eberhardt used confocal laser scanning microscopy for scanning of glass fiber-reinforced polymer systems [32]. Mlekusch [33] used reflected light microscopy and scanning electron microscopy (SEM) to obtain micrographs of 2-D cross-sections.

Nowadays it is possible to obtain 3-D information of materials using X-Ray Computed Tomography (CT) [34]. Benson et al. [35] employed x-ray computed tomography for non-destructive evaluation of fiber dispersion. They pointed out that the available scanners are not capable of resolving individual small fibers. Thus, they suggested the use of contour plots of x-ray absorption density to analyze fiber dispersion characteristics.

X-Ray tomography is a good method to study fiber dispersion characteristics of FRC materials because it is non-destructive and gives 3-D information. Unfortunately, only very small specimens can be examined due to resolution-related concerns as mentioned above and methods for analyzing data are not well established.

Various methods exist to describe fiber dispersion characteristics from experimental results. Akkaya [18] used K, G and F functions of statistical point processes to describe various parameters of fiber dispersion such as fiber clumping and fiber-free areas from experimental data.

Storeven [36] used stereological methods to model fiber dispersions in cementitious systems. He employed first order stereology to estimate mechanical properties of cement-based materials.

For this study statistical point processes and second order orientation tensors are employed to describe fiber dispersion characteristics from experimental data. The details of the two methods are given in the next chapter.

2.2 Rheology

Rheologhy is defined as the science dealing with the deformation and flow of materials under stress [37] or simply the study of the flow behavior of fluids.

Viscosity and yield stress of materials are measured typically, to study the flow behavior. Viscosity (η) is an internal property of a fluid that offers resistance to flow and yield stress (τ_o) is the stress needed to be applied to material to initiate flow[13].

Fluids have different flow behaviors and they can be classified into two groups as Newtonian and Non-Newtonian fluids depending on flow behaviors. A newtonian fluid follows the equation below [38].

$$\tau = \eta(\Delta v / \Delta y) \qquad \textbf{(2.1)}$$

In this equation τ is the shear stress and Δv/Δy(γ) is the velocity gradient (shear rate). Water and oil are the most known newtonian fluids. There is a linear relationship between shear stress and shear rate, so the viscosity is a constant for Newtonian fluids.

A non-newtonian fluid doesn't follow the Eq.(2.1). The viscosity of a non-newtonian fluid changes depending on the shear rate. Non-newtonian fluids can be classified as time-independent and time-dependent.

The viscosity of time-independent fluids is dependent on temperature and shear rate but it doesn't change with time. Time independent non-newtonian fluids can be classified as shear thinning, shear thickening and plastic. Viscosity decreases with increasing shear rate in a shear thinning type of fluid and increases with increasing shear rate in a shear thickening type of fluid. Plastic fluid requires a threshold stress which is called yield stress before flow starts and after yield stress surpassed a linear relationship between shear stress and viscosity is seen. Bingham fluid is the most known example of plastic fluids. Flow behavior of fresh concrete is mostly modeled by using Bingham model. Figure 2.1 shows the shear stress versus velocity gradient curves of newtonian and non-newtonian fluids [38].

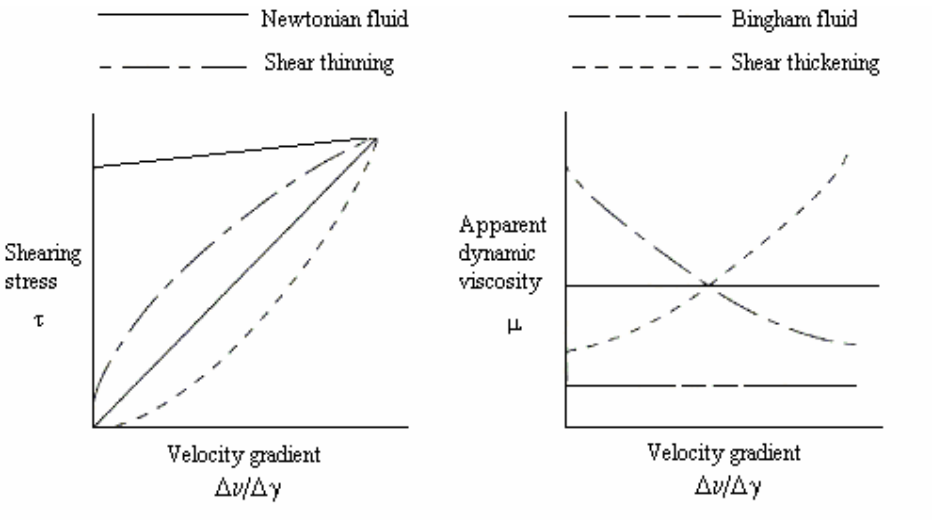

Figure 2.1: Shear stress vs. velocity gradient curves [38]

The viscosity of non-newtonian time dependent fluids is dependent on temperature, shear rate and time. So these fluids are very difficult to analyze. They are classified as thixotropic and rheopectic. Materials whose viscosity decreases time dependently at a certain shear rate are thixotropic and the materials whose viscosity increases time dependently are rheopectic.

Cement based materials shows thixotropic behavior. Figure 2.2 shows the typical shear stress versus time behavior for a cementitious material being sheared at a constant shear rate. Both a peak and equilibrium stresses are observed due to the thixotropic nature of the material. Under a constant shear rate there is a reversible time-dependent decrease in viscosity, which can be explained by the microstructural breakdown of the material [39]. Once the shear stress is removed, the microstructure rebuilds. Currently, measuring protocols are either based on the peak stress value, τ_{peak}, or the equilibrium stress value, $\tau_{equilibrium}$ [40].

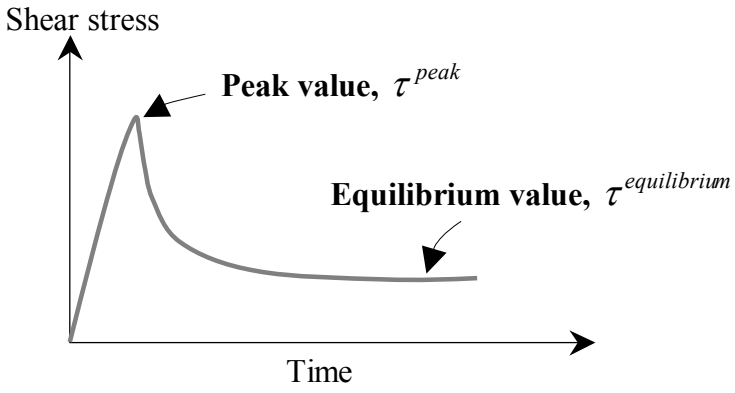

Figure 2.2: Peak and equilibrium values of shear stress at a constant shear rate.

Different models exist to describe the rheological characteristics of cement-based materials. The most common of these is the Bingham equation, and is given as:

$$\tau = \tau_0 + \mu_0 \dot{\gamma} \qquad \textbf{(2.2)}$$

where, τ is the shear stress applied to the material, τ_0 is the Bingham yield stress, μ_0 is the Bingham plastic viscosity and $\dot{\gamma}$ is the shear strain rate. Yield stress is typically defined as the force required to initiate flow and viscosity is the resistance to flow.

Some of the other models which were suggested to describe rheological characteristics of cement-based materials are Herschel-Bulkley [41], Vom Berg, Eyring [42], Casson, Ellis [43], Robertson-Stiff [44], and Atzeni [13].

Rheometers are used to measure the yield stress and viscosity of cementitous materials. A variety of rheometer types exist due to the wide range of materials being tested – cement paste, mortar and concrete, with varying compositions including fibers, mineral additives, admixtures and aggregates. Depending on the stiffness, maximum particle size, fiber length and solid particle concentration of the material being tested, different rheometers are appropriate. Rheometers can be classified as either commercial rheometers, such as Haake, or as custom-designed and built rheometers, including the BML and CEMAGREF-IMG (coaxial type configuration) [45, 46], BTRHEOM and a parallel plate configuration developed at the University of Illinois at Urbana-Champaign [47-49] or IBB and two-point [50-52].

Various researchers have studied the rheology of cementitious materials, using variety of rheometers, measuring protocols and materials. Unfortunately, the results from the different studies are not quantitatively comparable, although qualitative relationships can usually be found. Rheometer types, measuring protocols and materials all influence the results obtained. Plug flow, slip and sedimentation are problems often encountered with rheometers and can significantly influence rheological measurements. The extent to which these problems occur depends on the rheometer configuration used. Shear history also significantly affects the experimental results, due to the thixotropy of cement-based systems. Therefore, mixing and measuring protocols should be identical if repeatable test results are to be obtained.

In this study, a parallel plate rheometer is designed and built, specifically for stiff fiber-reinforced cementitious materials.

3. FIBER DISPERSION - METHODS OF ANALYSIS AND FUNDAMENTALS OF THE METHODS

3.1 Introduction

In this section, basics of the employed methods for fiber dispersion monitoring are discussed. In the 1st part of this section, AC-IS and dual arc behavior are introduced and explained. Intrinsic conductivity approach, which is the relation used to define dispersion characteristics is given. Different fiber dispersion issues are classified and the use of AC-IS for various applications is explained. Experimental set-ups are presented. Then the methods used to obtain dispersion characteristics from experimental data are given. Fractional intrinsic conductivities for characterization of fiber orientation, point-probe technique and matrix-normalized conductivity profiles for fiber segregation and dispersion factors for fiber clumping are employed.

In this study, image analyses are done to verify the results from AC-IS measurements. Therefore, in the 2nd part of this section, image analyses techniques used are introduced. Methods of statistical point processes are used to describe fiber clumping and second order orientation tensors are employed to describe fiber orientation.

3.2 Fiber Dispersion

3.2.1 AC – impedance spectroscopy (AC-IS) and dual arc behavior

Impedance (Z) is a measure of the total opposition to current flow in an alternating current circuit. It can be thought as the AC equivalent of resistance (R) in DC circuits. Resistance is the ratio of voltage to current. Impedance is a more general form of resistance. Impedance consists of the sum of resistance (R) and reactance (X) contributions. Reactance contributions may occur due to capacitive (X_C) and/or inductive (X_L) contributions. For a pure resistor Z=R. Impedance is time and frequency dependent and there is a phase difference (due to capacitive/inductive contributions) between applied voltage and output current as seen in Figure 3.1.

Therefore, Ohm's law for impedance takes the form Z(w)=V(t)/I(t), while it is R=V/I for resistance. In these equations, V is voltage, I is current, t stands for time and w for frequency. There are various ways to show impedance data. Nyquist plots are generally used to represent complex impedance data. Real part of the impedance is shown on the x axis, while imaginary part is shown on the y axis (Figure 3.2 (b) and (d)).

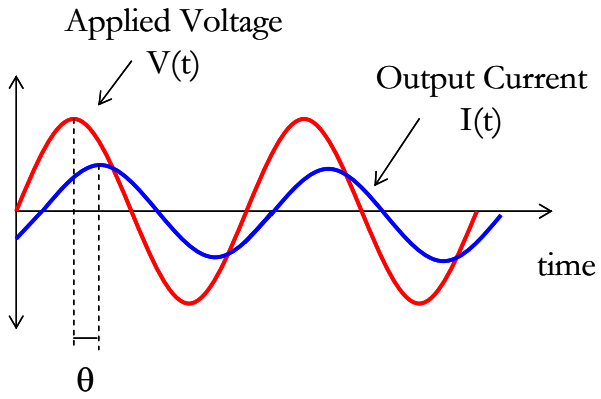

Figure 3.1: Applied voltage-output current vs. time relations showing phase difference (θ)

Figure 3.2. (a) and (b) shows a resistor (R) parallel with a capacitor (C) (simple RC circuit) and typical impedance (Z) response for it, respectively. Any simple material-electrode system demonstrates resistive and capacitive contributions behaving in parallel as seen in Figure 3.2 (a). In Figure 3.2. (b), ω_p is the peak angular frequency. It is possible to obtain dielectric relaxation time or time constant as $\tau_D = RC$. At the top of the arc $\tau_D\omega_p=1$. The relationship between $\tau_D\omega_p$ determines the frequency range impedance plane curve is seen. In Figure 3.2.(d) two distinct bulk arcs are seen in different frequency ranges owing to different RC constants of different material phases.

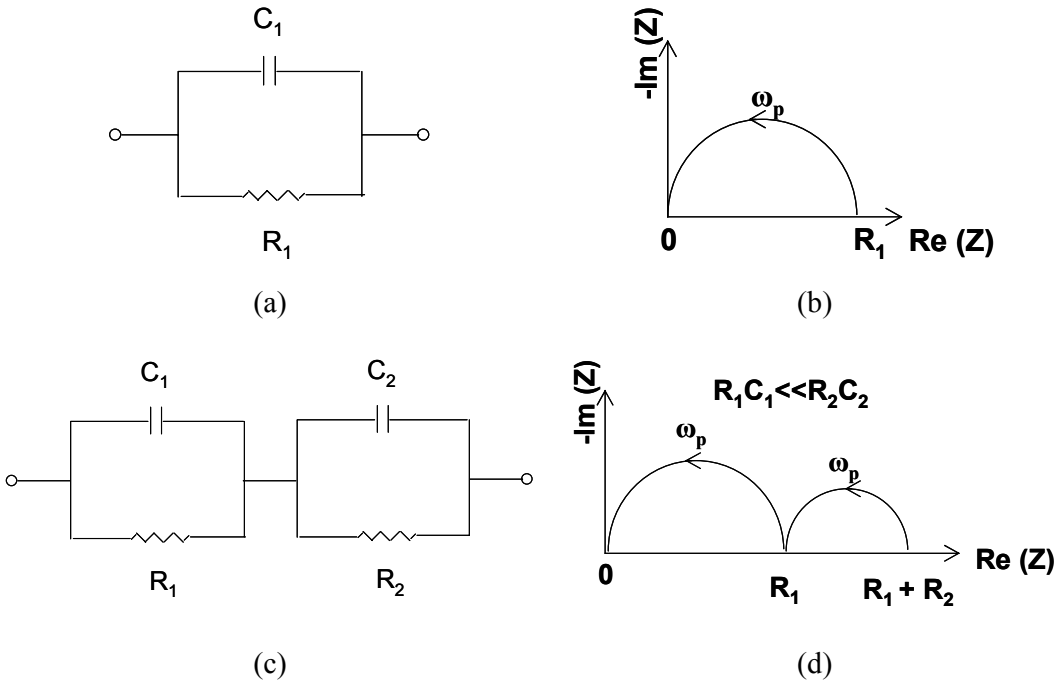

Figure 3.2: a) Simple RC circuit consist of resistor and capacitor in parallel b) Impedance response of simple RC circuit c) Two RC circuits in series with each other d) Impedance response of the two RC circuits

AC-IS measurement is based on application of an alternating voltage at a range of frequencies to a sample, and measurement of the magnitude and phase of current. The collected data are then transformed into real and imaginary components as shown in Figure 3.3. Frequency is stepped from high (MHz) to low (Hz) such that each frequency generates a single datum in so-called Nyquist plots (-imaginary vs. +real impedance), with frequency markers ($\log_{10}$f) as shown.

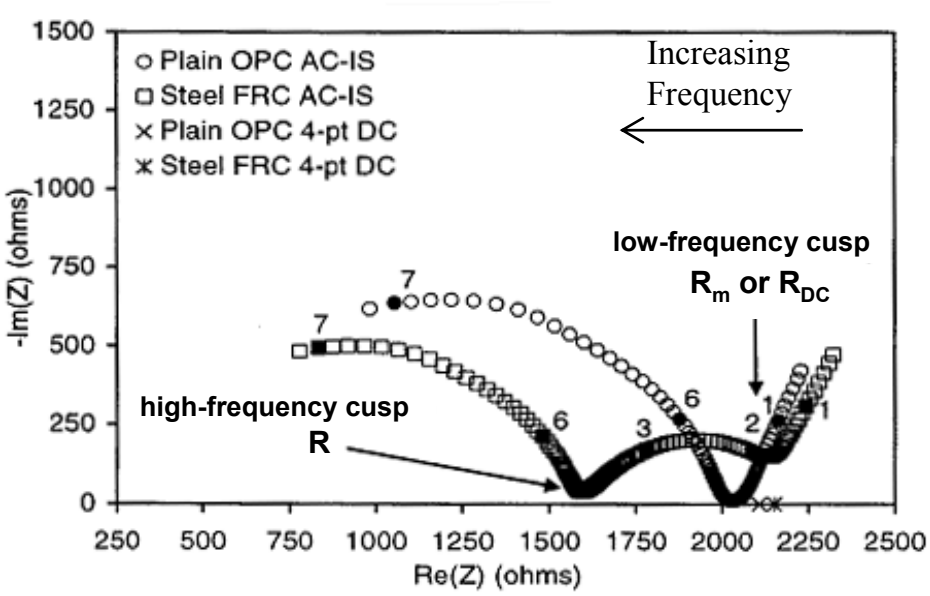

Figure 3.3: Typical Nyquist plot for plain OPC and steel-fiber reinforced composite with frequency markers

Without fibers, OPC (ordinary Portland cement) paste shows a single bulk arc (to the left of the low-frequency (LF) cusp). On the other hand, the steel fiber-reinforced OPC specimen displays two bulk arcs, separated by a high-frequency (HF) cusp which gives the resistance of composite. This is called dual-arc behavior and occurs due to the frequency dependent behavior of conductive fibers. Frequency dependent behavior can be explained with reference to Figure 3.4. Conductive fibers act as insulators under DC or low frequencies of AC (Figure 3.4 (a)) because of a polarization layer (double layer/charge transfer resistance) forming at the fiber-electrolyte interface, while they act as conductors under high frequencies of AC (Figure 3.4 (b)). It should be stressed that dual-arc behavior can only be obtained by AC measurements, and not by DC methods.

In Fig. 3.3, low-frequency cusp in both plots is for the resistance of matrix. Small difference between the two low-frequency cusps may occur due to experimental error and/or material dissimilarities between the specimens. DC measurements are also performed on the specimens to check the low-frequency AC-IS results. AC-IS and DC results are in good agreement as seen in Figure 3.3. The rightmost arc in both curves is associated with the electrode response and does not depend on the material properties.

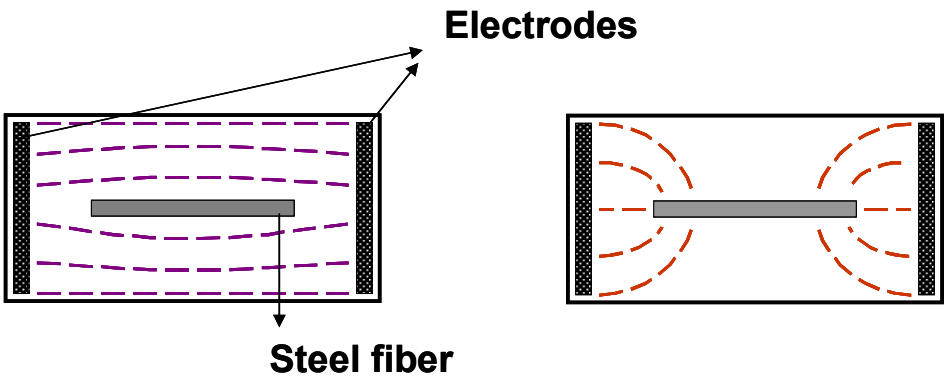

(a) (b)

Figure 3.4 : Schematic diagram of current flow, a) current flow at DC and low AC frequencies, b) current flow at high AC frequencies

By making use of frequency dependent behavior, fiber dispersion can be characterized in terms of the conductivity of composite and cement matrix.

For composites with low fiber volumes, an intrinsic conductivity approach can be employed to evaluate impedance results. This approach is based on each particle shape/geometry having an intrinsic conductivity and the dependence of overall conductivity on the intrinsic conductivity of inclusions. Equation (3.1) shows this relation for FRCs with low fiber volumes [53].

$$\sigma / \sigma_m = R_m / R = 1 + [\sigma]_\Delta \phi \qquad \Delta = \frac{\sigma_p}{\sigma_m} \tag{3.1}$$

In this equation, σ is the conductivity of the composite, σ_m is the conductivity of the matrix, R is the resistance of the composite (the high frequency cusp (R) in Figure 3.3), R_m is the resistance of the matrix (the low frequency cusp resistance in Figure 3.3), ϕ is the volume fraction of fibers, and $[\sigma]_\Delta$ is the "intrinsic conductivity" of the fibers. Δ is the ratio of the fiber (particle) conductivity to the matrix conductivity and approaches "∞" for highly conductive particles, while it goes to "0" for insulating particles. The intrinsic conductivity is determined exclusively by the aspect ratio (AR=length vs. diameter) of the fibers using Eq. (3.2).

$$[\sigma]_{\infty} = \frac{1}{3}\left[\frac{2(AR)^2}{(3\ln\{4(AR)\}-7)} + 4\right] \quad \textbf{(3.2)}$$

3.2.1.1 Equivalent circuit modeling

Equivalent circuit modeling is applied to simplify complicated systems using functionally equivalent forms [54]. In this study, an equivalent circuit model which was developed by Woo and co-workers [55] is employed for the impedance response of fiber-reinforced composites and an equivalent circuit software is used to fit the behavior of electrical circuit elements to the measured data [56]. Detailed information regarding equivalent circuit modeling of frequency-dependent behavior of fiber-reinforced composites can be found in literature [55, 57].

3.2.2 Characterization of fiber dispersion using AC - impedance spectroscopy

Fiber dispersion in fiber reinforced cementitious materials was studied using AC-IS. Dispersion issues in fiber reinforced cementitious materials were classified as orientation, clumping and segregation (Figure 3.5). Experimental methods were modified to characterize different issues.

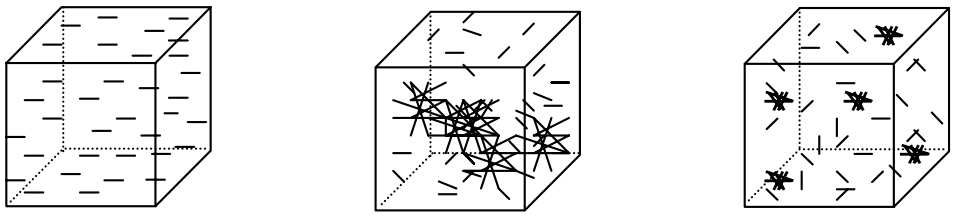

Figure 3.5 : Dispersion issues in FRCs a) preferred orientation, b) large-scale segregation, c) clumping

3.2.2.1 Fiber orientation – Fractional effective conductivities

The orientation of fibers in preferred directions leads to variable mechanical performance due to different material properties in each direction. The degree of orientation is a critical parameter in controlling the mechanical performance. It was demonstrated, by model studies (experimental, theoretical) on single conductive fibers, that the AC-IS response is directionally sensitive and can be used for detection of preferred orientation [25]. In a previous study, it was shown that AC-IS measurements in three directions (3-D) are quite sensitive to the presence of

preferred orientation of fibers [58, 59]. For example, in a perfectly aligned specimen the value of $[\sigma]_{\Delta}$ in Eq. (3.1) measured in the same direction as the fibers, is triple that of $[\sigma]_{\Delta}$ measured in a random FRC specimen. 3-D AC-IS involves making independent "effective" intrinsic conductivity measurements in x, y, and z directions of a given composite specimen:

$$[\sigma]_{\Delta i} = \frac{\frac{R_{matrix}}{R_{composite}} - 1}{\varphi} \qquad i = x, y, z \tag{3.3}$$

The effective intrinsic conductivity in the i^{th} direction is then normalized by the sum of intrinsic conductivities and resulting fractional x, y, z effective conductivities are calculated:

$$f_i = \frac{[\sigma]_{\Delta i}}{\sum_{i}^{3} [\sigma]_{\Delta i}} \tag{3.4}$$

3-D AC-IS measurements are performed on FRC specimens and test results are presented in Chapter 4.

3.2.2.2 Fiber segregation – Local probe method

Whether by improper mixing or gravitational settling (steel fibers are much more dense than cement paste or fresh concrete), macroscopically inhomogeneous dispersion of fibers can occur in FRCs, as shown in Figure 3.5 b. Segregation of fibers in some parts of the element leads to the formation of fiber free areas throughout the material. Previous work demonstrated that the fiber free areas in FRCs can act as flaws; crack initiation and propagation is favored in the fiber-free areas, leading to reduced strength and toughness [60]. Thus, detection of these reinforced vs. unreinforced regions has great importance. A "local probe" technique was utilized to investigate macro-scale segregation of fibers. The technique is borrowed from the field of electroceramics, where it is known as a "point probe" to evaluate the electrical properties of grains vs. grain boundaries [61, 62]. The method can be described with reference to Figure 3.6.

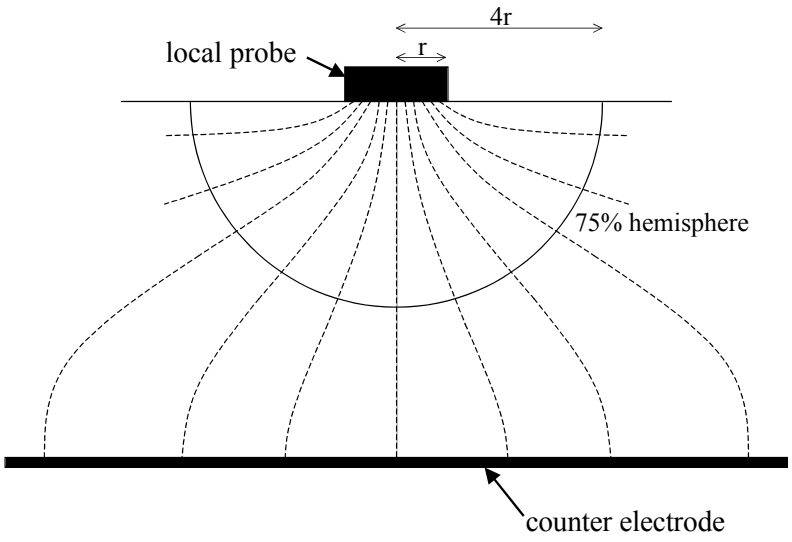

Figure 3.6: Current constriction to a planar point electrode with circular geometry showing the hemisphere over which 75 % of the resistance drop occurs for such a point contact.

For a planar electrode with circular geometry, current-bunching results in a "spreading resistance" that can be much larger than the overall bulk resistance of the body. This contact resistance is given by the Newman equation [63]:

$$R_{contact} = \frac{1}{4\sigma r} \tag{3.5}$$

where r is the radius of the electrode and σ is the conductivity of the body being measured. Fleig and Maier [62] reported that 75% of this resistance derives from a hemisphere with a radius four times that of the contact, as shown in Figure 3.6. This hemisphere, therefore, can be used as a "local AC-IS probe" near the surface of FRCs. The only conditions are 1) the counter electrode must have a large area so as to have negligible resistance vs. the probe, 2) the bulk resistance of the body should be small relative to the probe resistance (of the hemisphere), and 3) the hemisphere diameter needs to be at least several times larger than the fiber length in the composite being studied. Segregation in a FRC specimen is monitored using local probes. Test results are given in Chapter 4.

3.2.2.3 Fiber Clumping

It is possible to achieve a macroscopically uniform fiber density in FRCs, but with micro-scale inhomogeneities, e.g., due to fiber clumping, especially when small

fibers are involved (see Figure 3.5 c). Characterization of fiber clumping is important to control fiber-free areas in FRCs. To evaluate micro-scale inhomogeneities by using AC-IS a "dispersion function/factor" (DF) was used. The idea is based on comparing the normalized conductivity of an actual FRC:

$$(\sigma / \sigma_m)_{observed} = R_m / R = 1 + [\sigma]_{\Delta} \varphi' + \sum [\sigma]_{\Delta i} \varphi_i \qquad \textbf{(3.6)}$$

to that of perfectly dispersed FRC (Eq. 3.1). On the right side of Eq. 3.6, the second term accounts for the effect of the randomly distributed fibers in a given composite and the final term accounts for the effects of fiber clumps of various sizes/ geometries. It should be noted that although the intrinsic conductivities of fiber clumps can be expected to be smaller than for isolated fibers, this term is not negligible. DF is given as the ratio of Eq. 3.6 (from actual composite data) to Eq. 3.1 (the theoretical value assuming perfect dispersion):

$$DF = \left[\frac{\left(\frac{\sigma}{\sigma_m} \right)_{observed} - 1}{\left(\frac{\sigma}{\sigma_m} \right)_{theory} - 1} \right] = \frac{\phi'}{\phi} + \frac{\sum [\sigma]_{\Delta i} \phi_i}{[\sigma]_{\Delta} \phi} \qquad \textbf{(3.7)}$$

It should be stated that DF is not equal to the fraction of well-dispersed fibers. Since the rightmost term in the Eq. 3.7 is non-zero, DF is only an upper limit for the fraction of dispersed fibers. A series of tests were done on fresh and hardened FRC specimens and dispersion functions were calculated. Tests on FRC specimens will be discussed in Chapter 4, under the title of "fiber clumping".

3.2.3 Image analysis

Image analysis is a well studied and fundamental method to quantitatively evaluate fiber dispersion. Various image analysis methods exist. These methods can be distinguished by the technique by which images are captured and analyzed [64]. Two or three dimensional data can be used to obtain fiber dispersion characteristics. In this study, data from two dimensional cross-sections were used for fiber clumping and orientation analyses. Statistical point processes were employed to evaluate fiber clumping and second order orientation tensors were used to calculate fiber orientation.

3.2.3.1 Fiber clumping

Diggle defined a spatial point process as any stochastic mechanism that generates a countable set of events x_i in the plane [65] and described first order and second order properties of a spatial point process. Akkaya et al. [60], proposed that point process statistics could be used to calculate fiber dispersion in a specimen cross-section. They suggested that if fibers are not packed together in close contact, then the center of the fiber cross-sections can be assumed as points for realization of the point process. They used first order and second order functions of spatial point processes to describe fiber intensity, the tendency of fibers to clump and repel each other, and the fiber-free area in the cross-section. In this study, point process statistics are used to define the clumping level of fibers. The centers of the fiber cross-sections were assumed to be points. Three different fiber volume ratios were studied (1%, 2%, and 4%). Figure 3.7 shows cross-sections from specimens with fiber volume ratios of 1, 2, and 4 % respectively. As can be seen from Figure 3.7, most of the fiber cross-sections are circular or elliptical, however, there are fibers aligned almost parallel to the cutting plane (Figure 3.7). For these fibers, the mid points of the lines were assumed to be points. To check the validity of this assumption, the percentage of the fiber cross-sections with a major/minor axis ratio greater than 5 was calculated. Less than 1% of the fibers was found to have a ratio that exceeded 5. Please note that, if the fiber is aligned perfectly parallel to the cutting plane, then the major/minor axis ratio would be 37.5 (fiber length = 6 mm, diameter = 0.16 mm).

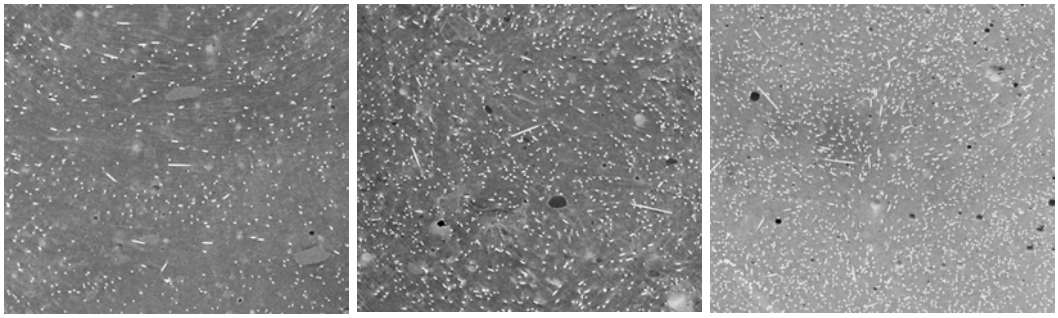

(a) (b) (c)

Figure 3.7: Cross-sections of specimens with fiber volume ratios of a) 1%, b) 2%, and c) 4%

To be able to use point process statistics, the sample under consideration should satisfy certain basic conditions. The sample should be stationary and isotropic. A

process is stationary if all probability statements about the process in any region A of the plane are invariant under arbitrary translation of A, and isotropic if the same invariance holds under rotation, i.e., if there are no directional effects [65]. To check if it is stationary, statistical analyses were done on the sub-regions of the pattern under consideration, and replicable results were found. To check for isotropy, the equation below is employed [66].

$$\hat{K}_E(r) = \frac{(\text{Area of } A_R) \times \sum_{\text{fibers} \in A_R} (\text{number of fibers in A, within the cone sector c(r, } \theta, \Phi))}{(\text{number of fibers in } A_R)^2} \times \frac{360}{2\theta} \quad \textbf{(3.8)}$$

Figure 3.8 (a) shows a schematic of $\hat{K}_E(r)$ estimator. A Fortran routine (Appendix A) was written for the determination of the estimator $\hat{K}_E(r)$. The number of fibers in the cone-sector is calculated for each fiber for different sector orientations. Estimates for different sector orientations did not show any dependence upon ϕ, suggesting that the system was isotropic.

In this study, the K function was used to quantitatively describe fiber clumping. The K function gives the tendency of fibers to clump and repel each other. The estimator of the K function is given as [66]:

$$K = \frac{\text{Expected number of fibers within a distance r of x, given that x is a fiber location}}{\text{fiber intensity of the process}} \quad \textbf{(3.9)}$$

For determining the K function, the number of fibers in an area with a radius r of every fiber is needed. While this data can be obtained precisely for central fibers, it maybe incomplete for the fibers that are closer than r to the edge of the area, as seen in Figure 3.8 (b). To avoid this, analyses were done for fibers in a smaller area (A_R), where all fibers in it are at least a distance r from the edge of the window, making it possible to take into consideration all neighboring points for every fiber (Figure 3.8 (c)) (See Appendix A for Fortran routine).

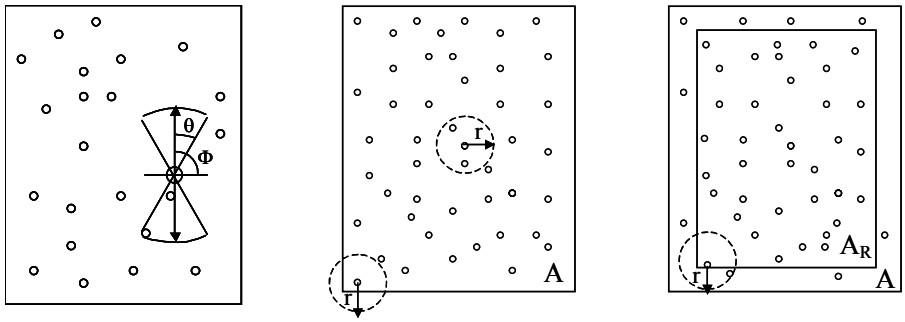

(a) (b) (c)

Figure 3.8: Schematic of a) K_E and b) K function entire section c) K function sub - section [60]

Akkaya [18] proposed a Clumping Factor (CF) to describe the degree of clumping by means of the K function (Eq. 3.10). The idea is based on comparing the observed value of the K function, to the theoretical value. The theoretical value of the K function can be calculated using a reference point process. For this study, a Poisson process was employed as a random reference point process. Figure 3.9 shows the K functions for the specimen with 1% fiber volume and for a spatially random dispersion. For a spatially random dispersion the K function is equal to πr^2. The upper curve, corresponding to the experimental K function, shows clumping. In Eq. 3.10, πr^2 is for the K function of a random distribution and C is the constant term of the experimental data. K functions were calculated for each specimen and given in Chapter 4.

$$\%\ \text{Clumping Factor} = \left(\frac{K_{observation}}{K_{theory}} - 1 \right) x\,100 = \left(\frac{Cr^2}{\pi r^2} - 1 \right) x100 \qquad \textbf{(3.10)}$$

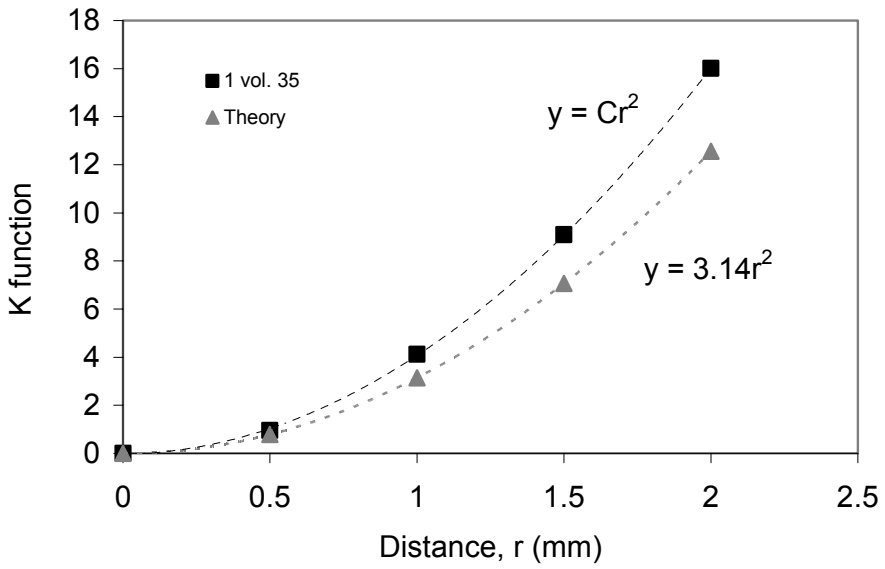

Figure 3.9: Observed and theoretical (random) K-functions of the fiber dispersions for the specimen with 1 % of fibers and water-to-cement ratio of 0.35

3.2.3.2 Fiber orientation

A tensor description method was employed for fiber orientation density calculations in the specimen. A detailed description of the method is given in literature [33, 64, 67, 68]. It is possible to describe a 3-D fiber orientation state using a 2-D micrograph of a sample. For a single fiber, the orientation state can be described using in-plane (ϕ) and out-of- plane (θ) angles, as shown in Figure 3.10. On the other hand, to describe the fiber orientation state for a number of fibers that are distributed in a volume, a more general description is needed. The most commonly used description is the probability distribution function, ψ, which gives the probability of encountering a fiber between the angles θ_1 and $(\theta_1+d\theta)$ and ϕ_1 and $(\phi_1+d\phi)$, and is defined as,

$$P(\theta_1 \le \theta \le \theta_1 + d\theta, \phi_1 \le \phi \le \phi_1 + d\phi) = \psi(\theta_1, \phi_1)\, \mathrm{Sin}\theta_1 d\theta d\phi \qquad \textbf{(3.11)}$$

It is also possible to involve fiber length as a variable in Eq. 3.11 [64]; however this was not necessary in this study, since rigid fibers with uniform circular cross-section and uniform length were used. Thus, fiber length was not considered as a variable. As an alternative and simpler way, it is common to use a unit vector p, as shown in Figure 3.10, to define orientation of a single fiber.

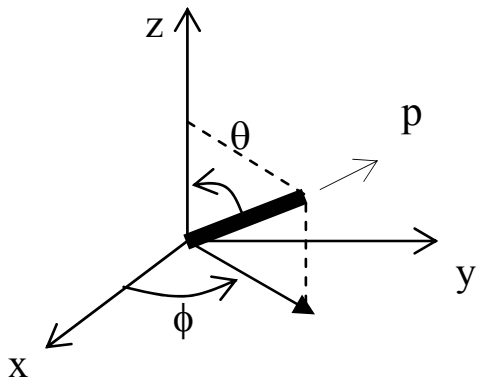

Figure 3.10: In-plane (ϕ) and out-of-plane (θ) angles of a single fiber

The components of p in 3 directions give the orientation state of a single fiber in reference directions,

$$p_x = Sin\theta\, Cos\phi$$
$$p_y = Sin\theta\, Sin\phi \qquad \textbf{(3.12)}$$
$$p_z = Cos\theta$$

For complete 3-D orientation information, at least 2 orthogonal cross-sections of a specimen should be analyzed. This is due to the fact that it is not possible to distinguish two fibers at angles (θ, ϕ) from the fibers at angles (θ - π, ϕ + π) as seen in Figure 3.11. A second cross-section is needed for the missing part of the data or the following symmetry assumption must be made [68]. In this study, a second cross-section was not used because, only the orientation densities in the reference directions (x, y, z) were needed and these values were not affected by the symmetry assumption.

$$\psi\,(p) = \psi\,(-\,p) \qquad \textbf{(3.13)}$$

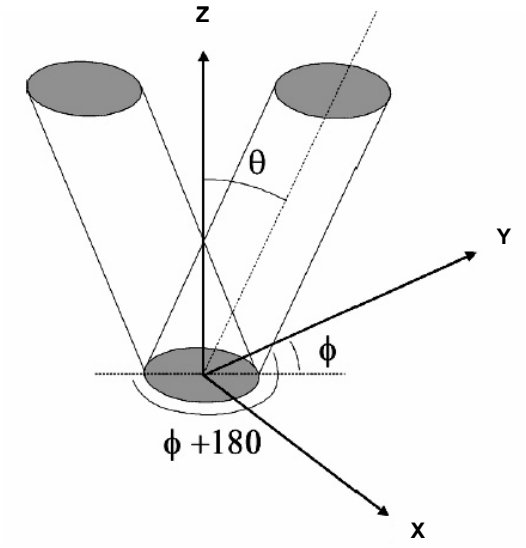

Figure 3.11: Two fibers at angles (θ, ϕ) and (θ - π, ϕ + π) cannot be distinguished [68]

In addition, since ψ (p) is a density function, the following normalization condition is valid.

$$\int_{\theta=0}^{\pi}\int_{\phi}^{2\pi}\psi(\theta,\phi)\,Sin\theta\,d\theta\,d\phi = \oint\psi\,dp = 1 \qquad \textbf{(3.14)}$$

The orientation distribution function, ψ (p), is known as a complete and general method to obtain the fiber orientation state; however, it is mentioned by various researchers [33, 67, 68] that the practical use of the function is cumbersome and needs intensive calculations. Therefore, Advani and Tucker [67] proposed the use of orientation tensors instead of orientation distribution functions to describe the orientation state. The calculations of orientation tensors are straightforward, and they give concise information about the fiber orientation density. Orientation tensors are obtained from moments of the orientation distribution function. Non-even moments are zero due to the symmetry of the function and generally second order tensors are used to define orientation density.

$$a_{ij} = \frac{\sum (p_i p_j)_n F_n}{\sum F_n} \qquad \text{i, j = x, y, z} \tag{3.15}$$

In Eq. (3.15), a_{ij} stands for the components of the orientation tensor, p_i and p_j represent components of the unit vector p, F stands for the weighting function, and the subscript n shows the number of fibers. The weighting function (F) is used to account for the effect of fiber orientation on the probability of being intercepted by the cross-section under consideration. It is clear that the probability of intercepting a fiber which is aligned vertical to the cutting plane is much higher compared to a fiber aligned parallel to the section. To obtain an unbiased estimate of fiber orientation, every component should be weighted as described in Eq. (3.16) [64]. In Eq. (3.16), L stands for fiber length and θ represents the out-of-plane angle. θ_c is the cutoff angle that can be described as the angle above which a fiber has a useful projected height of fiber diameter d.

$$F_n = \frac{1}{L\ Cos\theta_n} \qquad \text{for} \quad \theta < \theta_c$$

$$F_n = \frac{l}{d} \qquad \text{for} \quad \theta > \theta_c \quad \text{and} \quad \theta_c = \cos^{-1}\left(\frac{d}{L}\right) \tag{3.16}$$

4. FIBER DISPERSION -EXPERIMENTAL STUDY: PART I

4.1 Introduction

In chapter 3, the basics of AC-IS and the experimental methods used were given together with analyzing techniques. Image analysis methods used were also explained. In this chapter, application of AC-IS to detect various dispersion issues is studied on conductive fiber-reinforced cement-paste specimens. The ability of AC-IS to monitor fiber orientation, fiber segregation and fiber clumping is discussed. The use of image analysis for monitoring different fiber dispersion issues is also studied. Results of the two methods are evaluated together to better understand the extent to which AC-IS predicts different fiber dispersion issues. Finally, a comparison of the two methods is given.

4.2 Materials and Specimen Preparation

Fiber-reinforced cement paste specimens were cast using LaFarge Type I Portland Cement and short-cut steel fibers. Three fiber volumes (1 %, 2 %, and 4 %) and two water-to-cement ratios (0.30 and 0.35) were used. Fibers were 6 mm long and 0.16 mm diameter short cut steel fibers and were provided by Bekaert.

The mixing sequence was as follows: First, the cement and steel fibers were dry mixed for 1 minute at low speed using a Hobart planetary mixer, then water was added, and the mixture was mixed for 1 minute at the lowest speed, followed by blending for 2 minutes at the highest speed. Then, the mixture was placed into cubic molds, which were 89 mm on a side, and left for curing under 100 % relative humidity.

4.3 Fiber Dispersion

4.3.1 AC-IS

4.3.1.1 Experimental set up

Figure 4.1 shows experimental set-up for hardened state measurements. Hardened state measurements were performed 7 days after casting. Both 2-point AC-IS and 4-point DC measurements were obtained. Four-point DC results were used to confirm the LF cusp (R_{matrix}) results from 2-point AC-IS measurements. To obtain measurements, each specimen was positioned in a reservoir, and an artificial reservoir was created at the top of the specimen using tape and sealing cord as seen in Figure 4.1. Stainless steel electrodes were placed in the reservoirs. The reservoirs were filled with 1 M NaCl solution to provide good contact between the electrodes and the specimen. For 2-point AC-IS measurements, steel electrodes were used to apply voltage excitation and obtain current response. A Solartron 1260 impedance/gain-phase analyzer was used, and the frequency was stepped from 11 MHz to 100 mHz under a voltage excitation of 1V. For 4-point DC measurements, steel electrodes were used to apply the current, and steel wires were wrapped around the specimen to be used as voltage leads. A programmable current source was used, and the current was applied to the electrodes in 1 mA increments from 10 mA to -10 mA.

Figure 4.2 shows experimental set-up for fresh state measurements. For the tests in the fresh state, stainless steel electrodes were placed into moulds before casting and 2-point AC-IS measurements were started 25 minutes after adding water to the mixture. Four-point DC measurements were not made in the fresh state due to experimental limitations.

Another experimental set up -Local-probe configuration- was used for segregation tests. This configuration will be explained in section 4.3.1.3.

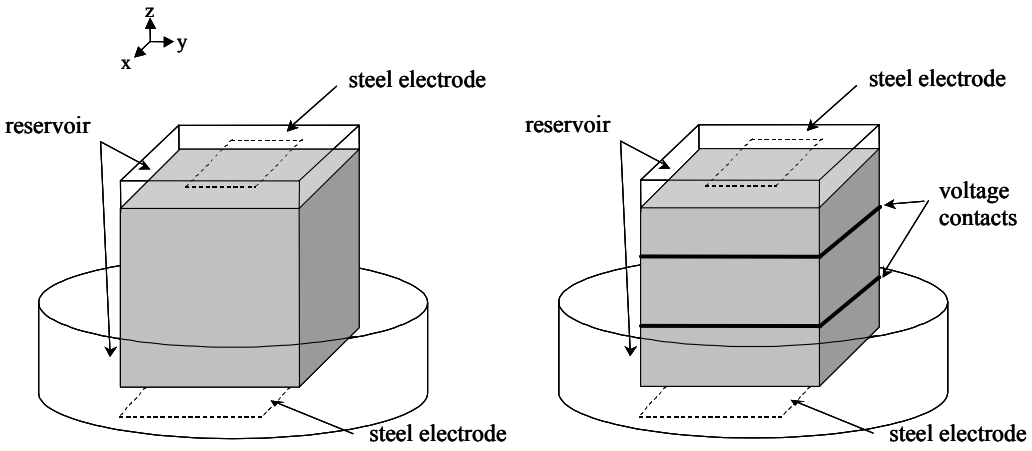

Figure 4.1: Experimental set-up for hardened state AC-IS measurements a) 2-point AC-IS and b) 4-point DC

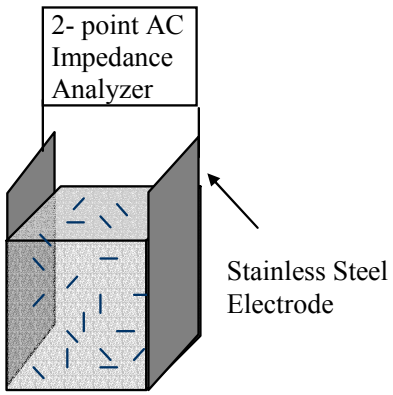

Figure 4.2: Experimental set up for fresh state AC-IS measurements

4.3.1.2 Fiber orientation

3-D AC-IS and DC measurements were obtained 7 days after casting and fractional effective intrinsic conductivities were calculated for each specimen as described in section 3.2.2.1. Figure 4.3 shows fractional intrinsic conductivities on a ternary diagram. A ternary diagram is used to represent contributions to the orientation from 3 directions. In case of theoretically random orientation, orientation density is equal in each direction and the center of the triangle (Δ) shows the orientation state. In case of theoretically planar (xy) and uniaxial (x) orientations, this point switches to bottom (□) and corner (O) of the diagram respectively as is shown with arrows.

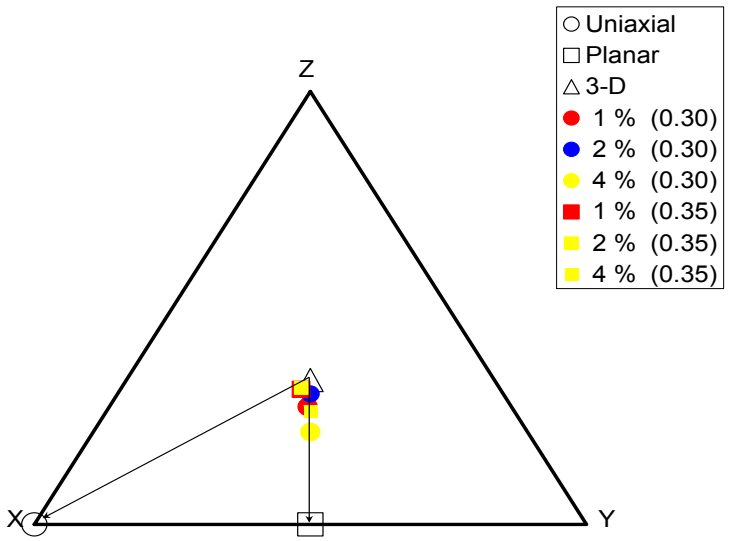

Figure 4.3: Triangular represantation of relative x, y, and z contributions to the intrinsic conductivity and therefore the alignment of fibers

The solid data points are from the FRC cubes with fiber contents of 1, 2, 4 vol. % (6 mm long, 0.16 mm diameter) and water to cement ratios of 0.30 and 0.35. As seen in the figure, fibers tend to align vertical to the casting direction (z) and parallel to the xy plane. Highest preferred orientations were detected in the specimens with 4 % fiber volume content.

4.3.1.3 Fiber segregation

Fiber segregation experiments were performed by Leta Y. Woo. Local AC-IS probe was used to study fiber segregation in an FRC specimen. An FRC cube (89 mm on a side) was prepared with 1 vol. % of steel fibers (6 mm long, 0.16 mm diameter), but with all the fibers cast in the bottom third of the cube as seen in Figure 4.4. Once hardened, the cube was turned on its side (see the inset of Figure 4.5) and measurements were obtained. The probe on the top surface consisted of a moist electrode of 6 mm diameter (a flat sponge disk saturated with 1M NaCl solution and contacted from above with a steel plate electrode) whereas the counter electrode was a large steel plate pressed against a similarly saturated sponge contacting the entire bottom surface. The local probe was stepped across the top surface, and AC-IS measurements were taken. From the LF- and HF-cusp resistances, the local normalized conductivities (as per Eq. 3.1) were obtained as shown in Figure 4.5. As can be seen from the Figure 4.5, matrix-normalized conductivity increased at the

fiber-rich end of the specimen. A slight increase is also seen in the middle section due to the fact that the local probe monitors a hemisphere volume with a radius of four times that of the contact.

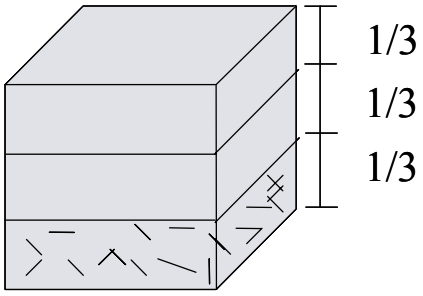

Figure 4.4: Schematic of the specimen used for segregation study

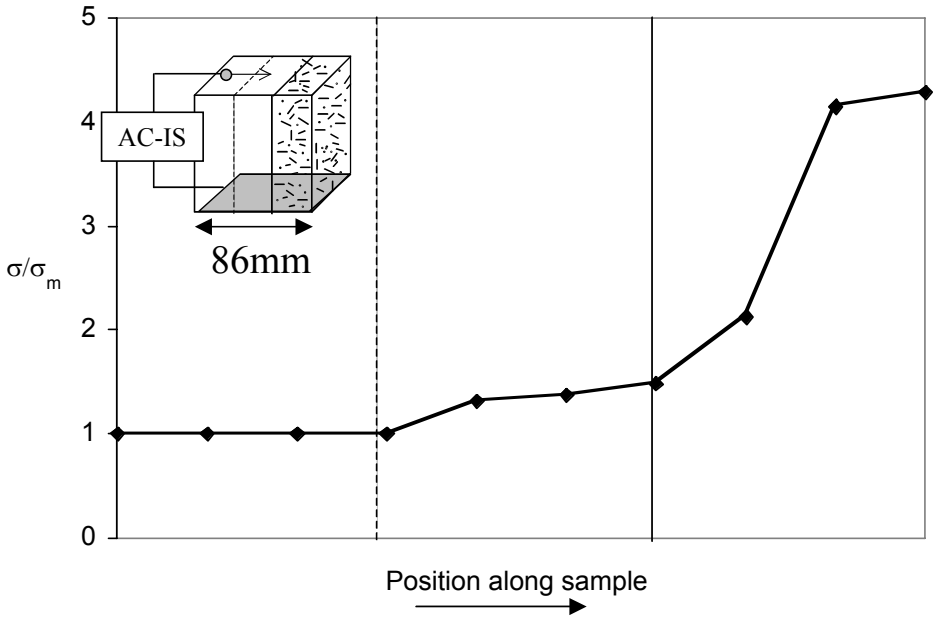

Figure 4.5: Matrix–normalized conductivity profile made by local AC-IS probe for a specimen with fibers intentionally segregated to one end (e.g., to simulate settling).

This result means that AC-IS can be employed to characterize fiber segregation in FRC specimens.

4.3.1.4 Fiber clumping

Results from 3-D orientation measurements were used to calculate DF values to evaluate fiber clumping in the FRC specimens. Additional experiments were conducted in the fresh state to evaluate the amenability of the method to be used as a

characterization method in the fresh state. DFs from the fresh and hardened states were compared.

4.3.1.4.1 Hardened state calculations

Results of 3-D AC-IS and DC measurements were used to calculate dispersion factors (DFs) of each specimen. Matrix-normalized conductivity (σ/σ_m) values from each direction (x, y, z) had been measured for each specimen to study the effect of orientation in section 4.3.1.2. These values were averaged to obtain average σ/σ_m for each specimen. Then, average (σ/σ_m)s were used to calculate DFs as was explained in section 3.2.2.3.

4.3.1.4.2 Fresh state measurements

The degree of dispersion significantly affects the resulting mechanical performance of FRCs as mentioned before. Thus, characterization of fiber dispersion in the fresh state is of considerable interest for control of ultimate mechanical properties.

Sample Nyquist plots are given in Figure 4.6. Prior to set, plain paste shows no bulk arc in Nyquist diagrams; only the electrode arc is visible, as in Figure 4.6. However with the addition of conductive fibers the low frequency arc of the two bulk arcs has become visible and this arc gives the necessary information (the LF cusp resistance and the HF cusp resistance) for detection of orientation, segregation and clumping in fresh composite.

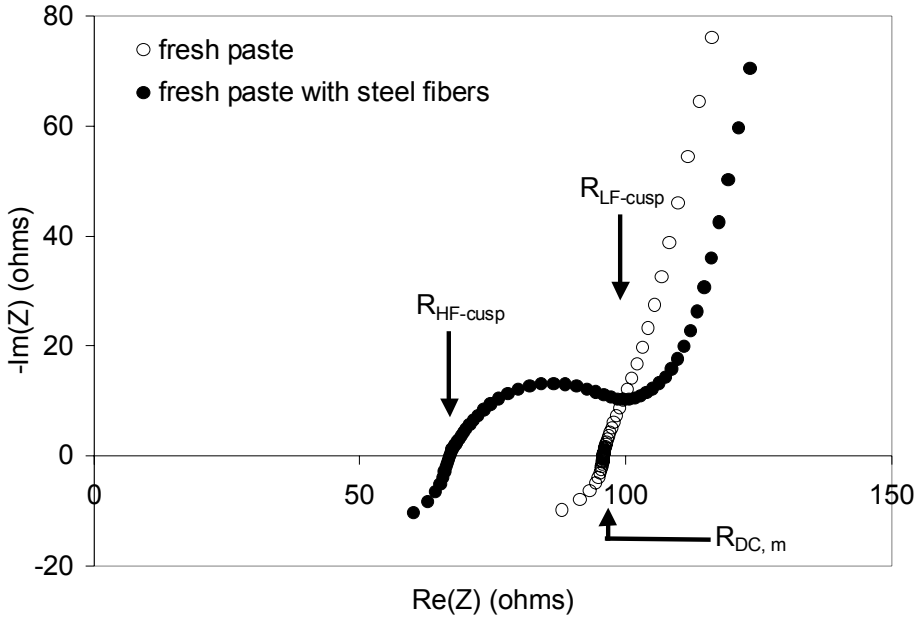

Figure 4.6: Sample Nyquist plots for fresh cement paste with and without steel fibers (1.5 h after mixing)

Fiber reinforced specimens were prepared with fiber volumes of 1 % and 2 % (volume) and w/c of 0.30 and 0.35. Materials and mixing procedure were the same as with hardened FRCs, but this time stainless steel area electrodes were fixed into the moulds before casting, to ensure good contact of electrodes and mixture (Figure 4.2). AC-IS tests were started approximately 25 minutes after adding water to the mixture and ended after 15 hours. 40 AC-IS measurements were taken at 15 minutes time intervals over a 15 hours period. Measurements were taken only in 1 direction due to the experimental limitations. Figure 4.7 shows results from the specimen with 0.35 water-to-cement ratio and 1 vol. % of fibers. In figure, only results of the first (25^{th} minute) and last measurements (15^{th} hour) are given with simulations, which were done using equivalent circuit modeling (Section 3.2.1.1). As seen in Figure 4.7, low-frequency and high-frequency cusps become more visible when specimen is hardened. However, both curves give similar information confirming the ability of AC-IS to be used in the fresh state when σ/σ_m values are compared.

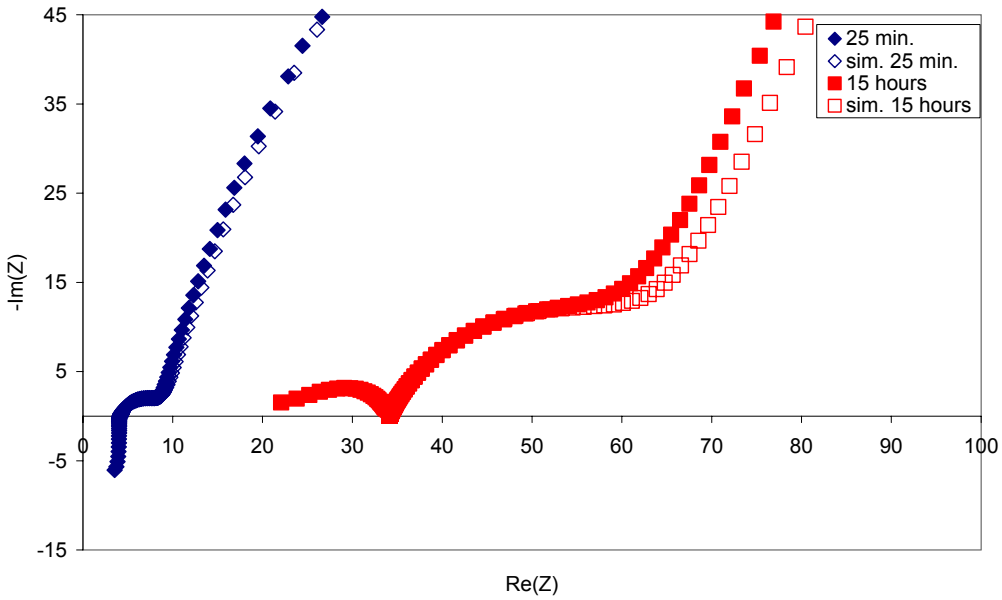

Figure 4.7: Fresh and hardened state measurements from the specimen with water-to-cement ratio of 0.35 and 1 vol. % of fibers.

Figure 4.8 shows the dispersion functions for different fiber volumes and water-to-cement ratios. Open data points show the dispersion factors from fresh state measurements and solid data points show the dispersion factors from hardened state measurements. Results from the fresh and hardened state measurements matched well as seen in Figure 4.8, confirming the ability of AC-IS to characterize fiber clumping in the fresh state. The dashed line illustrates the DF in the absence of clumping (DF=1). The observed dispersion functions were in the range of 0.81 to 0.88 and were not significantly affected by the w/c ratio. To check these results, image analyses were also conducted on the specimens. Clumping was also evaluated using image analysis and comparative analyses were done. The results of the image analyses tests are given in 4.4.1.

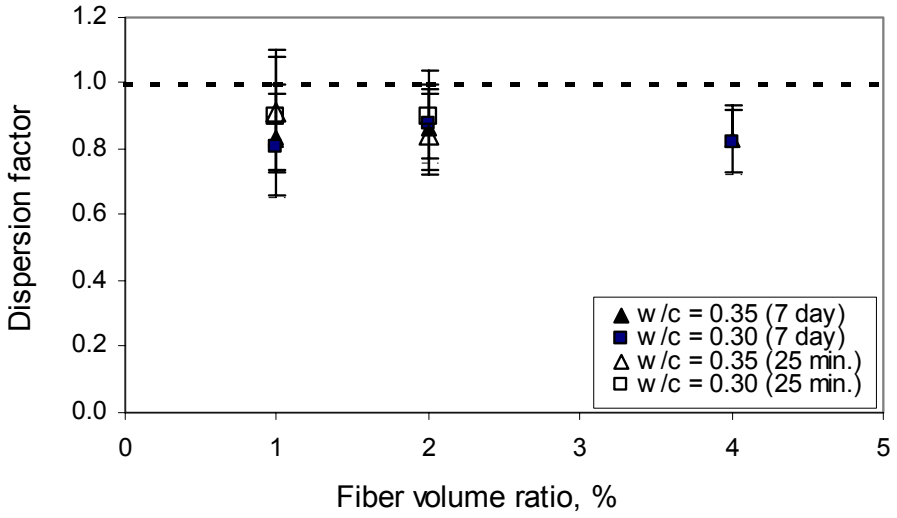

Figure 4.8: Dispersion function – fiber volume ratio relations for water to cement ratios of 0.30 and 0.35.

4.3.1.5 AC-IS Review

A review of AC-IS approach to the fiber dispersion characterization is given in Figure 4.9 [59]. First, a point probe is used to find any global segregation of fibers. If there is global segregation, matrix-normalized conductivity profile of the specimen can be used to evaluate fiber segregation. If global segregation is not present, than 3-D AC-IS measurements are obtained to check for the preferred orientation. If there is no orientation or slight orientation, matrix-normalized conductivity values are averaged to calculate DF values. DF values are used to describe fiber clumping as mentioned before. A DF value close to 1 means no clumping or negligible clumping of fibers. A DF value less than 1 means clumping of the fibers. Smaller DF values are obtained with increasing clumping of the fibers. It should be noted that DF values can not be calculated if severe orientation is detected.

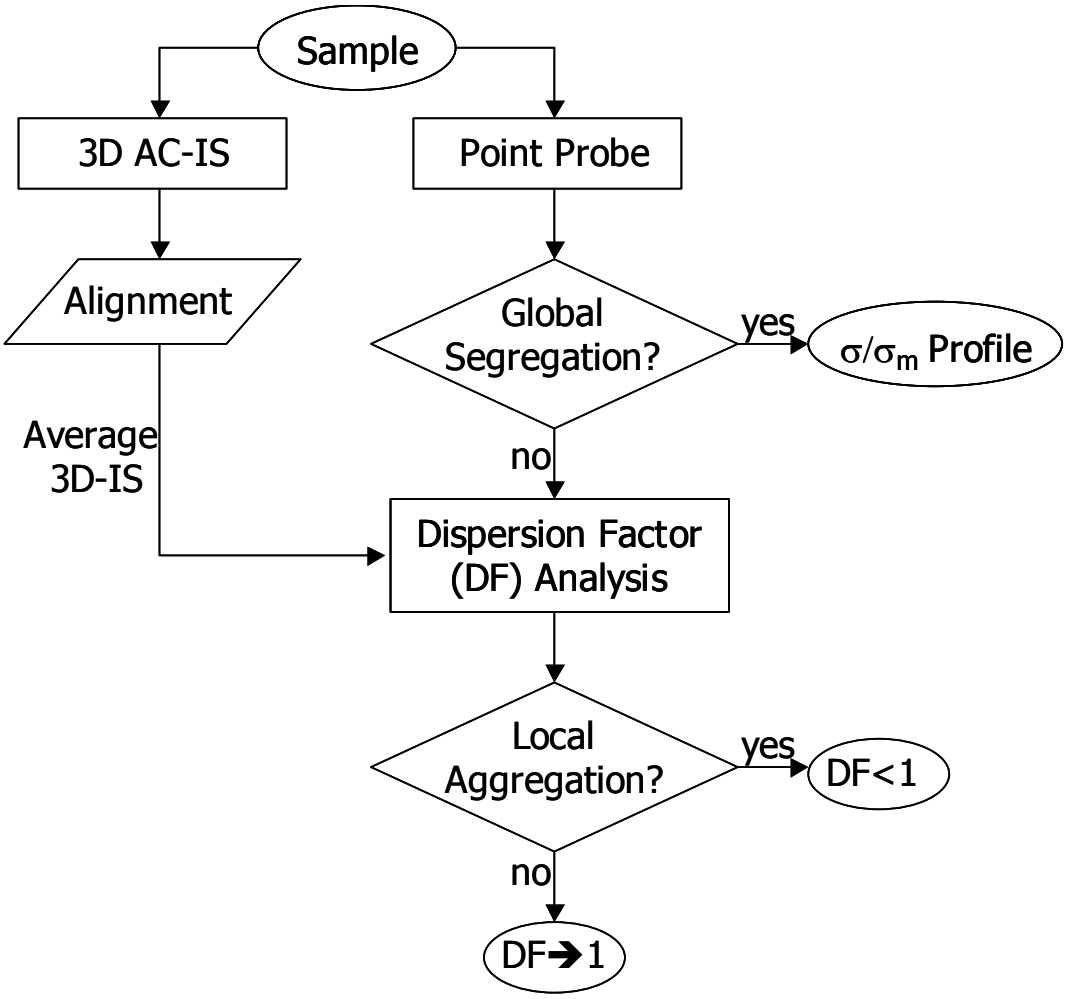

Figure 4.9: A review of AC-IS approach for fiber dispersion characterization

4.3.2 Image analysis

4.3.2.1 Specimen preparation

An image analysis study was carried out on the same specimens that were used for the AC-IS measurements. Specimens were cut either parallel (for clumping analysis) or vertical (for orientation analysis) to the casting direction using a saw cut. Then specimen surfaces were prepared to obtain a good contrast between the fibers and the matrix before taking the pictures. Various preparation techniques were given in the literature and the best preparation technique depends on the image capturing tools employed. In this study, a surface grinder (Okamoto 450) was used to coarsely grind the specimen and then standard grit papers progressing from grit 400 to grit 1200, were used for fine polishing. This method was found to achieve a good contrast between the fibers and the matrix.

4.3.2.2 Image capturing and processing

For image capturing, an optical microscope (Wild M3Z stereo microscope w/UV light source) and a high resolution digital camera with a macro lens were used. The optical microscope was used to take the micrographs, which were later used to calculate orientation density and the high resolution digital camera was used to take pictures, which were later used for the fiber clumping analysis. The reason for using the high resolution camera instead of optical microscope was to be able to obtain the pictures of entire cross-sections with a minimum labor time and cost.

For the clumping analysis, captured cross-section pictures were digitized so that each fiber was considered as a point, using Adobe Photoshop binary (black and white) pictures were obtained and Image J, which is an image processing and analysis program was used to acquire the total number of fibers and the XY coordinates of each fiber.

For orientation density calculations, careful processing of the images was necessary. Adobe Photoshop was used to select and distinguish fibers from the matrix and to obtain binary micrographs. It should be noted that the fibers that were not complete ellipses were not included in the calculations due to time concerns. However, the error associated with neglecting incomplete sections is negligible due to the large number of fibers studied. The formulation for the calculation of incomplete sections can be found in literature, if needed [69]. After binary micrographs were obtained, Image J was utilized for fitting ellipses to the fiber cross-sections and the major and minor axis lengths were obtained together with in plane angle for each fiber. For calculation of out of plane angles, the following equation was used, where a and b are the lengths of the minor axis and the major axis respectively (Figure 4.10).

$$\theta = arc\ cos(\frac{b}{a}) \quad \textbf{(4.1)}$$

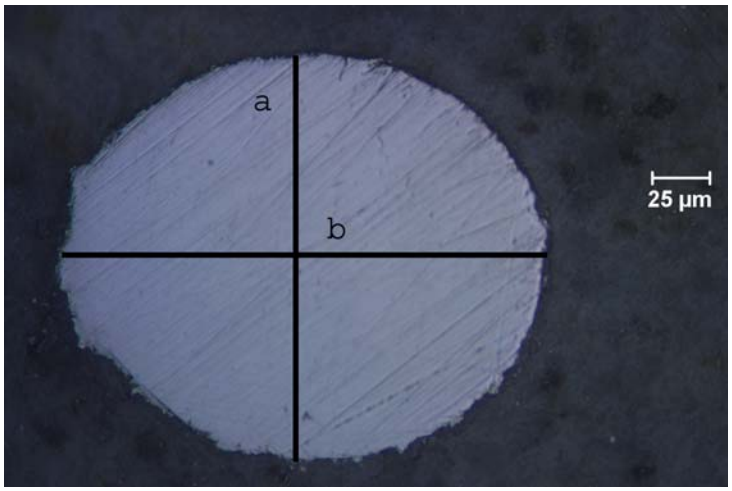

Figure 4.10: Major and minor axes length of a fiber section.

Then x,y,z components of the p vector were calculated for every fiber and weighted using the Eq. (3.16) to calculate the components of the second order orientation tensor.

4.4 Results and Discussion – Comparing AC-IS and Image Analysis

4.4.1 Fiber clumping

To calculate fiber clumping with image analysis, cubic specimens were cut parallel to the casting direction and analyses were done on 1 section for each specimen. Figure 4.11 shows a sample section from the specimen with 4 % vol. of fibers and water - to - cement ratio of 0.30. The studied number of fibers and the cross-section area of each specimen are given in Table 4.1.

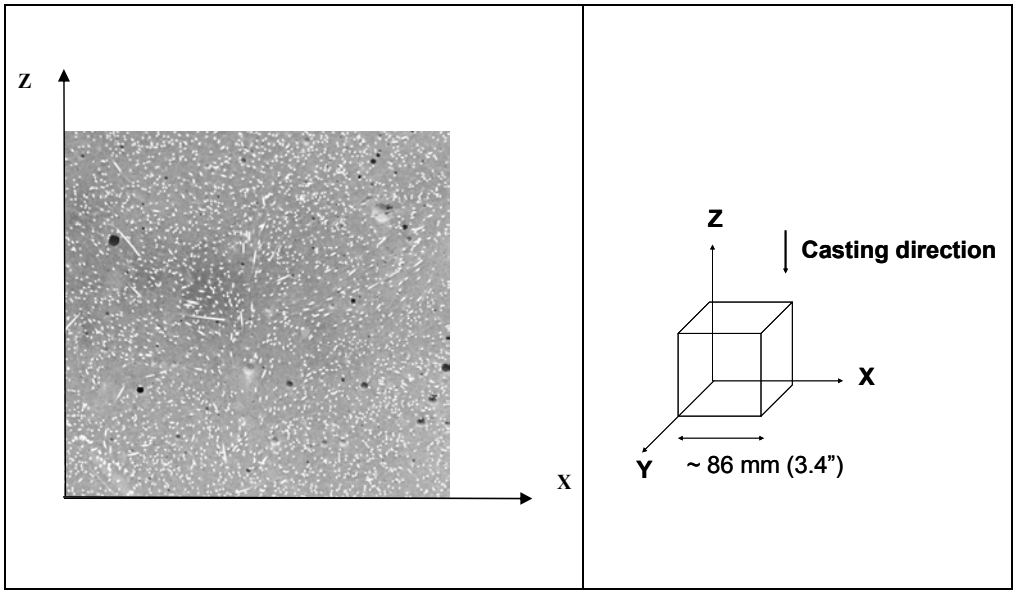

Figure 4.11: A sample section that was cut parallel to the casting direction with a schematic of cubic sample

Table 4.1: The studied number of fibers and cross-section area for fiber reinforced cement specimens

	Fiber volume, (%)	**Number of fibers on the section**	**Cross-section area, (mm^2)**
w/c = 0.30	**1**	1932	7047.6
	2	3577	6955.3
	4	7527	7788.0
w/c = 0.35	**1**	1697	6705.7
	2	3589	7138.0
	4	7944	7743.0

K functions were calculated for radiuses ranging from 0 to 2 mm, and plotted, as was shown in Figure 3.9. A Fortran routine (see Appendix A) was written to obtain the number of neighboring fibers for each fiber. Using K functions, clumping factors were calculated for each specimen, as was explained in 3.2.3.1.

AC-IS (DF) and image analysis (1-CF) results are given in Table 4.2 for different water - to - cement and fiber volume ratios. Clumping factors (CF) are subtracted from 1 so that they can be compared with the dispersion factors.

Table 4.2: Dispersion factors (AC-IS) and 1-CFs (Image analyses) for fiber reinforced cement pastes

	Fiber volume, %	DF (AC-IS)	1-CF (Image A.)
w/c = 0.30	**1**	0.81 ± 0.17	0.79 ± 0.12
	2	0.88 ± 0.13	0.78 ± 0.14
	4	0.82 ± 0.11	0.80 ± 0.16
w/c = 0.35	**1**	0.83 ± 0.17	0.72 ± 0.19
	2	0.86 ± 0.13	0.70 ± 0.24
	4	0.83 ± 0.11	0.85 ± 0.10

AC-IS and image analysis results are plotted together to be able to compare the two methods. Dispersion factors are given on the primary y-axis, while clumping factors are plotted on the secondary axis. Results from the two methods agreed very well in experimental uncertainty. This demonstrates the sensitivity of AC-IS to the clumping of fibers. As can be seen in Figure 4.12, a clear difference was not found in dispersion factors with the increasing fiber volume or water - to - cement ratio. Dispersion factors (AC-IS) were found to be around 0.8 for all mixtures and similar results were obtained from image analyses. Variation in the experimental results was found to decrease for 4 % fiber volume.

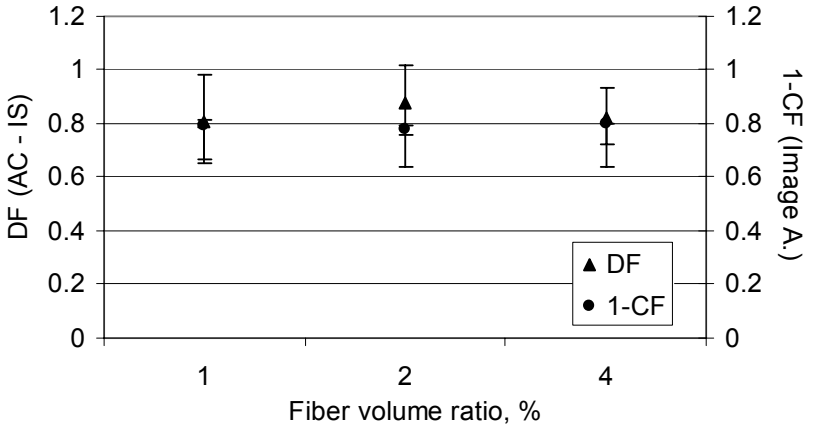

(a)

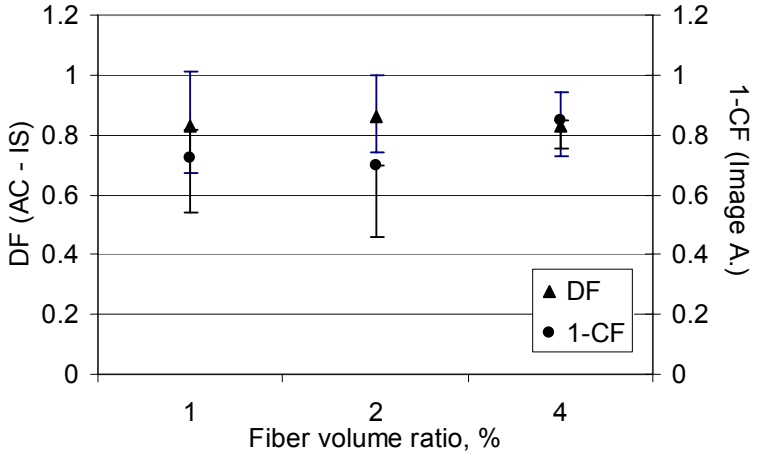

(b)

Figure 4.12: Comparison of DF (AC-IS) and 1-CF (Image analysis) a) w/c = 0.30, b) w/c = 0.35

4.4.2 Fiber orientation

AC-IS measurements were obtained in 3 directions, fractional effective intrinsic conductivities were calculated for each direction, as defined in section 3.2.2.1 and the results were given in Table 4.3. Fractional conductivity values were found to be lower in the z direction (casting direction) for all specimens, showing a tendency to align in the xy plane. Values for x and y directions were similar and didn't show any tendency. Highest orientation was observed in the specimen with fiber volume ratio of 4 % and water - to - cement ratio of 0.30. The orientation state of this specimen is shown on a ternary diagram (Figure 4.13).

Table 4.3: Fractional intrinsic conductivity values for x, y and z directions.

	Fiber volume, %	f_x	f_y	f_z
w/c = 0.30	**1**	36.9	35.9	27.2
	2	34.9	34.9	30.1
	4	39.3	39.3	21.3
w/c = 0.35	**1**	36.1	32.7	31.2
	2	35.9	32.7	31.5
	4	37.0	37.0	26.1

The circular data point on the diagram shows the orientation state for the specimen with 4 % fiber volume ratio (w/c=0.30). As can be seen from the figure, the orientation state of this specimen was found between 3-D random and 2-D planar orientations. To compare AC-IS with image analysis, fiber orientation density of this specimen was calculated using tensor description method of image analysis.

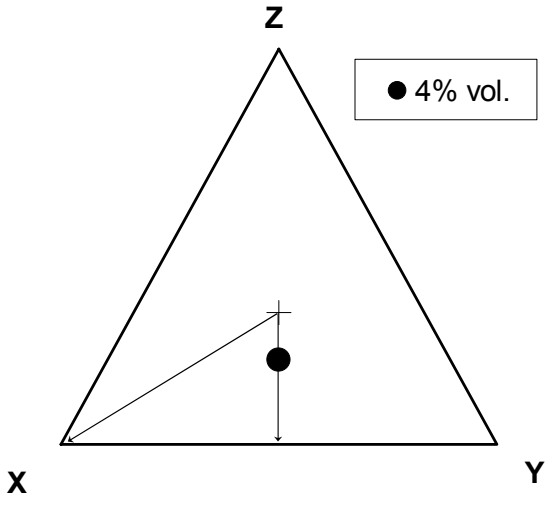

Figure 4.13: Triangular representation of the orientation state of the specimen with 4 vol. % of fiber and water-to-cement ratio of 0.30

A section from this specimen was used to study fiber orientation with image analysis. The total number of fibers on the section was approximately 6000 (xy section). Considering the time and labor intensity associated with the image processing, it was decided to choose a representative amount of sub-sections out of the entire cross-section, and carry out analyses on these sub-sections. Approximately 2500 fibers were examined for the orientation density analysis.

To be able to obtain representative results, the section was first visually inspected. As a result of visual inspection it was found that the fiber orientation in the vicinity of the wall was clearly different than the inner part of the section. Thus, it was decided to analyze the inner and outer sections separately. When the section was visually inspected, it was seen that the wall effect was apparent within 10-12 mm (approximately 2 times of the fiber length) of the wall. Thus the section was divided into equal sub-sections of 12.7 mm, and analyses were done on selected sub-sections, as can be seen in Figure 4.14.

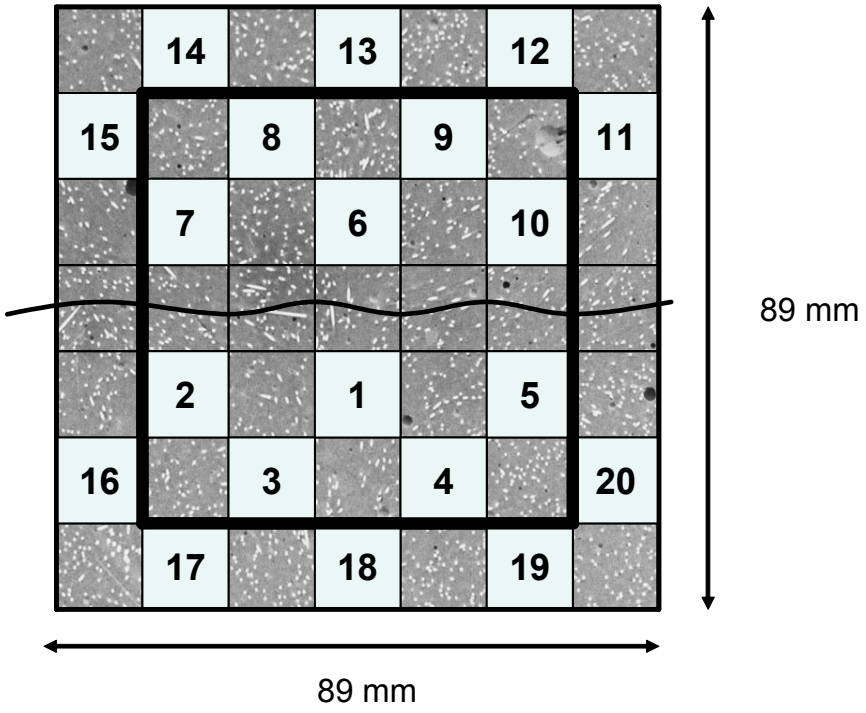

Figure 4.14: Schematic of the examined cross-section

In Figure 4.14, the region framed with a thick border line represents the inner part, and outside of this region shows the outer section. The parts that are numbered show the sub-sections that were chosen for orientation density calculations. Please note that the section under consideration was cut into two parts and ground prior to analysis (fiber clumping analysis), causing some material loss, so it was not possible to carry out analysis in the center position of the section. Fiber orientation densities were calculated for the 20 selected sub-sections, and the orientation densities for reference directions were plotted.

Figure 4.15 shows the fiber orientation densities in the reference directions for the inner and outer sections. The inset of Figure 4.15 (a) shows a schematic of the section, with the numbers representing the analyzed sections. As it seen in Figure 4.15 (a), fibers tend to align in the x direction in the inner part of the section. However, in the vicinity of the wall (outer section), large variations were observed.

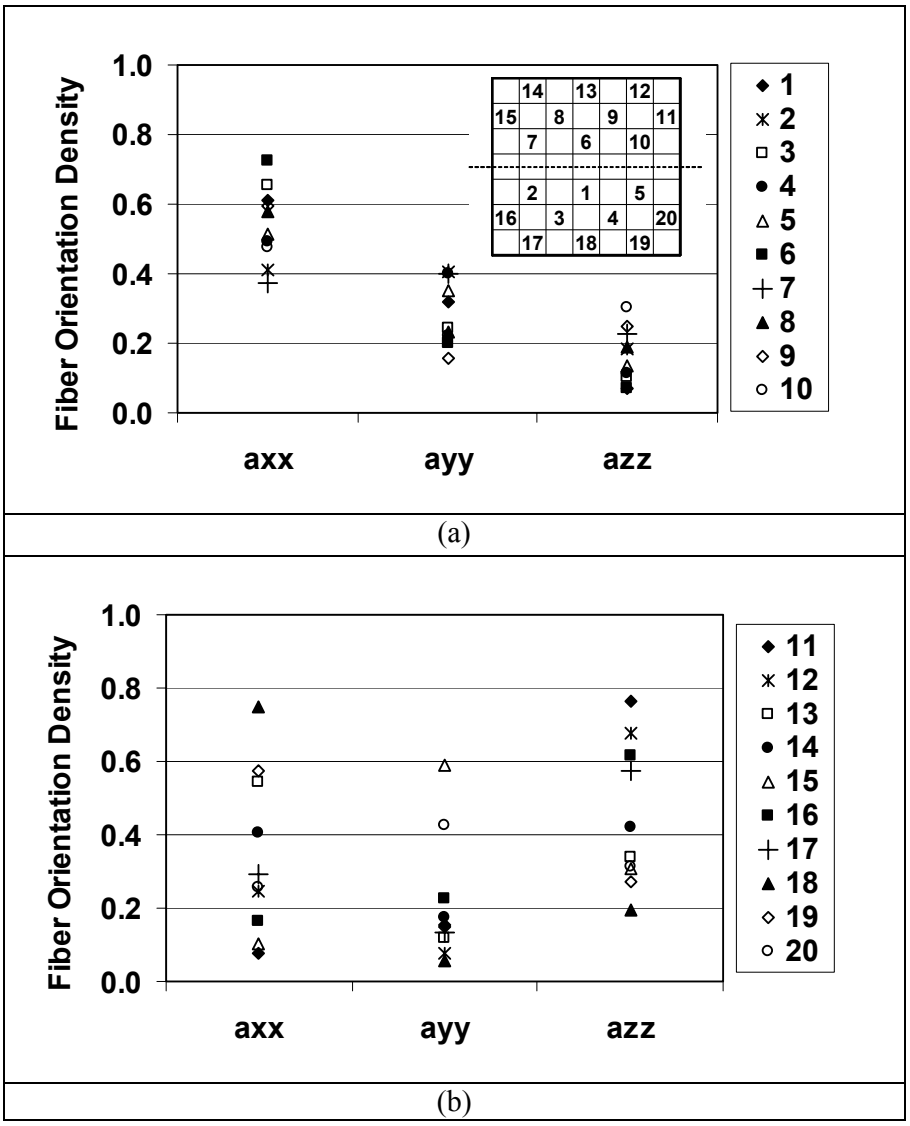

Figure 4.15: Fiber orientation density distribution in reference directions in the a) inner and b) outer section

Figure 4.15 demonstrates the high variations of fiber orientation in different sub-sections. Variations went up to 90 % meaning that small sections were not representative of the entire section. To obtain a general description of the entire section with image analysis, sub-sections were analyzed together, fiber orientation densities in reference directions were calculated, and the results were plotted together with fractional intrinsic conductivities from AC-IS in Figure 4.16. Fractional intrinsic conductivities are shown on the left vertical axis, and fiber orientation densities are shown on the right vertical axis.

.

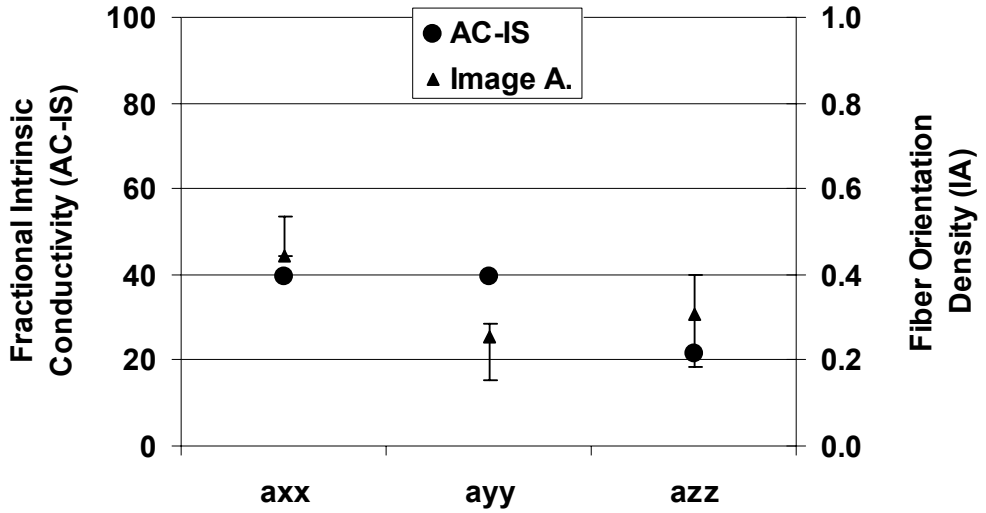

Figure 4.16: Fractional intrinsic conductivity (primary axis) and fiber orientation density (secondary axis) distributions

Results from the two methods agreed well within experimental uncertainty. Both methods showed low alignment in the casting direction (zz). AC-IS showed equal alignment in x and y directions, while image analysis results gave higher alignment in the x direction. Differences between the two methods were expected because they were quite dissimilar in their measurement and analyzing techniques. For image analysis, only one cross-section was analyzed for the specimen, and it was assumed that this cross-section represented the entire specimen. To obtain results with higher precision, more cross-sections throughout the specimen could be investigated. However, the main goal of this study was to compare the results of AC-IS with a fundamental technique (i.e., image analysis) to verify the sensitivity of AC-IS as a dispersion monitoring technique. Therefore, the analysis done was believed to be sufficient to show the amenability of AC-IS for fiber dispersion monitoring.

While evaluating results, it should be considered that the AC-IS measurements were obtained from the entire volume of the specimen. With image analysis it was possible to get 3-D data for each and every fiber. However, the area or the number of fibers analyzed should be large enough to be representative of the entire section/specimen. It can be seen in Figure 4.15 that when small sub-sections were analyzed separately, high variations were observed. In this study for one specimen, over 100 micrographs were obtained, and 2500 fibers were analyzed to ensure that

the data was representative of the entire section, which made the process very intensive and time consuming. On the other hand, with AC-IS measurements a general description of fiber orientation was obtained simply by making 3-D orientation measurements for a given specimen.

4.5 Conclusions

A series of experiments were carried out on fiber-reinforced cement paste specimens to better understand the ability of AC-IS for fiber dispersion monitoring. Different dispersion issues such as fiber orientation, fiber segregation and fiber clumping was studied using AC-IS and the results were quantified. AC-IS was found to be sensitive to the different dispersion phenomenon. Measurements in the fresh and hardened states were obtained and the results were compared. It was found that AC-IS can be used in the fresh state to obtain dispersion characteristics of FRC materials. Image analyses were carried out on the same specimens to understand the extent to which AC-IS predicts fiber dispersion issues. Results of the two methods were found to be comparable confirming the amenability of AC-IS to detect different dispersion issues in fiber-reinforced cement-based materials. The two methods were evaluated by means of time and labor intensity and damage made to the specimen.

5. FIBER DISPERSION - EXPERIMENTAL STUDY: PART II

5.1 Introduction

Chapter 4 discussed the sensitivity of AC-IS to monitor various dispersion phenomenon on lab-scale FRC specimens. AC-IS was found to be sensitive to all dispersion phenomenon. However, it was important to understand the applicability of AC-IS on larger-scale specimens if it is to be used for industrial applications. For this purpose, the use of AC-IS on a precast fiber-reinforced self-compacting concrete beam is discussed in this chapter. Fiber orientation throughout the beam is studied using AC-IS and image analysis. Mechanical tests are also performed and the results are given.

5.2 A Large Scale Application of AC-IS

A pre-cast fiber-reinforced concrete beam was used to study preferred orientation of fibers using AC-IS. A pre-cast concrete company (CON/SPAN Bridge Systems) supplied a FRC beam that had been manufactured at their plant. The beam was cast and tested under four point bending by the company prior to be sent to the lab. (Only a part of the whole beam was used for convenience of transportation and experimental study). CON/SPAN Bridge Systems provided the information regarding the materials and their properties. The fiber-reinforced beam was cast with self-compacting concrete using 1 % Dramix RC 65/60 (L=60mm, AR=65) steel fibers. The dimensions of the full beam were 25.4 x 15.2 x 400cm (10"x6"x13').

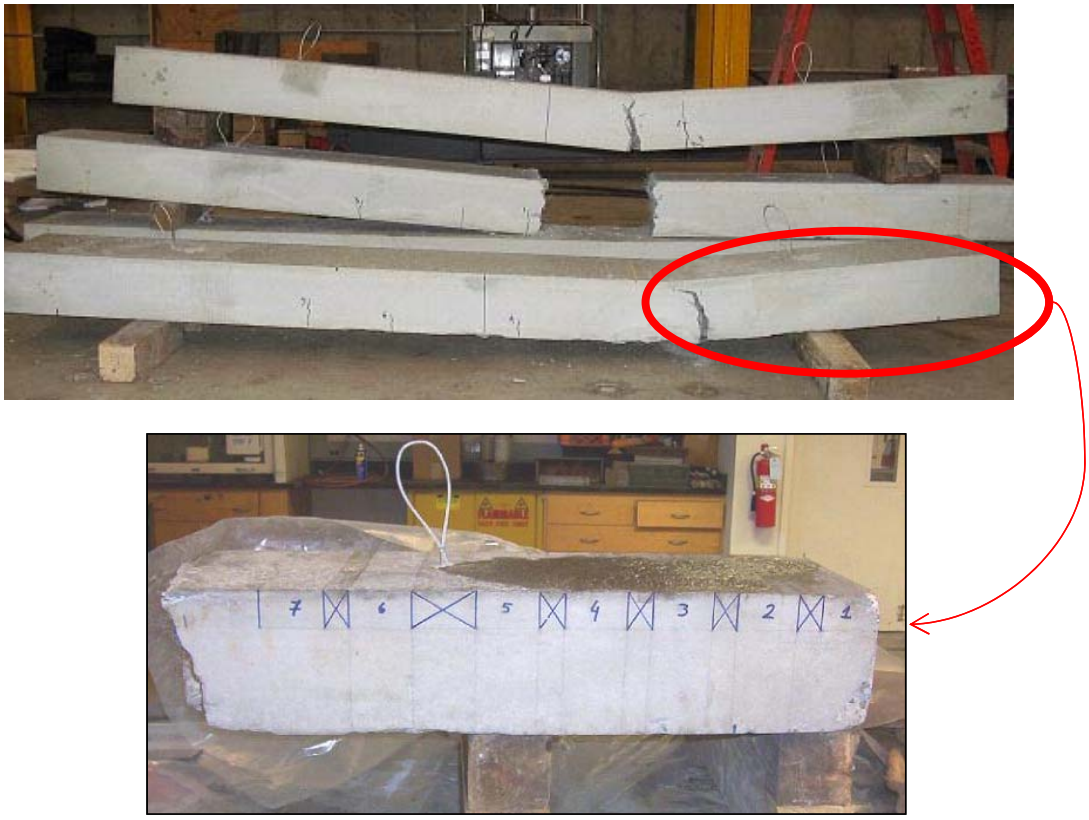

Figure 5.1: Studied part of the precast beam

Figure 5.1 shows the beam after being tested under 4-point bending. The right side of the beam, with a length of 71cm (2´4´´) was used for the orientation tests. First, AC-IS tests were carried out on the beam. Then, the beam was cut and image analysis and splitting tensile tests were done.

AC-IS Experimental setup

Figure 5.2 shows the experimental setup for the AC-IS measurements. Stainless steel circular electrodes with radii of ~59mm (2.3") were used on top of the specimen. These electrodes were submerged in highly conductive NaCl aqueous solutions, but were not in direct contact with the beam surface. Several electrode configurations were examined and this configuration was found to be the most effective for this particular specimen and fiber geometry. Artificial reservoirs were created using sealing putty and filled with 1 M NaCl solution to provide good contact of electrodes and the specimen. A Solartron 1260 impedance/gain-phase analyzer was used, and the frequency was stepped from 100 mHz to 11 MHz under a voltage excitation of 1V.

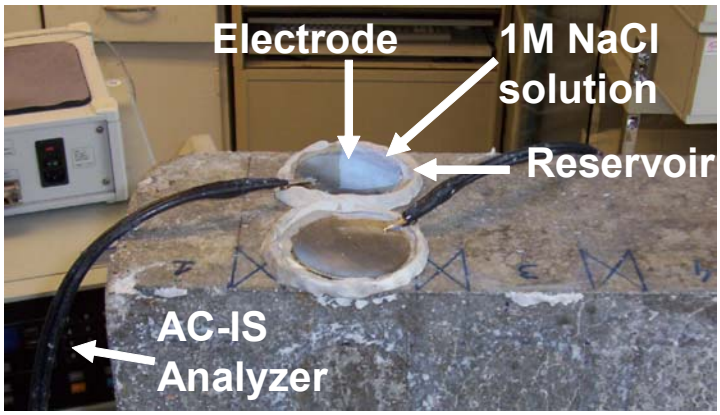

Figure 5.2: AC-IS experimental setup

AC-IS measurements were obtained from both the X and Z directions for all 7 regions. Figure 5.3 shows the electrode positions and approximate current paths for the X and Z directions. Measurements were repeated 2 times to confirm the reproducibility of the results.

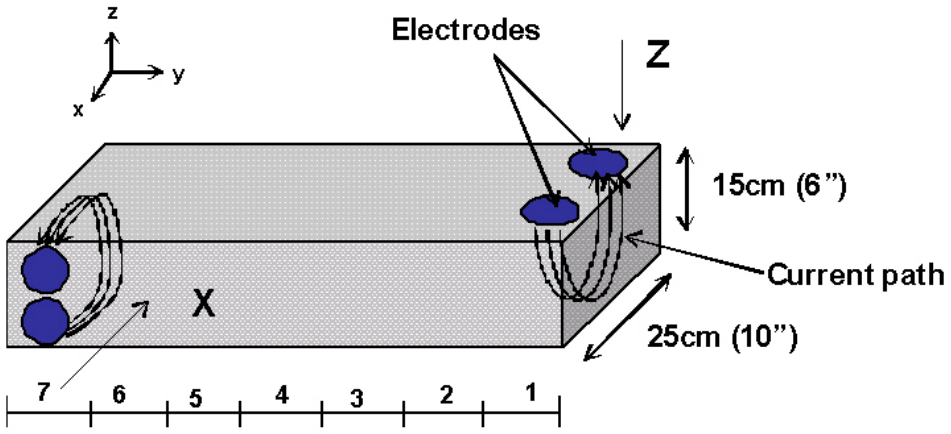

Figure 5.3: Schematic of measurement directions and approximate current paths for X and Z directions.

Figure 5.4 shows the normalized conductivity profiles for the X and Z directions. The X axis shows the measurement points on the beam. Conductivity was found to be higher in the X direction than in the Z direction, suggesting preferred orientation of the fibers in the XY plane. This observation is expected, since previous studies have shown that fibers tend to align in the plane that is vertical to the casting direction [70].

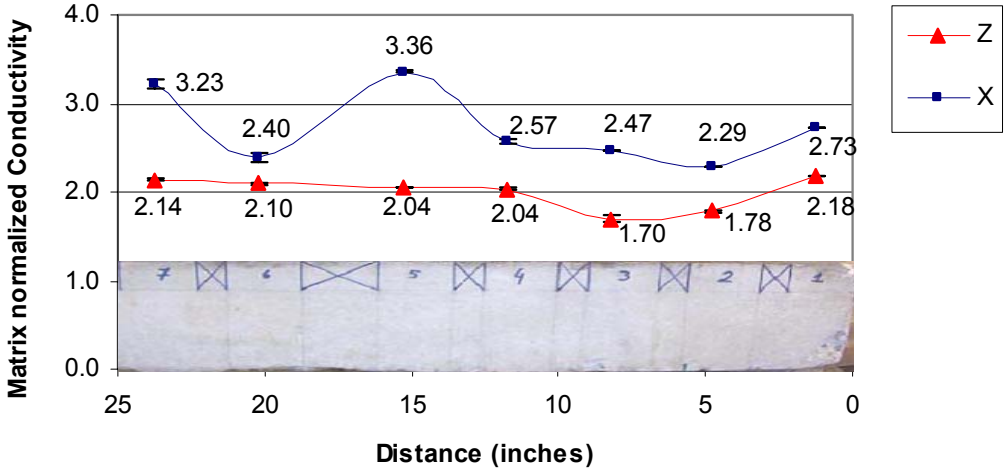

Figure 5.4: Matrix-normalized conductivity profile of the beam for X and Z directions.

Another possible reason for variations in the matrix-normalized conductivity values can be variations in fiber contents at different parts of the beam. To check for this effect approximate fiber contents in different parts of the beam were determined and were found to be similar independent of location along the beam. Details are given in the next section. To further study these findings, image analysis and mechanical tests were conducted on the specimen and the results are given in the next sections.

5.3 Image Analysis

A straightforward technique was used for image analysis. First, the beam was cut into 7 pieces, with the approximate dimensions of 8.9 x 15.2 x 25.4cm (3.5"x 6"x 10"), as seen in the left hand side of Figure 5.5 (the segments are numbered from 1 to 7). Then, each piece was cut into 2 parts vertically (Part a and Part b) with the dimensions of 8.9 x 12.7 x 12.7cm (3.5"x 5"x 5") to be used for image analysis and mechanical testing. 2.54cm (1") from the top of each specimen was removed using a saw to smooth the specimen surface for splitting tensile tests. The number of fibers on XY and ZY planes was counted for each piece. A schematic of studied planes are shown shaded in the right hand side of Figure 5.5.

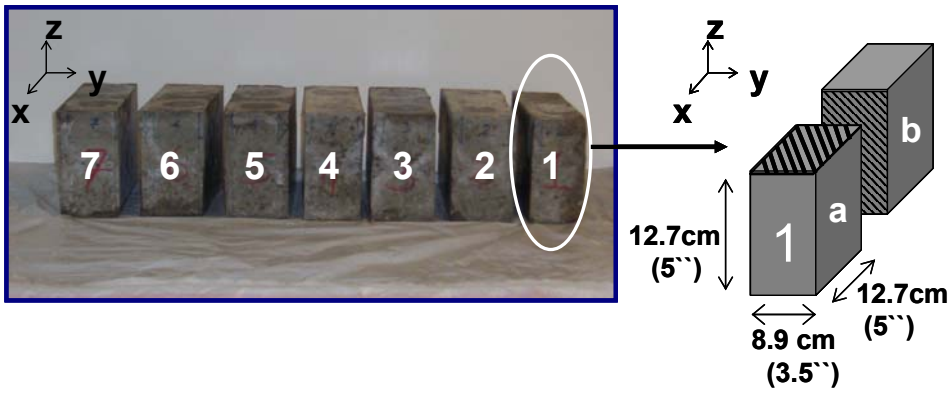

Figure 5.5: Studied specimens with section numbering.

Figure 5.6 shows XY and ZY planes of beam part 2. As seen in Figure 5.6, the number of fibers on the XY plane is noticeably smaller than on the ZY plane, indicating a preferred alignment of fibers in the XY plane, as suggested by AC-IS measurements. Another reason for having fewer fibers on the XY plane could be segregation of fibers since the studied plane was close to the top surface. To check for this effect, specimen cross-sections were visually examined and no sign of fiber segregation was observed.

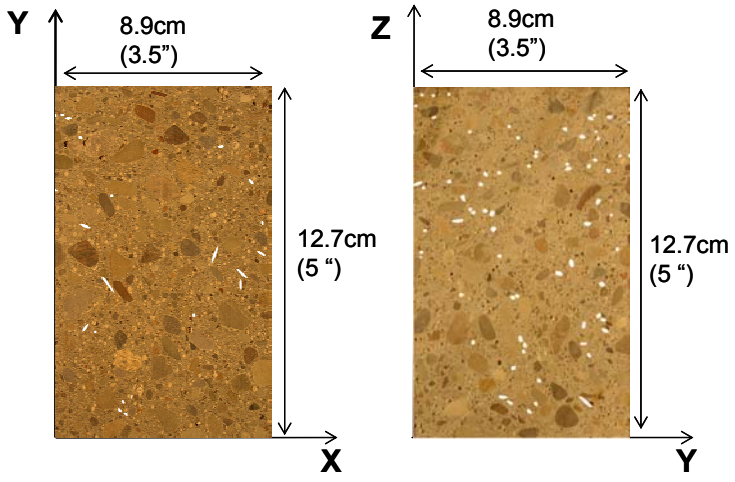

Figure 5.6: The pictures of XY and ZY planes for the beam part 2

The number of fibers on a cross-section depends on the orientation of fibers in the plane. A relationship between the number of fibers and the orientation number is given as follows [71]:

$$\eta_{\varphi} = \frac{N_f * A_f}{V_f} \qquad \textbf{(5.1)}$$

Where;

η_{φ} : Orientation number

N_f : Number of fibers per unit area, ($1/mm^2$)

A_f : Cross-sectional area of a single fiber, mm^2

V_f : Fiber volume fraction (vol., %)

The numbers of fibers on the XY and ZY planes were counted to be able to calculate orientation numbers for each beam part using Eq. 5.1. Figure 5.7 presents the results from these calculations for each part of the beam. Higher orientation number means more fibers oriented perpendicular to the plane under consideration. For instance, in Figure 5.7, higher orientation numbers on the ZY planes means preferred orientation of fibers in the X direction. As was expected, the orientation numbers were found to be lower in the Z direction, in agreement with AC-IS findings.

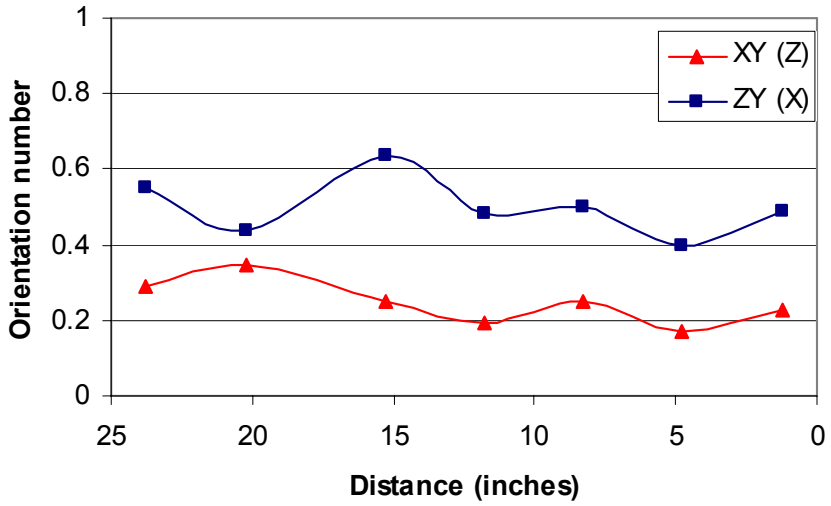

Figure 5.7: Orientation numbers for X and Z directions

When Figure 5.4 and Figure 5.7 are compared, similar tendencies are observed. Both AC-IS and image analysis show preferred orientation in the XY plane. Orientation number profiles show very similar peaks and valleys with the matrix-normalized conductivity profiles, confirming AC-IS results.

In this section (IA) and the previous section (AC-IS), the variations in matrix-normalized conductivity and orientation number values were attributed to the preferred orientation of fibers. Another reason for variations in these values may be differences in fiber content throughout the beam. To check for this effect, fiber contents in different parts of the beam were calculated. The number of fibers at each XZ face was counted (Figure 5.8), after the beam was cut into 7 parts. Fiber content was found to be similar in each part of the beam. The number of fibers per unit area varied 7 % from the average. On the other hand, normalized conductivity and orientation number values varied around ± 20 %, suggesting preferred orientation of fibers in the beam.

Figure 5.8: Number of fibers on the XZ planes throughout the beam

Figure 5.9 shows the orientation number versus matrix-normalized conductivity relation, indicating a linear relationship, with an R^2 value of approximately 0.83.

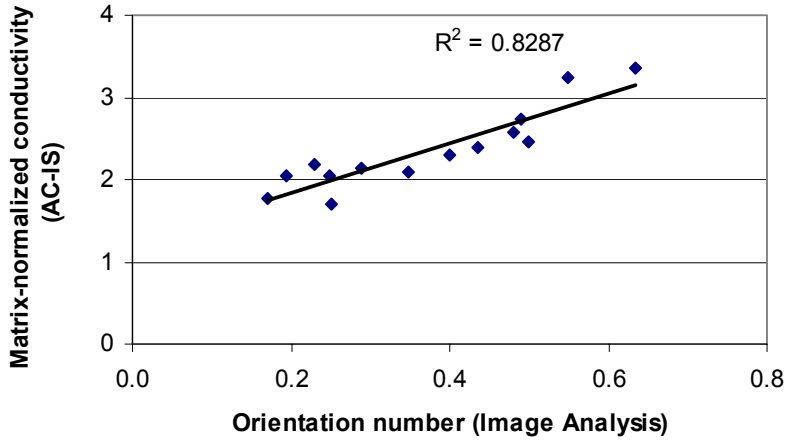

Figure 5.9: Matrix-normalized conductivity versus orientation number

5.4 Mechanical Tests

Splitting tensile tests and 3-point bending tests were conducted on the beam parts to study the effects of fiber orientation on mechanical properties. The beam was cut into 7 pieces and then each piece was divided into two parts (Part a and Part b), with the dimensions of 8.9 x 12.7 x 12.7cm (3.5``x 5``x 5``), as was shown in Figure 5.5. Part (a) was loaded in the Z direction while part (b) loaded in the X direction for each sample as shown in the right hand side of Figure 5.10.

Splitting tensile tests were conducted according to a modified version of EN-12390-6. A closed-loop MTS testing machine was used with a 500kN (110kip) capacity load cell. Loading was applied under average lateral displacement control, which was monitored using 2 LVDTs (Linear variable displacement transducer) that had a maximum range of 2.5mm. The LVDTs were fixed onto each side of the specimen and the lateral displacement was monitored.

Initially, loading was applied at a rate of 0.00025mm/sec. After the maximum stress was reached, the rate was increased to 0.001 mm/sec (for the sake of time). Testing continued until a 2mm lateral displacement was reached. Load and LVDT displacements were recorded for data analysis.

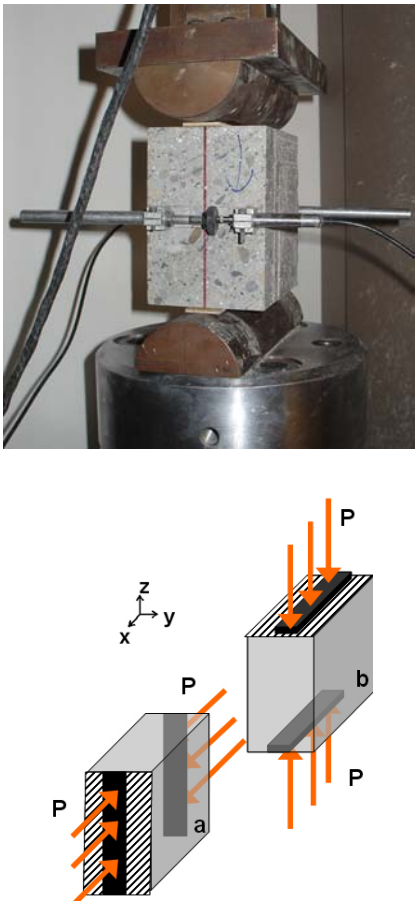

Figure 5.10: Splitting tensile test set up with two LVDTs on each side.

Tensile strength values were calculated using Eq. 5.2, and the splitting tensile strength profile of the beam was obtained (Figure 5.11).

$$f_{ct} = \frac{2P}{\pi LD} \qquad (5.2)$$

In Eq. 5.2, f_{ct} is stress (MPa), P is the maximum load (N), L is the length of the line of contact of the specimen (mm), D is the cross-sectional dimension (mm) of the specimen.

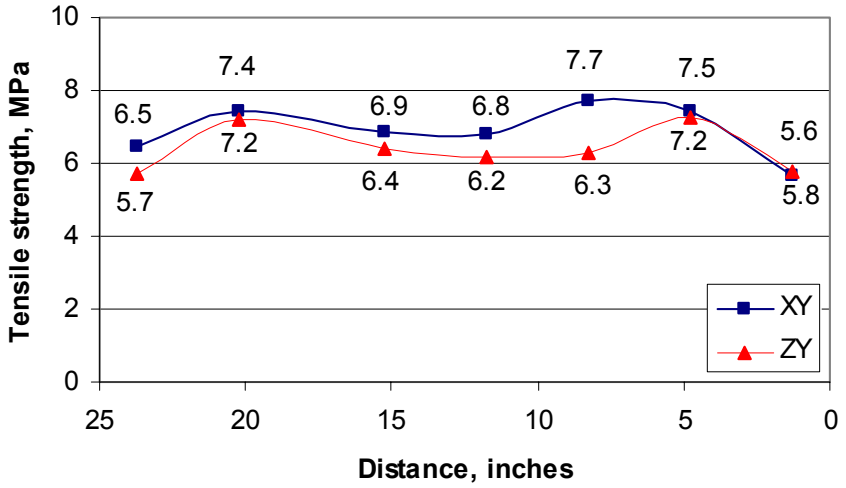

Figure 5.11: Tensile strength profile of the precast beam

When the specimen was loaded in the X direction the fibers aligned on the XY plane are effective in arresting cracks. When loaded in Z direction, fibers on the ZY plane are the effective fibers. The number of fibers oriented in XY had been found to be higher than the number of fibers oriented in YZ plane. This may be the reason for the slight difference between the splitting tensile strength profiles in Figure 5.11.

Three point bending tests were carried out to study the mechanical performance in the X and Z directions. Specimens with the dimensions of 2.5 x 2.5 x 12.7cm (1``x 1`` x 5 ``) were cut out of the beam Part 2, 5, and 6 and tested in the X and Z directions. The reason for using small beams was the limited number of specimens. A notch with a depth of 10mm (40 % of entire depth) was cut and an extensometer was used to measure CMOD. A closed-loop MTS testing machine was used. Loading was applied under CMOD control. Three replications were made for both the X and Z directions.

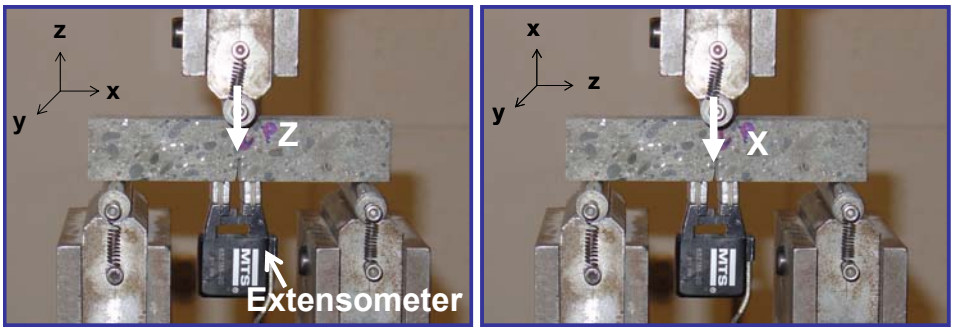

(a) (b)

Figure 5.12: Small beam specimens were tested in the a) Z and b) X directions

Figure 5.13 shows the load versus CMOD curves for beam part 6. As seen in the figure when the load applied in the X direction, the specimen behaves in a very brittle manner due to the lack of the fibers in the Z direction. On the other hand when load is applied in the Z direction, the specimen fails in a ductile manner owing to the fibers aligned in the X direction. Similar trends were obtained for other parts of the beam.

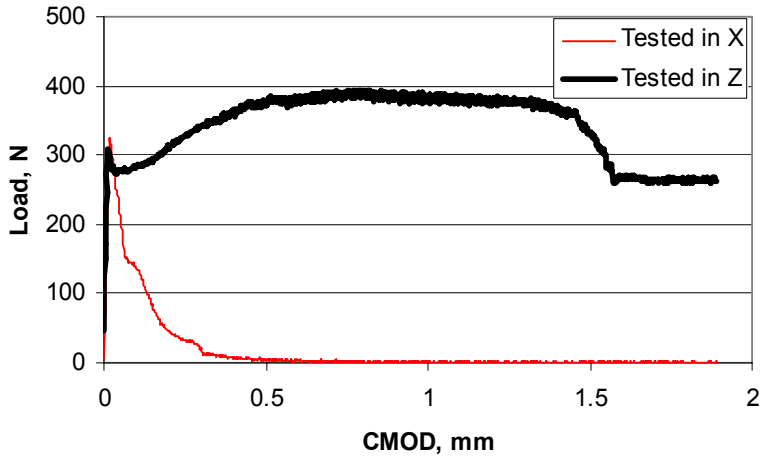

Figure 5.13: Load versus CMOD relations from 3-point bending test.

Flexural strength values were calculated for the X and Z directions using Eq. 5.3. In Eq. 5.3, $\sigma_{flexural}$, is stress, M is moment, c is the distance from the edge to the center, I is moment of inertia, P is the load, L is the length of the specimen span, w is the specimen width, and d is the specimen depth.

$$\sigma_{flexural} = \frac{Mc}{I} \qquad \left(M = \frac{PL}{4},\ I = \frac{1}{12} wd^3\right) \tag{5.3}$$

The average ratio of splitting tensile strength values to the flexural strength values in the X direction (Eq. 5.4) was calculated and found to be 0.67. This ratio and the observed flexural strength values were employed to estimate the splitting tensile values in the Z direction. This estimated profile is plotted together with Figure 5.11 and is given in Figure 5.14.

$$\left(\frac{\sigma_{splitting}}{\sigma_{flexural}}\right)_X = 0.67 \tag{5.4}$$

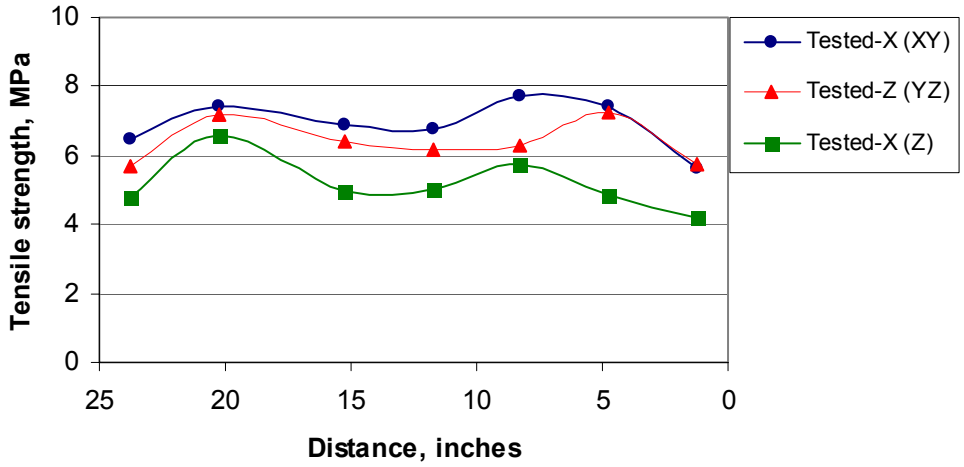

Figure 5.14: Tensile strength profiles of the precast beam.

In Figure 5.14, the legend shows the direction in which the specimen was tested and the direction of the fibers that are effective in arresting crack development. For instance, the closed circle data points were for samples in the X direction and the fibers aligned in the (XY) plane were effective in arresting the cracks. As seen in Figure 5.14, the lowest values were obtained in the Z direction. Mechanical test results are consistent with the results of AC-IS and image analysis measurements. This means that preferred orientation of fibers negatively affect mechanical performance of FRC components.

5.5 Conclusions

In this section AC-IS was used to study fiber orientation state in a precast self compacting FRC beam to understand the ability of AC-IS for fiber dispersion monitoring in structural components. Precast SCC beam was provided by CON/SPAN Bridge Systems. AC-IS measurements were obtained from two directions and the matrix-normalized conductivity profiles were obtained. Fibers were found to be aligned vertical to the casting direction. Image analysis was also performed on the sections of the beam and orientation number profiles were obtained. Orientation number profiles were compared with matrix-normalized conductivity profiles and very similar tendencies were observed confirming the results of AC-IS measurements. Mechanical performance of the beam in reference directions was also studied by means of splitting tensile tests and 3-point bending tests. Fiber orientation was found to affect mechanical performance. From the results of this section, it can be concluded that AC-IS is a good candidate to be employed for non-destructive monitoring of fiber dispersion issues in FRC components.

6. RHEOLOGY – DESIGN and CALIBRATION of the NEW RHEOMETER

In this section design and calibration of parallel plate rheometer is explained. Design considerations are discussed. Governing equations are given, and the modeling of wall effect is presented. Experimental protocol is described. Calibration of the rheometer using standardized high-viscosity oil and a conventional rheometer (Haake RheoStress 150) is discussed. The values obtained from the parallel-plate rheometer are compared with results from the commercial rheometer and values from the literature. Values from the new rheometer are found in the same range with values reported in the literature.

6.1 Rheometer Design

Rheometer design was done by Edward Mu. The intent of this work was to design a rheometer that can evaluate the rheological behavior of stiff fiber-reinforced cement paste and mortar systems. With this in mind, a number of considerations were made while selecting the rheometer configuration. First, an adequate gap size was required so that fibers and sand particles could be included in the mix. Next, the occurrence of plug flow and wall slip, testing artifacts that can lead to underestimated rheological parameters, needed to be minimized. Finally, for the rheometer to be able to shear stiff materials, a high torque capacity motor was needed.

Based on these design considerations, a parallel plate setup (shown in Figure 6.1:) was selected [72]. The two plates are 254 mm in diameter, with an adjustable gap. The rheometer is equipped with a high torque capacity motor, capable of approximately 20 N*m. The upper plate is rotated at a controlled speed. The shear rate varies along the radius of the plates, reducing the occurrence of plug flow. Square grooves, measuring 6.3 x 6.3 x 2.5 mm, are machined onto the two plates to minimize slip. A plexi-glass wall surrounds the bottom stationary plate to prevent material from flowing away during testing, which will introduce a frictional effect that will influence the rheological measurements. To reduce the effect of the wall, a

large diameter to gap ratio was used (typically greater than 10). The rheometer is attached to a data acquisition system for continuous monitoring during testing.

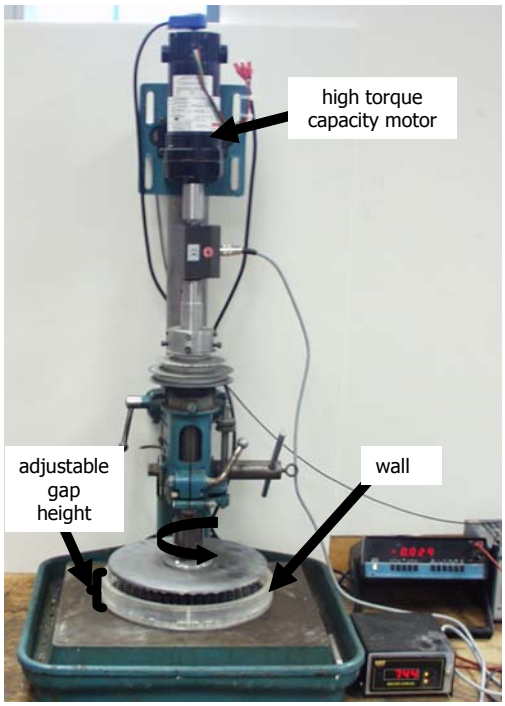

(a)

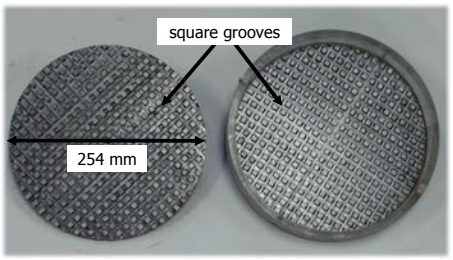

(b)

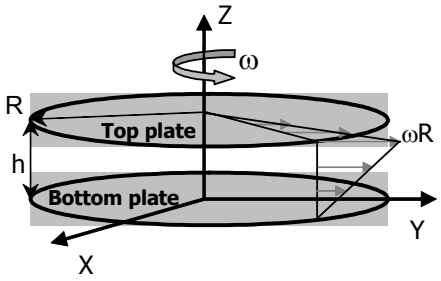

(c)

Figure 6.1: Parallel plate rheometer built: (a) rheometer, (b) plates with square grooves and (c) velocity distributions

6.2 Governing Equations

Without a wall, the shear rate, $\dot{\gamma}$ (s^{-1}), between the two plates, is a function of the radius, r (m), and gap height, h (m):

$$\dot{\gamma} = \frac{r\omega}{h} \qquad \textbf{(6.1)}$$

where ω is the rotation rate at the top of the plate (rad/s). For this rheometer, the gap height is assumed to be the clear distance between the grooves. The viscosity of the material can be explicitly expressed as [73]:

$$\eta(\dot{\gamma}_R) = \frac{(T/2\pi R^3)}{\dot{\gamma}_R}\left[3 + \frac{d\ln(T/2\pi R^3)}{d\ln\dot{\gamma}_R}\right] \qquad \textbf{(6.2)}$$

where $\eta(\dot{\gamma}_R)$ is the shear rate dependent viscosity (Pa·s), T is the resistant torque (N·m) and $\dot{\gamma}_R$ is the apparent shear rate (shear rate at r=R, with R = radius of plate (m)). For a Bingham material, this relationship can be described as a function of rheometer geometry, rotation speed and torque:

$$\frac{T}{\frac{2}{3}\pi R^3} = \tau_0 + (\frac{3}{4}\frac{R}{h}\omega)\mu_0 \qquad \textbf{(6.3)}$$

where τ_0 is the Bingham yield stress (Pa) and μ_0 is the Bingham viscosity (Pa*s).

If a cylindrical wall is attached to the stationary bottom plate, it will remain static during the test. From a microscopic viewpoint, there will be an interfacial layer between the wall and the measured material. Various authors have proposed the following model to describe this phenomenon [74]:

$$\tau = \tau_{0,i} + \eta_0 v_g \qquad \textbf{(6.4)}$$

where τ is the shear stress (Pa), $\tau_{0,i}$ is the interfacial yield stress (Pa), η_0 is the interfacial viscous constant (Pa*s/m) and v_g is the sliding velocity (m/s). Then, the total torque required should be a summation of the resistant torque by the measured material, and the resistant torque by the cylindrical wall (v_g is assumed to be linearly distributed along the gap):

$$\frac{T}{\frac{2}{3}\pi R^3} = (\tau_0 + \frac{3h}{R}\tau_{0,i}) + (\frac{3}{4}\frac{R}{h}\omega)(\mu_0 + \frac{2\eta_0 h^2}{R}) \qquad \textbf{(6.5)}$$

From the torque - rotation relationship, the Bingham parameters, τ_0 and μ_0 can be obtained, if the boundary conditions of the wall are known. Equation 6.5 suggests that the wall effect is more significant as the gap height increases.

6.3 Experimental Determination of the Wall Effect

Rheology experiments were performed together with Dr. Katherine Kuder. To understand the influence of the wall on the rheological measurements, the flow

behavior of a standardized known-viscosity oil (Cannon N15000 viscosity standard: 66 Pa*s at 20 ^{o}C) was evaluated. Using Eq. (6.2), the viscosity was measured at a variety of gap heights. The lowest gap height corresponded to a clear distance between the grooves that was equal to twice the total groove height (10 mm), since the teeth effect will become more pronounced at lower gap heights.

Figure 6.2 presents the measured viscosity as a function of gap height. As the model predicts, the viscosity increases with increasing gap height, due to the wall effect. Based on Eq. (6.5), a second order polynomial curve is fit to the data. By obtaining the viscosity at a gap height of zero, the wall effect is theoretically eliminated. Experimentally, the value of the polynomial curve at a gap height of zero, minimizes the effect of the wall. Here, the polynomial curve fits the data well and predicts a viscosity of 66.71 Pa*s, with an error of approximately 1%. To minimize the total number of experiments, an optimal range was selected in which the wall effect (more pronounced at larger gap heights) and teeth effect (more pronounced at lower gap heights) should be minimized. This range was estimated to be between 10 and 13 mm. Gap height was kept between these values during the experiments.

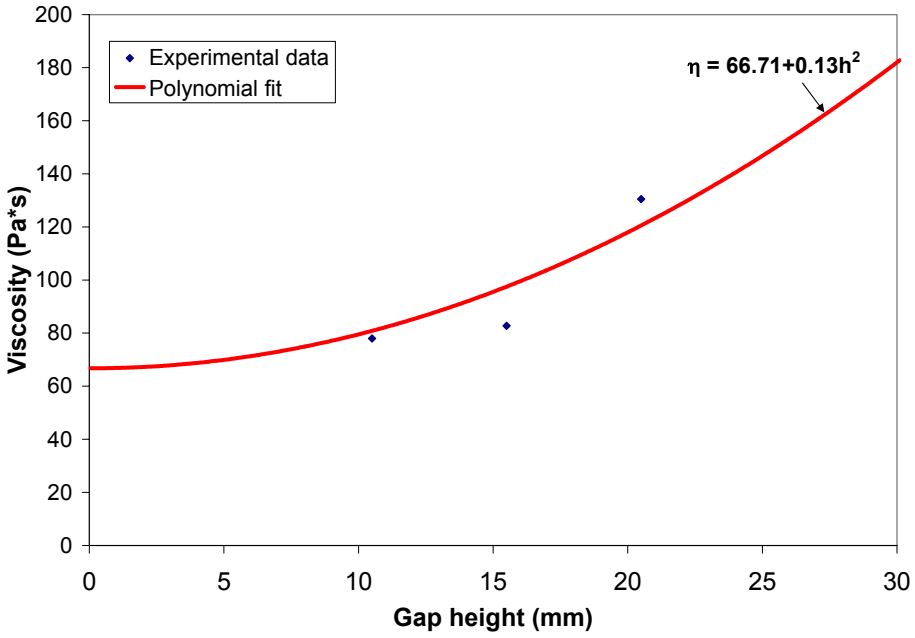

Figure 6.2: Minimization of wall effect with polynomial curve fitting

6.4 Rheological Protocol

The rheological measuring protocol used to obtain the equilibrium shear stress values is shown in Figure 6.3. This protocol is similar to the one proposed by Geiker et. al [75]. At each shear rate, torque measurements were recorded for 20 seconds. The torque at each shear rate was then obtained by averaging the values that corresponded to the equilibrium region. To ensure that a steady-state condition was reached, the data from the highest rotation rate was neglected. Torque and rotation speed were converted to shear stress and shear rate. As Figure 6.4 demonstrates, shear stress was plotted as a function of shear rate to obtain the Bingham parameters. The yield stress was determined from the resultant shear stress versus shear rate data for the slowest two shear rates, since the yield stress corresponds to the shear stress at a shear rate of zero.

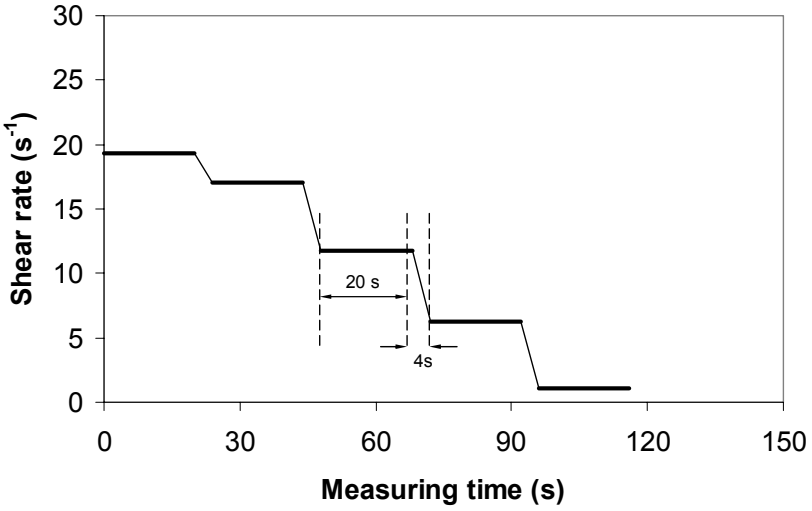

Figure 6.3: Rheology measuring protocol

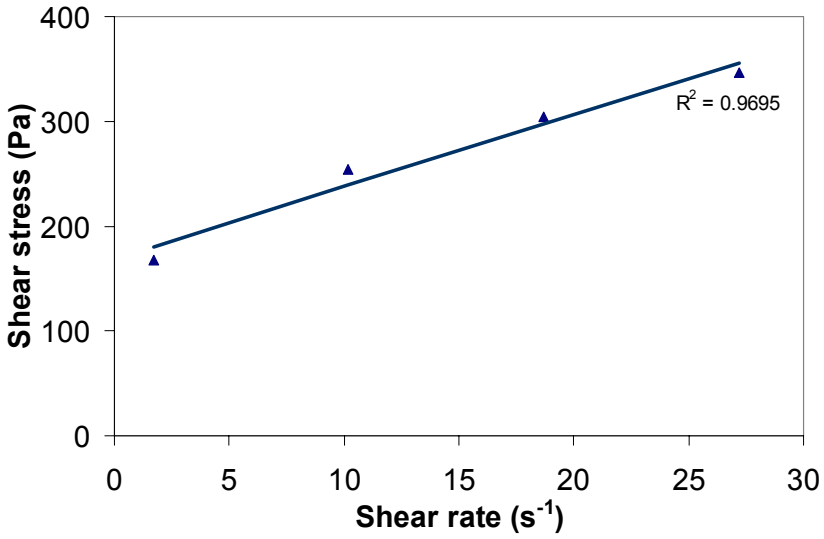

Figure 6.4: Example of shear stress vs. shear rate behavior with Bingham fit to data

6.5 Comparison of Parallel Plate Rheometer, a Commercial Rheometer and Values in the Literature

To verify that the rheological measurements obtained with the parallel plate rheometer were reasonable, measurements were compared with values determined using a commercial rheometer (Haake RheoStress 150) as well as with findings reported in the literature. Figure 6.5 shows Haake RheoStress 150 commercial rheometer.

Figure 6.5: Commercial Rheometer (HaakeRheoStress 150)

The same materials and mixing procedure were used for both the parallel plate and the Haake rheometer. Tests with Haake Rheometer were conducted by Dr. Katherine Kuder and Dr. Bin Mu. Samples were mixed in a Hobart (planetary) mixer. LaFarge Type I portland cement was used. The mixing procedure was as follows: First, the cement was placed in the mixing bowl. Water was added, followed by a 30 second rest. Next, the material was mixed for 30 seconds on the lowest speed. Then, the mixer was stopped and there was a 30 second rest, during which the bowl was scraped to collect any undistributed material. Finally, the material was mixed for 1 minute at the medium speed.

Neat cement pastes, with water/cement ratios (w/c) = 0.30 and 0.35, were tested with both rheometers. Initially, the parallel plate rheometer measurements were to be compared to the results from a commercial rheometer, a Haake Rheostress 150, using the concentric cylinder configuration. Concentric cylinder configuration has two cylinders one inside another. Test material is placed between the two cylinders

and inner cylinder is rotated to shear the material (Figure 6.5). The results, however, were not comparable, with the parallel plate rheometer providing yield stress and viscosity values that were significantly higher than those obtained using the Haake rheometer. It is suspected that this discrepancy is due to the problems of plug flow and slip that are often encountered when using the concentric cylinder geometry [76, 77]. Therefore, the fixturing was changed to the vane configuration, which previous researchers have shown to eliminate slip and plug flow [73, 78, 79]. Figure 6.6 shows vane configuration.

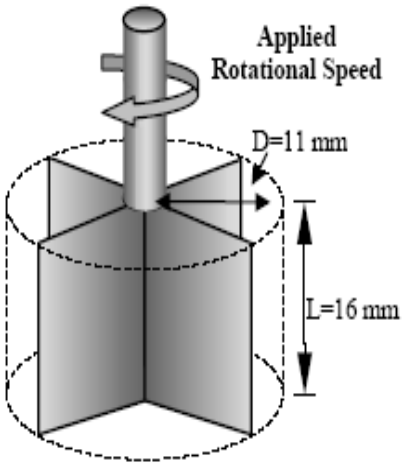

Figure 6.6: Vane configuration of commercial rheometer

Saak et al. compared yield stress values obtained using the concentric cylinder geometry and the vane [77]. For identical cement pastes, a 50% increase in yield stress values was observed due to the elimination of slip and plug flow. With the vane, only a thin layer of unknown thickness, is sheared. Consequently, only rotation rates are known, not shear rates. For this reason, the vane was used to measure yield stress, not viscosity. Both peak and equilibrium yield stress values were obtained using the methodology presented by Saak and colleagues [77].

The parallel plate rheometer was designed to obtain equilibrium shear stress values, using the protocol shown in Figure 6.3. To determine the peak equilibrium stress, the shear stress vs. time behavior was only observed for a single shear rate, approximately 1 s^{-1}. This value is not considered to be the absolute value for the peak yield stress, but is rather shown only to identify the range of yield stress values that could be expected from the parallel plate rheometer for a given material, so that

comparisons with the vane configuration can be made. A comparison of the yield stresses measured with the parallel plate rheometer, the vane and by the other researchers is presented in Figure 6.7. Yield stress values from other researchers represent the range reported in literature, demonstrating the influence of varying materials, rheometer geometries and measuring procedures on rheological findings. Despite the large range seen, the results obtained by the parallel plate rheometer are comparable.

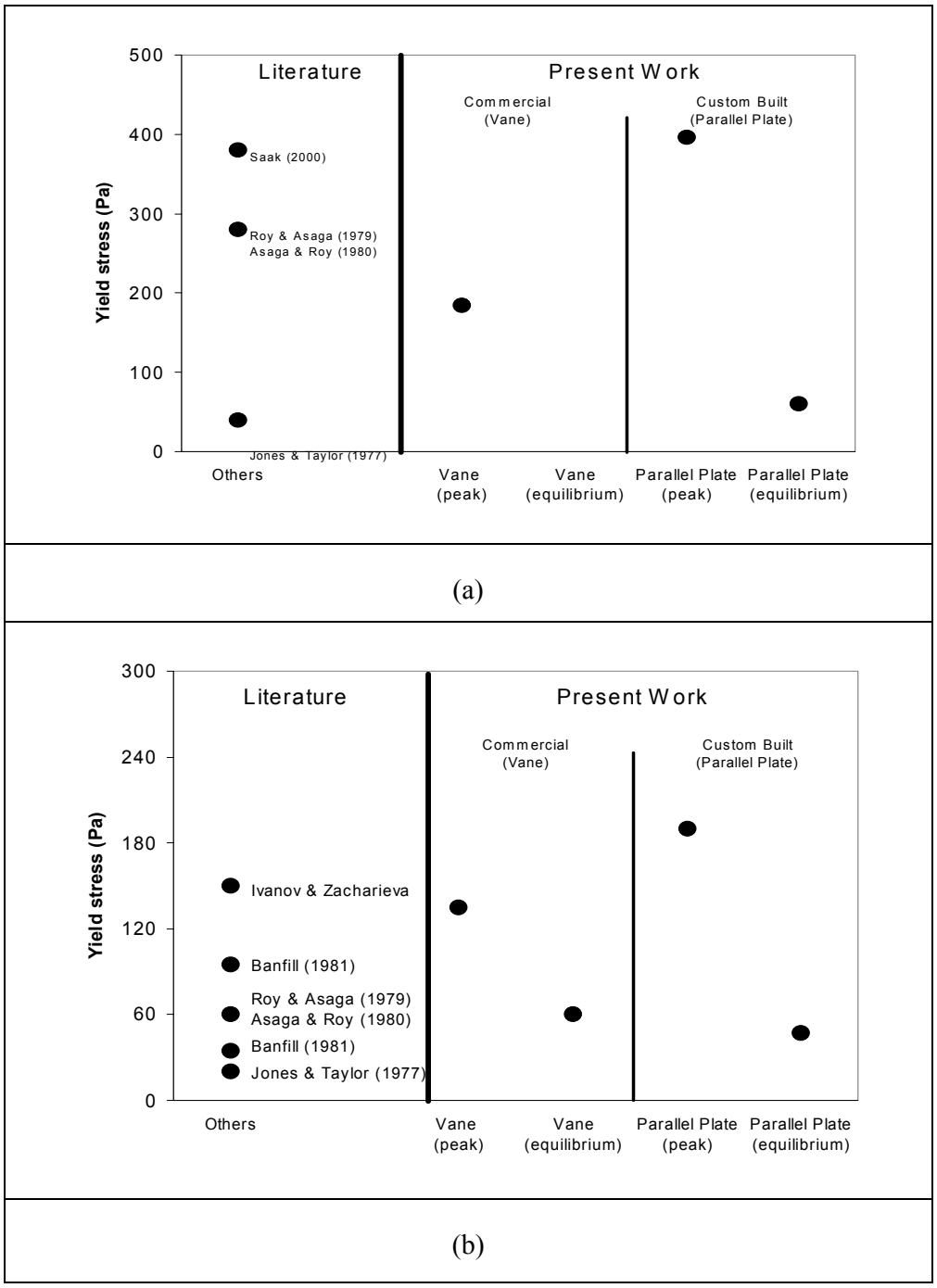

Figure 6.7: Comparison between yield stress values for (a) w/c = 0.30 and (b) w/c = 0.35

6.6 Conclusions

Design and calibration of a parallel-plate rheometer was explained. Design considerations were given. The effect of the plexiglass wall was modeled. Calibration of the rheometer using a standardized viscosity oil and a commercial

rheometer was done. The parallel plate rheometer was found to give reasonable rheological parameters. Measurements using the parallel plate rheometer fell within a reasonable range, when compared with the values obtained from a commercial rheometer and those values reported in the literature. The frictional effect of the rheometer wall was modeled using constitutive relations for the interfacial layer that forms between the wall and the bulk material. According to the resultant model, yield stress and viscosity measurements were found to increase as the gap height increases.

7. RHEOLOGY – EXPERIMENTAL STUDY

The parallel plate rheometer is used to study a variety of cementitious systems. To begin, a testing procedure that gives consistent results with reasonable experimental variation is developed with the neat paste. Then, the influence of water-to-cement ratio and sand on the rheology of cementitious systems is investigated. Finally, the effect of the volume of steel fibers on the rheology of cement paste is studied. Results are discussed and additional experiments are performed to better understand the rheological characteristics of fiber-reinforced systems.

7.1 Reproducibility

To investigate the reproducibility of the measurements made with the parallel plate rheometer, the rheology of two neat cement pastes were examined, with w/c = 0.30 and 0.35. The mixing and measuring protocol described in Section 6.5 were used. After mixing, the fresh cement paste was put into the rheometer with a scraper and then leveled by hand. Three repetitions were made.

Figure 7.1 shows shear stress vs. shear rate relations for three measurements that were done on identical cement paste mixes. As Figure 7.1 demonstrates, utilization of this preparation technique resulted in large experimental variations. Due to the stiffness of the matrices, the surface of the fresh cement paste was uneven, making it difficult to ensure that the top rheometer plate came in complete contact with the material. In addition, differences in void contents from sample to sample could have been large.

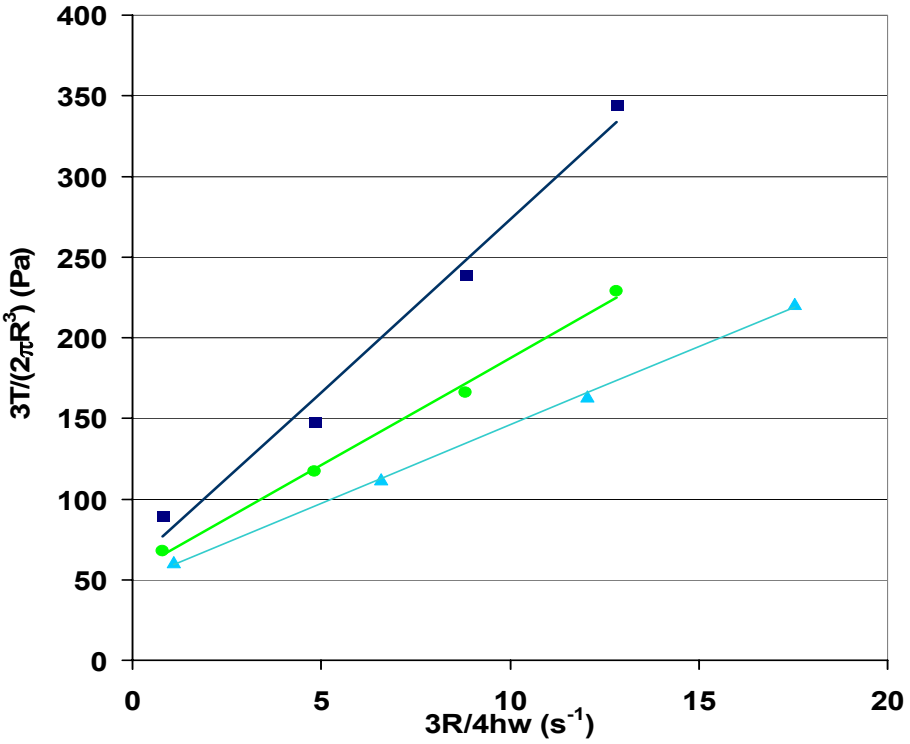

Figure 7.1: Rheological measurements with cement paste without vibration

To investigate the significance of these factors, and to try to reduce measurement variations, the testing procedure was modified. After the fresh sample was placed into the rheometer, a normal compression force of 2.36 kg was applied on the top of the sample as it was vibrated for 10 seconds (Figure 7.2). This procedure was found to make the surface more level. In addition, it is suspected that it also made the void system more uniform.

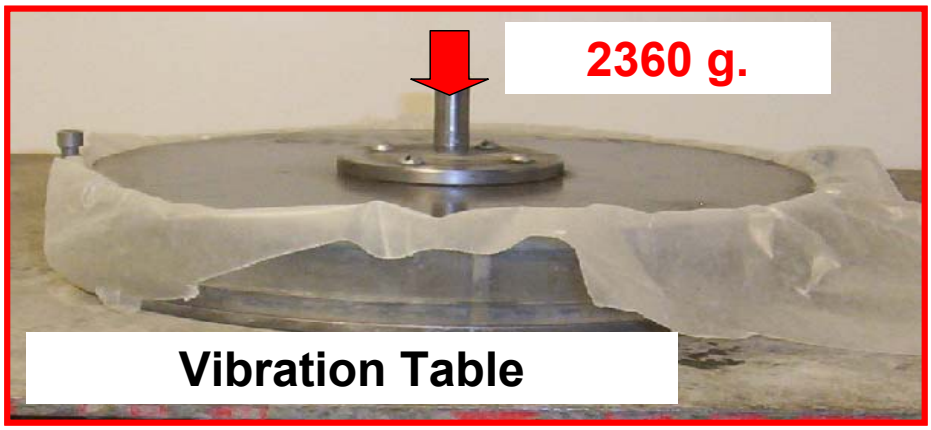

Figure 7.2: Vibration with compression was applied to the test materials

Figure 7.3 shows the improved repeatability of the rheological measurements that is attained for the neat paste with w/c = 0.30 when the vibration and the compression force were applied. Similar results were found with the w/c = 0.35.

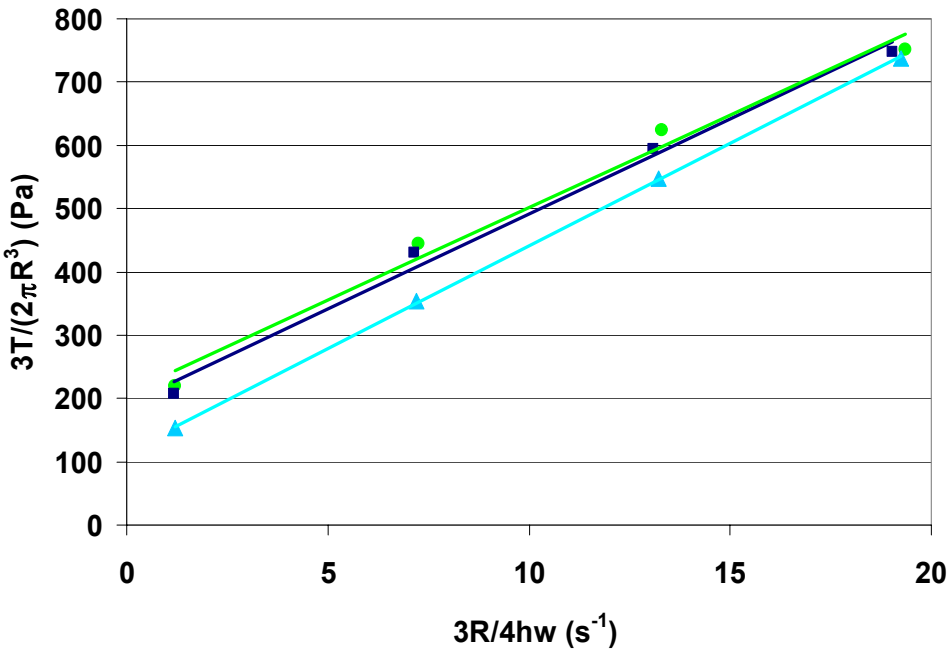

Figure 7.3: Rheological measurements with cement paste with vibration

7.2 Experimental Procedures

Subsequent rheological testing employed the vibratory preparation technique described above. In addition, a more rigorous mixing procedure was used: First, the cement, sand (if applicable) and fibers (if applicable) were placed in a Hobart mixer and mixed for 1 minute at the low speed. Next, water was added and the material mixed for 1 minute at the low speed and then there was a 30 second rest. Finally, the materials were mixed for 2 minutes at the high speed. This procedure was selected because it was found to disperse the sand and fibers well. The rheological measuring protocol given in Figure 6.3 was used. The gap height between the plates was kept between 10 and 13 mm. At least three replications were made for each parameter investigated.

The cement was LaFarge Type I. Short steel fibers, produced by Bekaert, which had a length of 6 mm and a diameter of 0.16 mm, were used. River sand, with a maximum particle diameter of 3 mm was used in the oven-dry condition.

7.3 Results

7.3.1 Effect of water-to-cement ratio

The influence of w/c on the rheological parameters for neat paste was evaluated. Three different neat pastes were studied, with w/c = 0.30, 0.35 and 0.45. As is expected, and Figure 7.4 demonstrates, both the yield stress and viscosity decrease as the w/c increases.

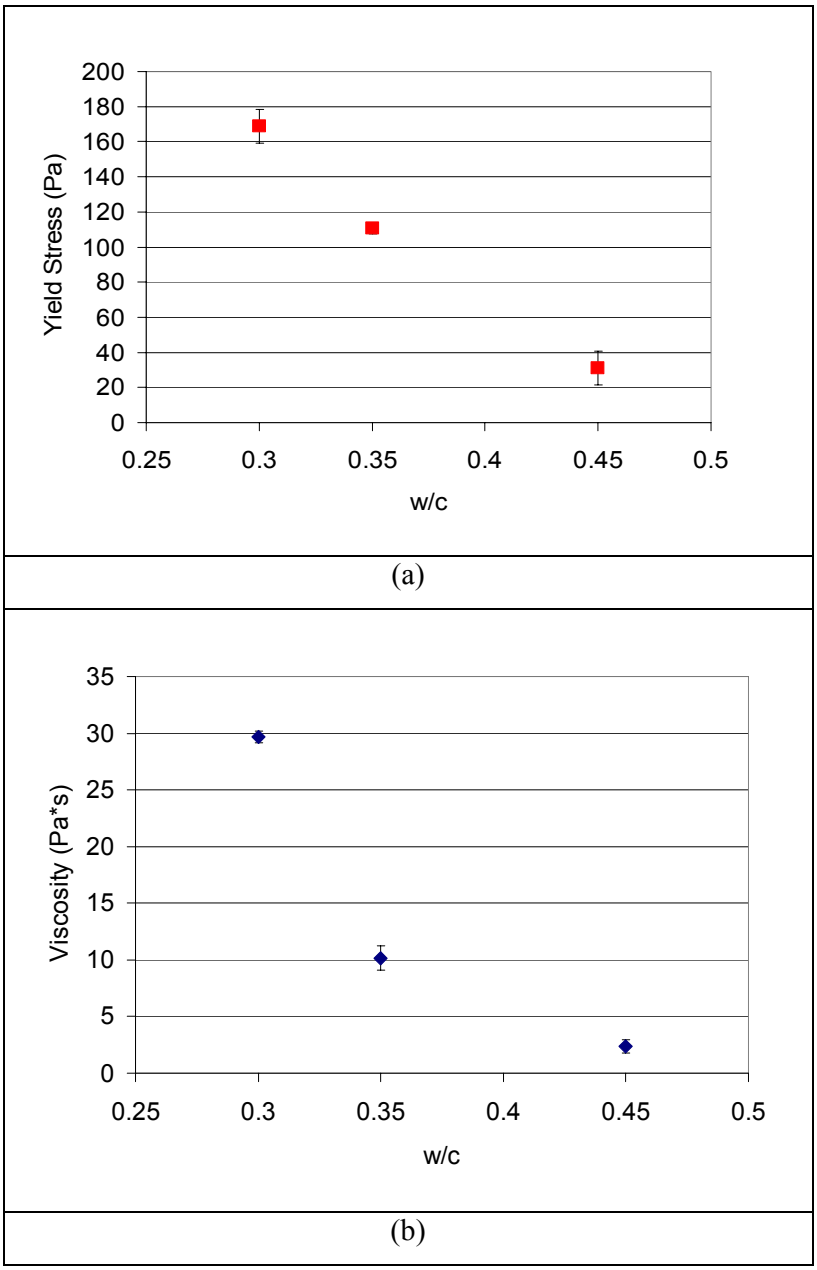

Figure 7.4: Effect of w/c on (a) yield stress and (b) viscosity of neat cement paste with standard deviations

7.3.2 Effect of sand content

Figure 7.5 presents the effect of sand addition on the rheology of cement paste with a w/c = 0.45. Sand was added at 10 and 30 % of the cement weight. Addition of sand has a small influence on the yield stress, but has a significant effect on the viscosity, which increases by more than 4 times, from 0 to 30 % sand.

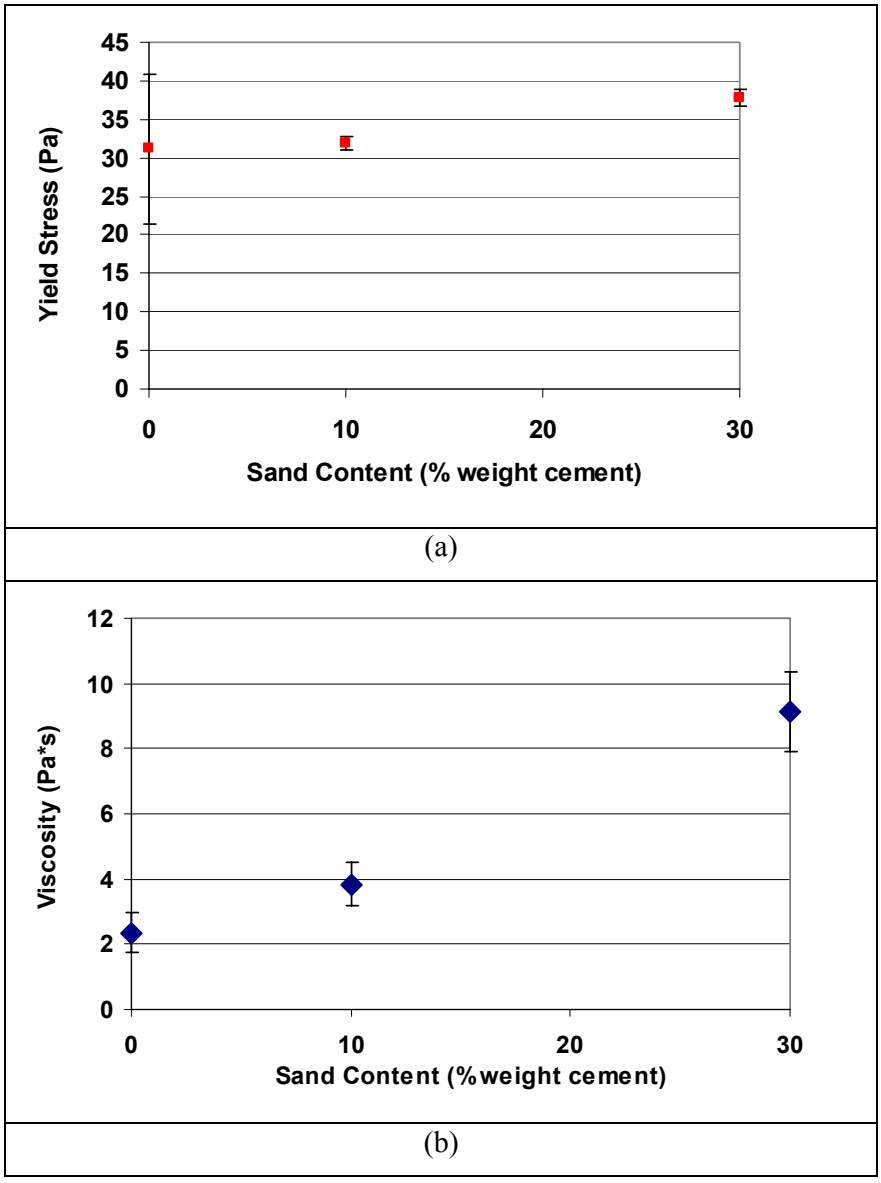

Figure 7.5: Effect of sand content on (a) yield stress and (b) viscosity of w/c = 0.45 cement paste with standard deviations

7.3.3 Effect of fiber content

Finally, the rheology of steel fiber-reinforced cement pastes was determined. Two w/c, 0.30 and 0.35, with three fiber volume contents, 1, 2 and 4%, were studied. Figure 7.6 and Figure 7.7 show the effect of steel fiber volume on the yield stress and viscosity of the neat pastes, respectively. For both w/c, the yield stress decreases until a critical volume fraction is reached, and then increases. The viscosities appear to decrease until reaching a critical point, however, the decrease for the stiffer matrix, with w/c = 0.30, is much greater. At a fiber dosage of 4 %, the yield stress and viscosity are similar for both w/c.

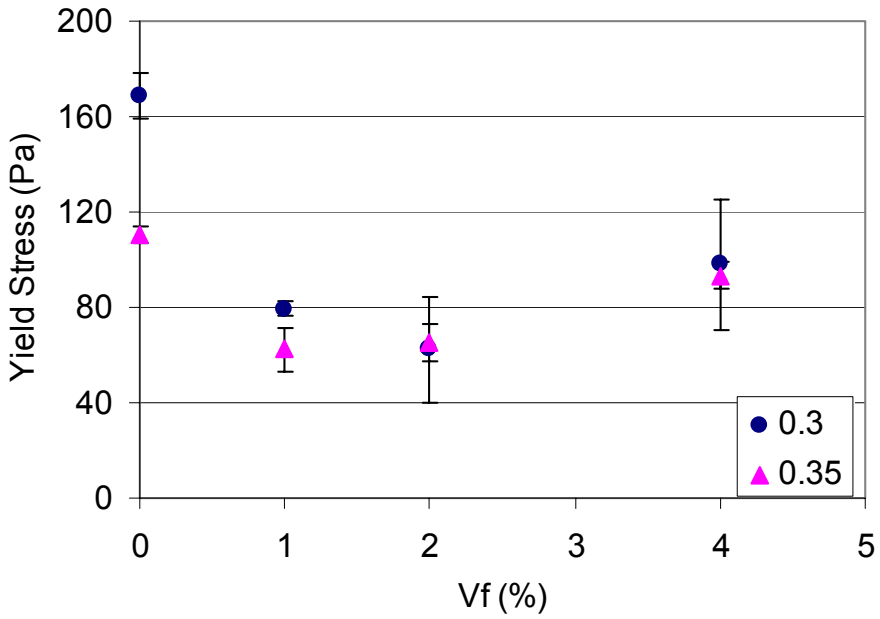

Figure 7.6: Effect of fiber content on yield stress for w/c = 0.30 and 0.35 with standard deviations

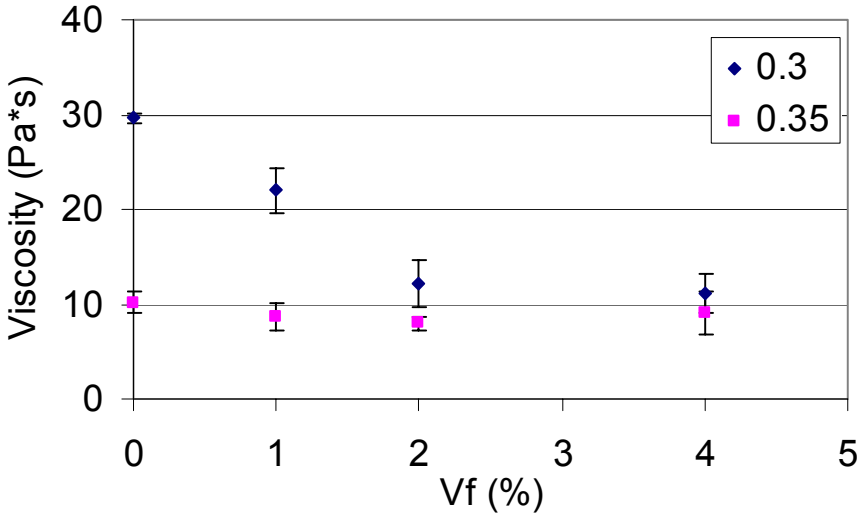

Figure 7.7: Effect of fiber content on viscosity for w/c = 0.30 and 0.35 with standard deviations

7.4 Comparative Analysis

Generally, it is expected that adding fibers will increase the yield stress and viscosity of cementitious materials. However, little research has been done on the rheology of fiber-reinforced cementitious materials, and most of the work has been done on highly fluid concrete or mortar, not on stiff cement paste systems. To evaluate the influence of steel fibers on the rheology of a more fluid material, and to compare rheological measurements from the parallel plate rheometer to those obtained using another custom-designed and built rheometer, the rheology of a highly fluid steel fiber-reinforced mortar was studied. In addition, drop table experiments were conducted.

7.4.1 Rheology of highly fluid steel fiber-reinforced mortar

Previous researchers evaluated the rheology of a highly fluid steel fiber-reinforced mortar using the BML rheometer (concentric cylinder configuration) that was developed by Wallevik and Gjorv [80, 81]. In their work, Bui and colleagues used steel fibers that are similar to the fibers in this study and found that as the amount of fibers increased, the Bingham yield stress and viscosity increased. These experiments were repeated here. The mixture proportions are given in Table 7.1. The mixing sequence reported was used; however, the constituent materials varied slightly and the rheological protocol and rheometer were different. Table 7.2

presents the results of this investigation. The trends observed by the authors are the same as those reported by Bui et al. The absolute values of the rheological parameters are of the same magnitude, but do not match exactly. This discrepancy is expected when using different rheometers and rheology protocols, as discussed previously [82, 83]. This work also demonstrates the potential differences in rheological trends when more fluid materials are investigated.

Table 7.1: Mixture proportions used by Bui and colleagues [80]

w/c	Cement (kg/m^3)	Water (kg/m^3)	Sand (kg/m^3)
0.6	592	355	1184

Table 7.2: Comparison of Parallel Plate and BML Rheometer [80]

	Parallel Plate		Bui and Colleagues	
V_f (%)	Yield Stress (Pa)	Viscosity (Pa*s)	Yield Stress (Pa)	Viscosity (Pa*s)
0	25.6	4.51	16	1
1	27.1	4.82	27	2
2	51.4	5.74	34	3.4

7.4.2 Drop table

Finally, drop table experiments were performed (Figure 7.8). A modified version of ASTM C-109, Standard Test Method for Compressive Strength of Hydraulic Cement Mortars, was used [84]. A frustum mold that is 50 mm in height with a lower diameter of 100 mm and an upper diameter of 70 mm was placed on the drop table apparatus. The material was mixed according the procedure discussed previously, placed in the mold and vibrated for 10 seconds. The mold was then removed and the crank turned manually 25 times, each time vertically displacing the table by 12.7 mm. The diameter of the spread material was then measured at four places. These four values were then averaged to give the flow diameter. Three replications were made for each mix tested.

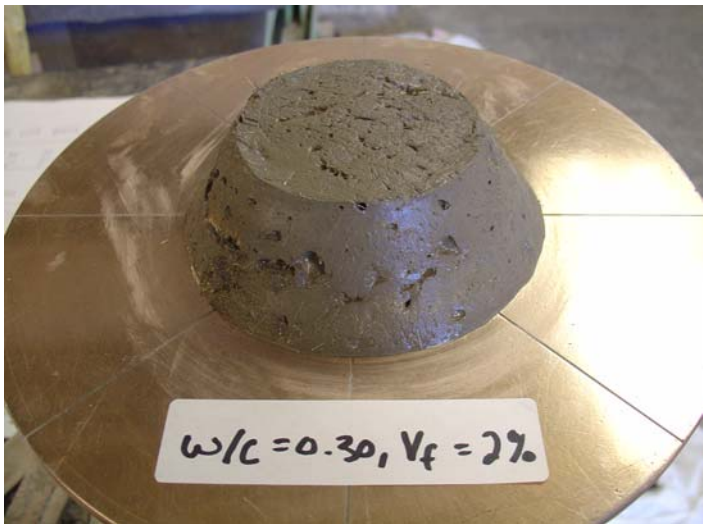

Figure 7.8: Drop table test on the fiber-reinforced cement paste mixes

Table 7.3 presents the drop table results from this test for the fiber-reinforced cement pastes. Similar to the results obtained with the parallel plate rheometer, fibers do not appear to adversely affect the flow behavior of the cement pastes, with the flow diameter not significantly changing due to the fibers. Figure 7.9 presents the inverse of the flow diameter (an indication of yield stress) as a function of the volume fraction of fiber reinforcement for the cement pastes with w/c = 0.30 and 0.35. Generally, the trends observed are similar to those found with the parallel plate rheometer, with the inverse of the flow diameter decreasing as the volume fraction increases until a critical point is reached. However, for the w/c = 0.35, with a 4% addition of fibers, a decrease is seen, which is not expected. Nevertheless, these results do suggest that there is an initial decrease in the yield stress of the material, followed by an increase once a critical volume fraction of fiber reinforcement is reached.

Table 7.3: Drop table results for steel fiber-reinforced cement pastes

w/c	Vf (%)	flow diameter (mm)
0.3	0	12.69 ± 0.40
	1	12.93 ± 0.71
	2	12.9 ± 0.40
	4	12.54 ± 0.57
0.35	0	14.05 ± 0.43
	1	14.81 ± 0.71
	2	13.82 ± 0.21
	4	15.20 ± 0.97

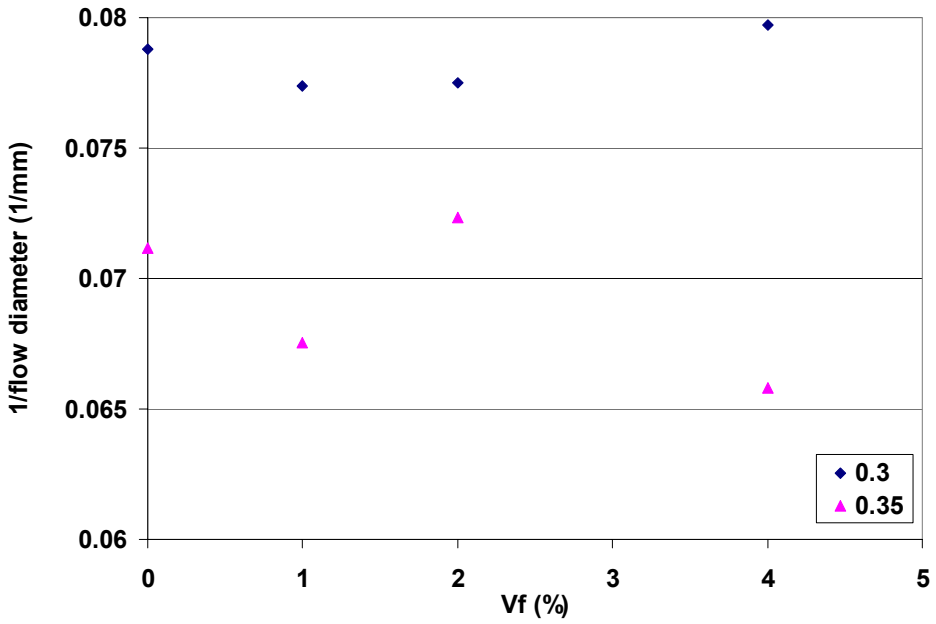

Figure 7.9: Effect of fibers on flow diameter

7.5 Discussion

The results presented here for the steel fiber-reinforced cement pastes are not what are generally expected. It is hypothesized that the initial decrease in Bingham parameters is due to the thixotropic nature of the cement paste. The stiff steel fibers might increase the amount of structural breakdown that occurs during mixing, thus initially reducing the yield stress and viscosity of the material. However, once a certain critical volume fraction of fibers is reached, the mechanical interlocking, or entangling, of the fibers could be dominating the flow behavior. This phenomenon of mechanical fiber interactions has been observed with fiber reinforced polymers [85].

Thus, at lower fiber dosages, the properties of the cementitious matrices are dominant, which is why the yield stress and viscosity are lower for w/c = 0.35 than 0.30. Beyond the critical volume fraction, the absolute values of the Bingham parameters are much closer, regardless of w/c, suggesting that the fiber interlocking is governing the behavior. It is also interesting to note that the critical volume fraction appears to be higher for the w/c = 0.30 than the w/c = 0.35, possibly indicating that a stiffer material undergoes more structural breakdown before reaching the critical point.

7.5.1 Rheology of a newtonian fluid with parallel plate rheometer

To isolate the effect of the mechanical interaction of the fibers, the rheology of a Newtonian fluid was evaluated. Rheological measurements were determined for a commercially available honey with varying dosages of the steel fibers investigated previously. The results from these experiments are shown in Figure 7.10. From 0-2%, the change in viscosity is small; however, between 2 and 4%, a large increase in the viscosity is observed. Thus, there does appear to be a point at which the mechanical interlocking of fibers dominates the flow behavior for both Bingham and Newtonian liquids.

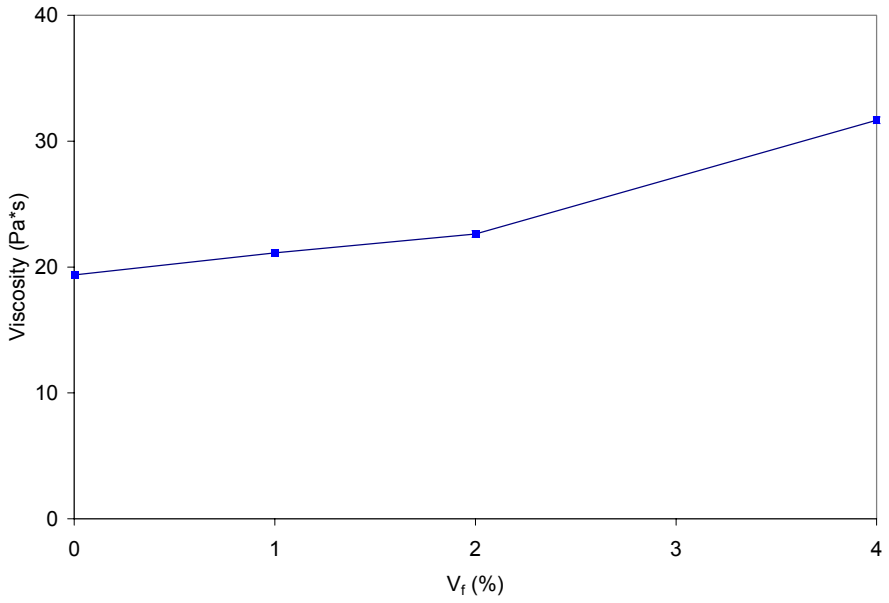

Figure 7.10: Effect of fiber content on viscosity of honey

7.6 Conclusion

A parallel plate rheometer was designed and built to evaluate the rheology of stiff fiber-reinforced cement pastes. Initial studies were conducted to verify that the rheometer worked properly. Finally, the rheology of a variety of cement paste systems was studied, including stiff steel fiber-reinforced cement pastes. With stiff cementitious materials, high variations in yield stress and viscosity measurements are seen when vibration is not applied, most likely due to the uneven surfaces of the samples and the differing void contents. Repeatability can be improved by applying vibration with normal compression to the sample before testing. For the steel fibers investigated, the Bingham rheological parameters decrease until a critical volume fraction is reached. This trend is explained by a coupling effect between the structural breakdown of the material, which occurs at low fiber volumes, and the mechanical interlocking of fiber, which occurs at higher volume fractions.

8. CORRELATION OF FIBER DISPERSION, RHEOLOGY AND MECHANICAL PERFORMANCE

Fiber dispersion, rheology and mechanical performance relation is studied in this section by means of fiber segregation. Various vibration times are applied to the specimens to study the effects of vibration on fiber segregation. An SCC mix is cast to compare segregation resistance with conventional concrete. Segregation is non-destructively monitored using AC-IS. Splitting tensile tests are performed to study mechanical performance of FRC specimens. The self-designed parallel plate rheometer is used to obtain rheological characteristics of cement matrices. The effects of rheological characteristics on the fiber segregation and consequently on the mechanical performance is discussed.

8.1 Materials and Mix Designs

Fiber-reinforced concrete specimens were cast and various vibration times were applied. LaFarge Type I Portland cement and two types of steel fibers were used. Short-cut steel fibers of 6 mm length and 0.16 mm diameter and longer steel fibers with 40 mm long and 0.62 mm in diameter were provided by Bekaert and used in different mixes. Daracem 19 by Grace Construction was used as water reducing superplasticizer (sp) for all mixes except SCC mix. For SCC, a polycarboxylate-based superplasticizer was used produced by Axim Italcementi Group. Kelcocrete 1376 by CP Kelco was used as a viscosity modifying agent (vma).

River sand with maximum diameter of 3 mm and coarse aggregate with maximum diameter of 8 mm were used. Water-to-cement ratio was kept constant at 0.40. Fiber content was 1 % by volume for all mixes. Concrete mix designs and vibration times are given in Table 8.1.

Seven groups of concretes were produced. Each mix is designated with letters (A, B or C) and vibration times are given as subscript. For example A_2 represents the design with superplasticizer and subscript 2 shows vibration time in minutes.

Table 8.1: Concrete groups and vibration times

Fiber type	Mix design		Vibration time
6 mm fibers w/c = 0.40 Fiber content: 1 %	A_0	sp	No vibration
	A_2		2 min.
	A_8		8 min.
	B_8	sp +vma	8 min.
	C_8	vma	8 min.
40 mm fibers w/c = 0.40 Fiber content: 1 %	A_2	sp	2 min.
	SCC		No vibration

Table 8.2 and Table 8.3 show mix designs for conventional concrete mixes and SCC respectively.

Table 8.2: Conventional concrete mix design

Cement	Water	Fine Agg.	Coarse Agg.	Vma (% water weight)	Sp. (% cem. weight)
1	0.4	2	2	0.2	1

Table 8.3: SCC mix design

Cement	Water	Fine Agg.	Coarse Agg.	Fly Ash	Sp. (% bind. weight)
1	0.4	1.56	1.9	0.25	0.7

8.2 Experimental Work

Three cylinders with dimensions of 15 x 30 cm (6`` x 12``) were cast for each group. One specimen of each group was used for fiber content calculation in the

fresh state, two specimens were left for curing under 100 % relative humidity. Non-destructive AC-IS measurements were carried out on one of these specimens after 3 days and splitting tensile test was done on the third specimen at 14th day. A schematic of experimental program is given in Figure 8.1.

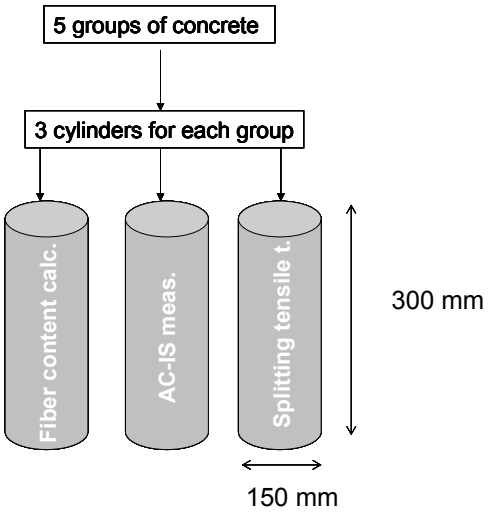

Figure 8.1: Schematic of experimental program

8.2.1 Study of segregation level in the fresh state

One specimen of each group was cut into 4 pieces (immediately after initial set) and fibers washed out in the fresh state and fiber volume ratios in each piece were calculated. Figure shows a schematic of the slicing of the specimens. The slices were notated from a to d beginning from the top of the specimen.

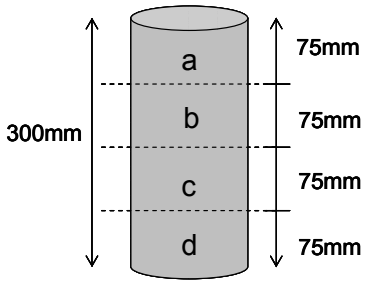

Figure 8.2: Slicing of specimen for fiber content calculation

8.2.2 AC-IS measurements

AC-IS measurements were obtained along the height of cylinders. Electrodes were stepped from top to bottom and measurements were obtained from 4 different positions. Wet sponges were used under stainless steel electrodes to provide a good contact of specimen and electrodes. 1 M NaCl solution was used to wet the sponges.

AC-IS measurements were obtained with a Solartron 1260 impedance/gain-phase analyzer, and the frequency stepped from 100 mHz to 11 MHz under a voltage excitation of 1V. Figure 8.3 shows electrode positions from top to the bottom of a cylinder specimen. Four sections were drawn on the specimens and measurements were obtained from the middle of each section as seen in Figure 8.3.

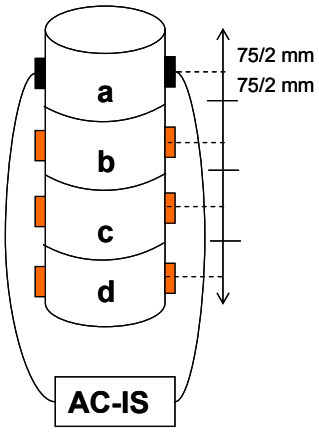

Figure 8.3: AC-IS measurement positions

Figure 8.4 shows resulting Nyquist plots of the specimen made with mix design A_8. As seen in the figure, $R_{matrix}/R_{composite}$ ($\sigma/\sigma m$) ratio decreases as the electrodes are stepped downwards along the specimen.

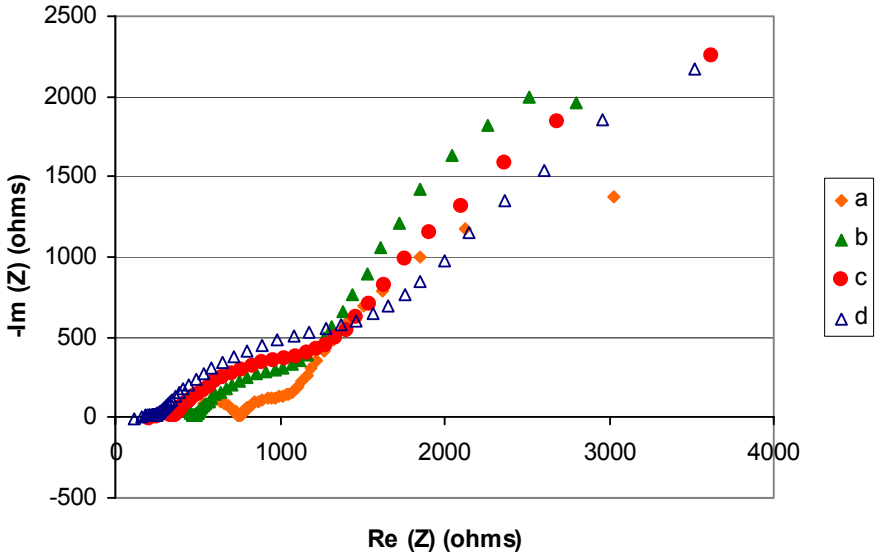

Figure 8.4: Resulting Nyquist plots from AC-IS measurements of the specimen made with mix design A_8

8.2.3 Mechanical tests – splitting tensile tests

Splitting tensile tests were conducted according to a modified version of EN-12390-6. A closed-loop MTS testing machine was used with a 500 kN capacity load cell. Loading was applied under average lateral displacement control, which was monitored using 2 LVDTs (Linear variable displacement transducer) that had a maximum range of 2.5 mm. The LVDTs were fixed onto each side of the specimen and the lateral displacement was monitored. Initially, loading was applied at a rate of 0.00025 mm/sec. After the maximum stress was reached, the rate was increased to 0.001 mm/sec (for the sake of time). Testing continued until a 2 mm lateral displacement was reached. Load and LVDT displacements were recorded for data analysis. Figure 8.5 shows a tested specimen with one LVDT on each side.

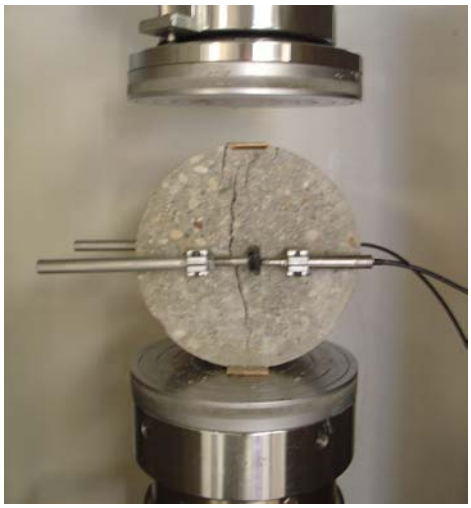

Figure 8.5: Splitting tensile test set up

Tensile strength values were calculated using the equation below,

$$f_{ct} = \frac{2P}{\pi LD} \qquad \textbf{(8.1)}$$

where, f_{ct} is stress (MPa), P is the maximum load (N), L is the length of the line of contact of the specimen (mm), D is the cross-sectional dimension (mm) of the specimen.

8.3 Results and Discussion

8.3.1 Fiber content distributions

Fiber content distributions were obtained for each concrete mix and given in Table 8.4 and Figure 8.6. Segregation of fibers increased with increasing vibration (A_0, A_2, A_8). Mix designs with vma were seemed to be more resistant to segregation even when vibration was applied. The level of segregation seemed to increase when longer fibers were used. Design A_2 with 6 mm long fibers had less segregation when compared to design A_2 with 40 mm long fibers. SCC mix had some segregation, but not as severe as the mix design A_8.

Table 8.4: Fiber content distribution in concrete specimens

	6 mm fibers					40 mm fibers	
	A_0	A_2	A_8	B_8	C_8	A_2	SCC
a	0.99	0.90	0.38	0.89	0.97	0.70	0.92
b	0.99	0.92	1.02	0.88	1.00	0.97	1.19
c	0.96	1.02	1.20	0.97	1.00	0.98	1.08
d	0.89	1.15	1.44	0.98	1.01	1.30	1.13

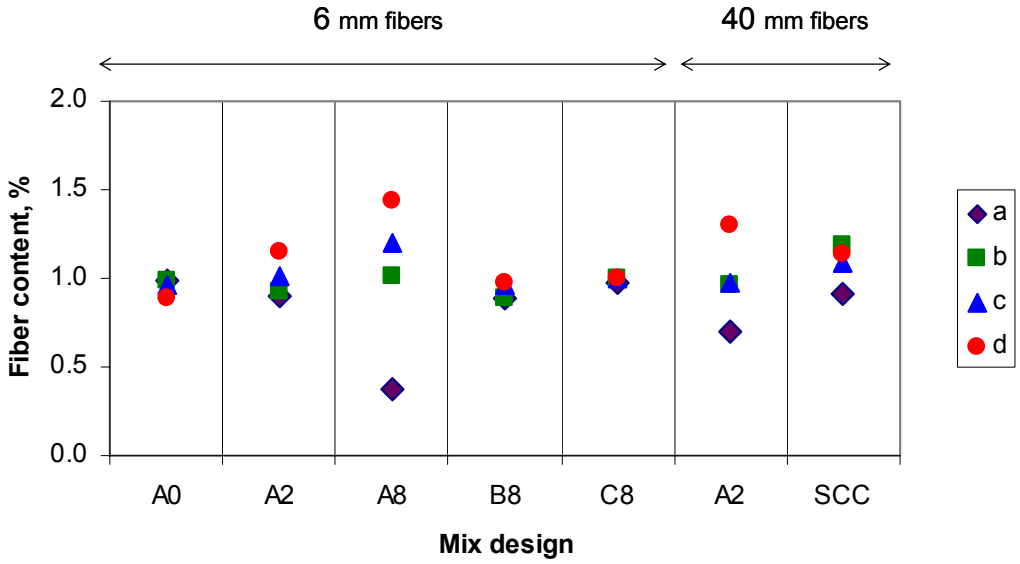

Figure 8.6: Fiber content distribution in concrete specimens

8.3.2 AC-IS

8.3.2.1 The effect of aggregate size – correction of results

AC-IS measurements were obtained and matrix-normalized conductivities were calculated for each section of the specimens. Figure 8.6 shows fiber content distribution in a specimen (mix design A_8), together with observed and theoretical matrix-normalized conductivity values (theoretical values were calculated using observed fiber content values and Eq.3.1). When these values are compared it is seen that the calculated values are excessively high compared to the theoretical values. This result can be attributed to the insulating property of coarse aggregates. Maximum diameter of coarse aggregates is 8 mm, while the

fiber length is 6 mm meaning that coarse aggregates are big enough to block conductive fibers and can cause a reduction of concrete matrix conductivity. This phenomenon can be explained with reference to Figure 8.7.

Table 8.5: Fiber contents in sections and corresponding matrix-normalized conductivity values (observed and calculated) for design A_8

Fiber content, %	σ/σ_m (observed)	Theoretical (calculated)
0.38	1.51	1.45
1.02	2.45	2.20
1.20	3.65	2.42
1.44	4.91	2.70

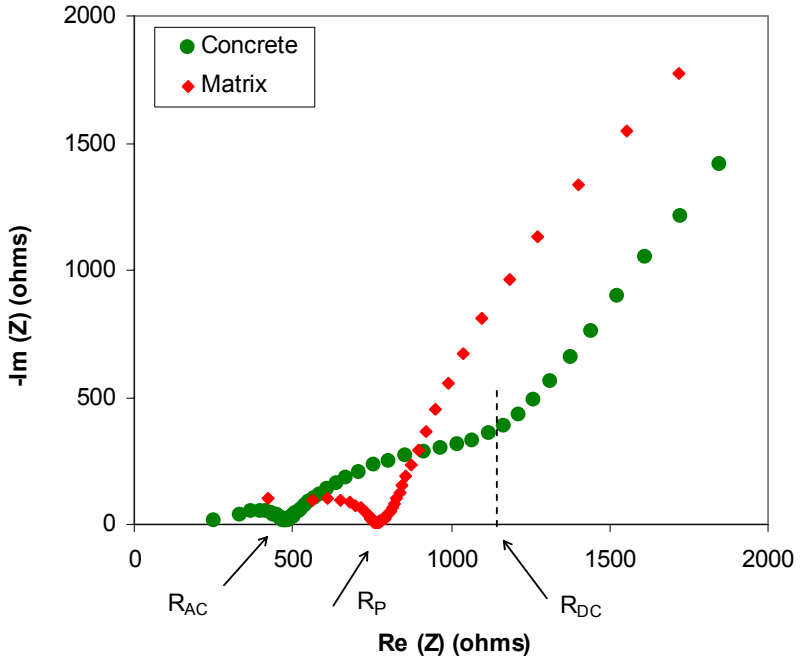

Figure 8.7: Sample Nyquist plots for concrete and cement paste of mix design A_8

In Figure 8.7 impedance curves of mix design A_8 for concrete and cement paste are given. In the figure R_{AC} represents composite resistance, R_{DC} shows concrete matrix resistance and R_p stands for paste resistance. R_{AC} and R_{DC} values were obtained from AC-IS experiments on concrete specimens and R_P values were obtained from AC-IS measurements on cement paste (cement paste specimens of each concrete mix design were cast and AC-IS tests were performed on the

specimens to obtain R_P values). As seen in Figure 8.7, resistance of concrete matrix is higher compared to resistance of cement paste of the same mix due to insulating effect of coarse aggregates. Mathematical expressions were derived and used to exclude insulating effect of aggregates and to calculate corrected matrix-normalized conductivity values.

$$\frac{R_{DC}}{R_{AC}} = \frac{\sigma}{\sigma_m} = 1 + [\sigma]_{\infty,f}\,\varphi \qquad \textbf{(8.2)}$$

$$\frac{R_p}{R_{DC}} = \frac{\sigma_{DC}}{\sigma_m} = 1 + [\sigma]_{0,A}\varphi_A + [\sigma]_{0,f}\varphi_f \qquad \textbf{(8.3)}$$

$$\frac{R_p}{R_{AC}} = \frac{\sigma_{AC}}{\sigma_m} = 1 + [\sigma]_{0,A}\varphi_A + [\sigma]_{\infty,f}\varphi_f \qquad \textbf{(8.4)}$$

In these equations;

σ_{DC} : Conductivity of concrete matrix, 1/ohms

σ : Conductivity of composite, 1/ohms

σ_m : Conductivity of cement paste, 1/ohms

$[\sigma]_\Delta$: Intrinsic conductivity of fibers, (-)

$[\sigma]_{0,f}$: Intrinsic conductivity of fibers (under low AC frequencies - insulating case)

$[\sigma]_{\infty,f}$: Intrinsic conductivity of fibers (under high AC frequencies – conducting case)

$[\sigma]_{0,A}$: Intrinsic conductivity of aggregates

φ_A : Aggregate content, %

φ_f : Fiber content, %

$$\frac{\sigma}{\sigma_m} = \left(\frac{R_p}{R_{AC}} = \frac{\sigma_{AC}}{\sigma_m}\right) - \left(\frac{R_p}{R_{DC}} = \frac{\sigma_{DC}}{\sigma_m}\right) \approx [\sigma]_{\infty,f}\,\varphi_f \qquad \textbf{(8.5)}$$

Equation 8.2 gives general relation between matrix-normalized conductivity and intrinsic conductivity when perfectly conductive fibers are used in a moderately conductive cement paste matrix. When aggregates are present in composite material, composite matrix conductivity decreases due to insulating property of

aggregates. This results in an increase of calculated σ/σ_m value. Eqs. (8.3) and (8.4) are used so as to exclude insulating effect of aggregates and to obtain paste matrix-normalized conductivity values. In Eq. (8.3), the term $[\sigma]_{0,f}\ \varphi_f$ approaches 0 due to the fact that fibers are insulating under low frequencies of AC. The term $[\sigma]_{0,A}\ \varphi_A$ in both equations stands for the insulating effect of aggregates and the term $[\sigma]_{\infty,f}\ \varphi_f$ in Eq. (8.5) is for the case that the fibers are conducting (high AC frequencies). Equation (8.3) is subtracted from Eq. (8.4) to obtain Eq. (8.5). Eq. (8.5) gives the term "$[\sigma]_{\infty,f}\ \varphi_f$", which is needed to calculate paste matrix-normalized conductivity of the material.

Observed matrix-normalized conductivity values were corrected using Eq. (8.5) for all measurements and corrected values were used for evaluations. Table 8.6 shows observed and corrected matrix-normalized conductivity values together with theoretical (calculated) values for the mix design A_8. It should be noted that, this correction was not needed for the mixes with 40 mm fibers due to the small size of aggregates compared to the length of the fibers.

Table 8.6: Corrected matrix normalized conductivity values together with the observed and calculated values for mix design A_8

Fiber content, %	σ/σ_m (observed)	Theoretical (calculated)	σ/σ_m (corrected)
0.38	1.51	1.45	0.38
1.02	2.45	2.20	1.05
1.20	3.65	2.42	1.74
1.44	4.91	2.70	2.50

8.3.3 Mechanical tests

Splitting tensile tests were carried out on parts of the specimens as was defined in 8.2.3. Load-deflection curves were obtained and splitting tensile strengths were calculated. Figure 8.8 shows load vs. deflection curves for the specimen cast using mix design A_8.

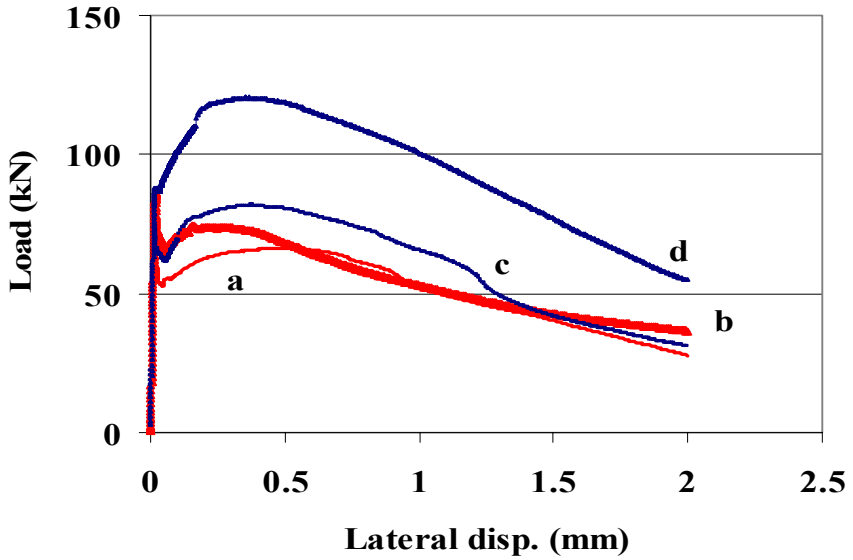

Figure 8.8: Load vs. lateral displacement curves for the specimen made with the design A_8

8.3.4 Comparison of test results

Data from fiber content calculation, AC-IS measurements and splitting tensile tests were plotted together to compare results obtained from 3 different methods. Figure 8.9 shows profiles for mix design A_8. Profiles for other concrete groups are given in appendix B. As seen in Figure 8.9, segregation of fibers can be predicted using AC-IS. Figure 8.9 also shows that the segregation of the fibers affects mechanical performance and causes non-homogenous material properties throughout the specimen. Similar tendencies were observed for all mix designs (Appendix B).

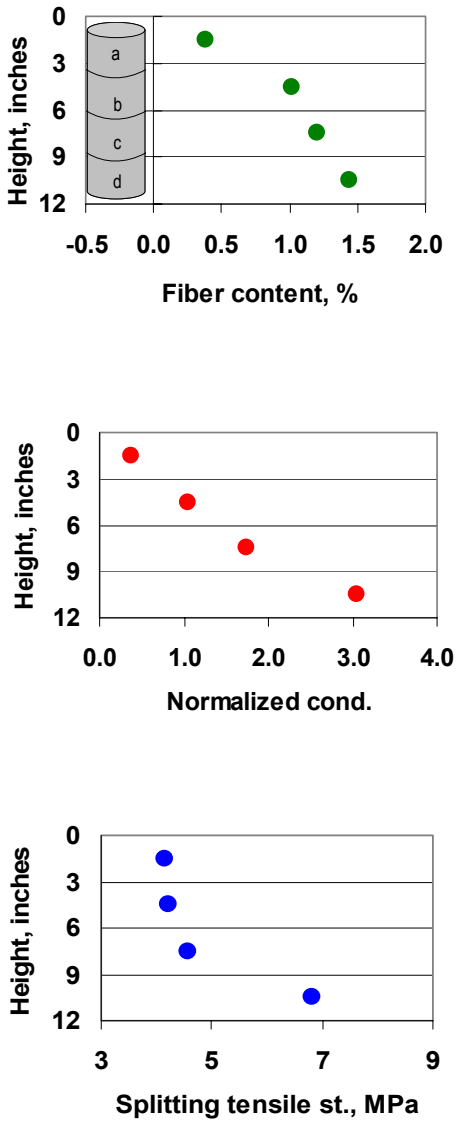

Figure 8.9: Fiber content, matrix-normalized conductivity and splitting tensile strength profiles of mix design A_8 (conventional concrete with sp and 6 mm fibers)

8.3.5 Rheology

Experiments were conducted on cement pastes of the mix designs to obtain rheological characteristics of mixes and to connect fresh and hardened state properties of FRCs by means of fiber dispersion. The rheological protocol which was given in section 6 was used and 3 repetitions were made for each mix. Shear stress and shear rate values were calculated from torque – rotation rate

measurements. Cement pastes showed Bingham behavior. Yield stress and viscosity values were obtained from Bingham plots as was defined in section 6.

8.4 Correlation of fiber dispersion, rheology and mechanical performance

Table 8.7 shows viscosity and yield stress values with standard deviations for all mixes. As seen in Table 8.7, viscosity and yield stress increases with addition of vma and the SCC mix has the lowest yield stress and highest viscosity.

Yield stress of design C was found to be lower than design B, while the viscosity is higher. This is due to the segregation preventing property of the vma used in this study. Kelcocrete 1376 is a viscosity modifier that is specifically designed to lower segregation of the ingredients in concrete by lowering yield stress while increasing viscosity.

Table 8.7: Rheological characteristics of cement pastes

		Mix Design	Viscosity (Pa*s)	Standard Dev. (Pa*s)	Yield stress (Pa)	Standard Dev. (Pa)
paste	sp	A	1.20	0.15	46.73	5.05
	sp+vma	B	3.52	0.18	110.65	2.31
	vma	C	5.45	0.29	76.73	2.07
	scc	SCC	7.22	0.51	19.48	2.80

Figure 8.10 represents viscosity – fiber segregation relation for mix designs A_8, B_8 and C_8. Standard deviation of fiber contents throughout the specimen was used as a representation of segregation. As seen in the figure viscosity increases with the addition of vma and segregation decreases.

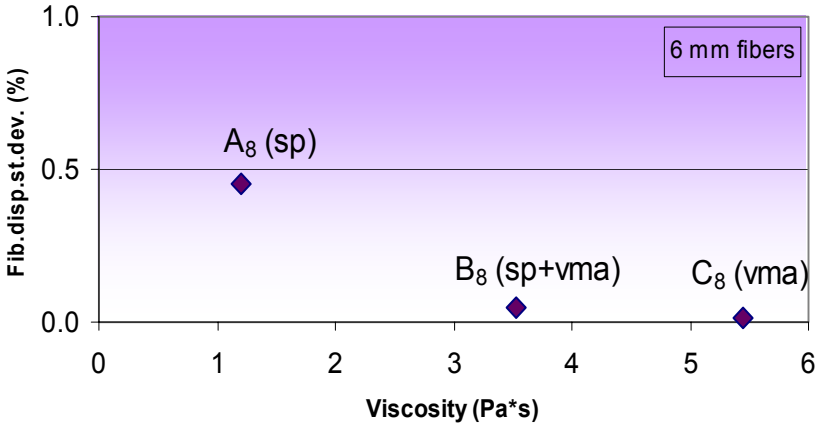

Figure 8.10: Standard deviation of fiber dispersion in the specimens vs. viscosity of cement pastes

Figure 8.11 represents yield stress – density relation for mix designs A_8, B_8 and C_8. As seen in the figure, yield stress increases with addition of vma and density decreases with increasing yield stress of cement pastes, meaning that vma designs in this study has a high segregation resistance due to high viscosity but low density/high pore volume due to high yield stress.

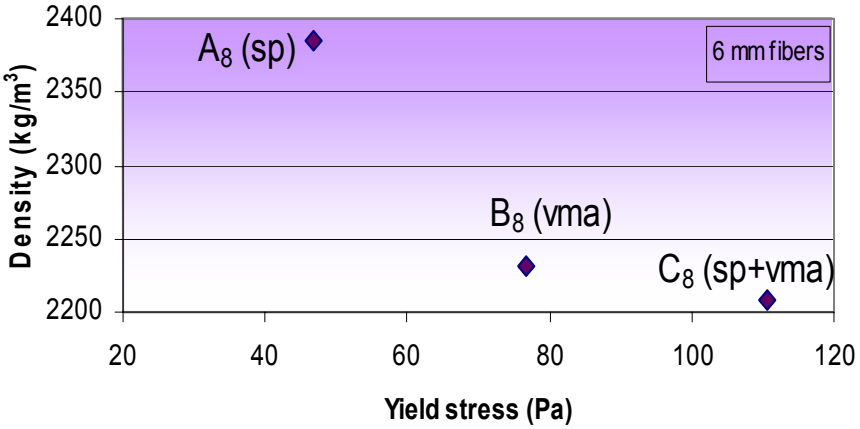

Figure 8.11: Standard deviation of fiber dispersion in the specimens vs. yield stress of cement pastes

Figure 8.12 and Figure 8.13 represent fiber segregation vs. viscosity and density vs. yield stress relations for conventional concrete and SCC. SCC designs are described with high viscosity and low yield stress. High viscosity ensures high segregation resistance and low yield stress provides good placeability. Figure

8.14 compares two conventional concrete specimens and an SCC specimen by means of surface quality/placeability. SCC specimen has no pores on the surface meaning a good placeability, while un-vibrated conventional concrete specimen has many visible pores. Vibrated conventional concrete specimen has also no pores on the surface, but severe segregation inside due to vibration as was shown in Figure 8.6. This means that the fresh state properties of SCC mixes are superior to those of conventional concretes.

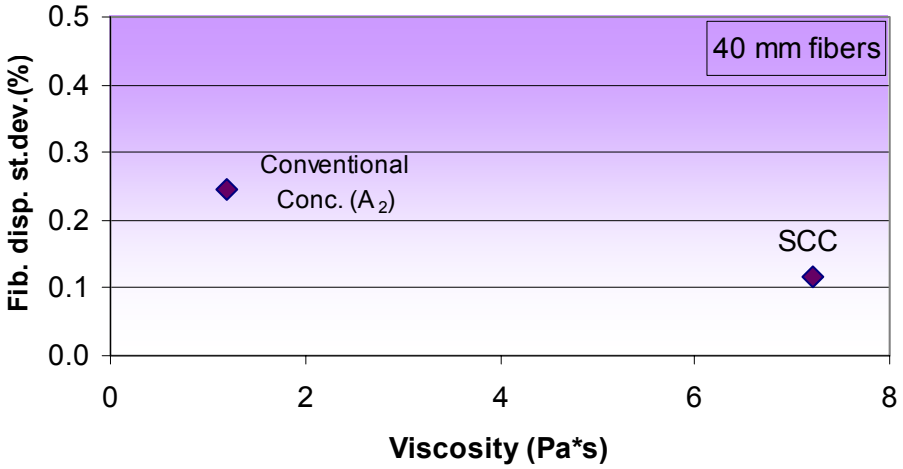

Figure 8.12: Standard deviation of fiber dispersion in the specimens vs. viscosity of conventional concrete and SCC

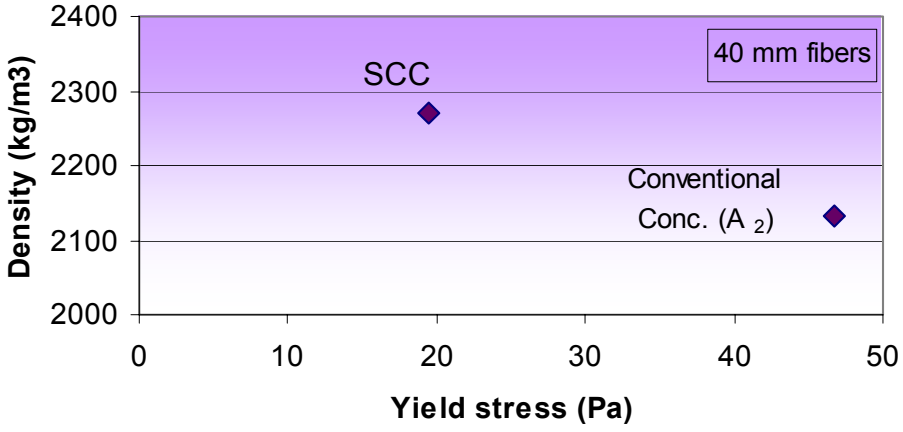

Figure 8.13: Density vs. yield stress of conventional concrete and SCC

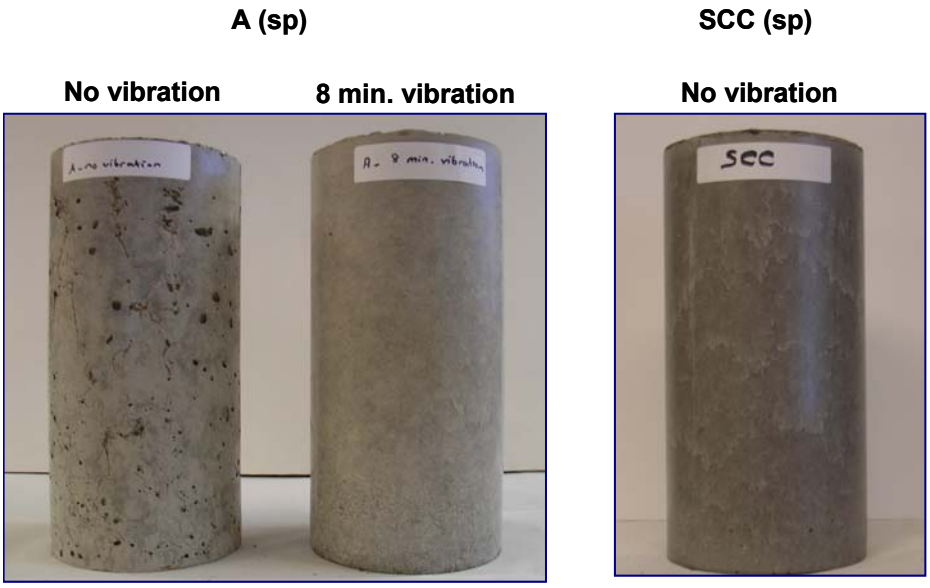

Figure 8.14: Surface properties of conventional concretes and SCC

8.5 Conclusions

Fresh and hardened state properties of FRC specimens were connected by means of fiber segregation. Both conventional concrete and SCC were cast using two types of fibers. The effect of vibration time on the segregation of fibers was investigated. Rheological characteristics of the mixes were measured using the parallel plate rheometer. AC-IS was used to monitor fiber segregation non-destructively.

Fresh state properties were found to affect segregation of fibers and mechanical performance of FRC. Conventional concrete designs and SCC were evaluated by means of fiber segregation. Segregation increased with increasing vibration time. SCC was found to be superior to conventional concrete with the features such as high segregation resistance and good placeability. Vma designs also had high segregation resistance but poor placeability/low mechanical performance. This result showed that fresh state properties strongly affect fiber dispersion and mechanical performance of FRCs. This study also showed that the fresh state properties and fiber dispersion can be successfully monitored using the self-designed parallel-plate rheometer and the AC-IS, respectively.

9. CONCLUSIONS AND FUTURE WORK

In this chapter, results of this thesis work are summarized and discussed. Some future work topics that can be investigated to better understand the subject are pointed out. The main objective of this study was to correlate fresh and hardened state properties of FRC materials by means of fiber dispersion. A comprehensive experimental work was conducted to characterize fiber dispersion and fresh state properties. AC-IS was employed for non-destructive monitoring of fiber dispersion and a new rheometer with a parallel-plate configuration was used to study fresh state properties of FRC materials.

9.1 Understanding the method

Fresh state and hardened state properties of FRC materials were studied by means of fiber dispersion. The use of AC-IS for non-destructive monitoring of fiber dispersion was analyzed. Comprehensive tests were conducted to understand the ability of AC-IS to detect various fiber dispersion issues, such as fiber orientation, fiber segregation and fiber clumping. From the results the following conclusions can be drawn:

- AC-IS is sensitive to any preferred alignment of fibers. By making 3-D measurements fractional intrinsic conductivities in reference directions can be obtained. Furthermore, by plotting the fractional intrinsic conductivities on a triangular plot, any deviation from a random distribution of fibers can be detected.
- Macro-scale segregation of fibers can be detected by a local probe, which can be scanned over the surface of a composite specimen. The probe registers “intrinsic conductivity” within a hemisphere of radius four times the radius of the probe. Intrinsic conductivity profiles can be used to describe macro-scale segregation.

- Micro-scale clumping may occur in FRC composites, especially when short fibers are used. By comparing averaged x, y, and z direction "intrinsic conductivities," with that predicted for a fully dispersed system, a "dispersion function" (DF) can be calculated. This provides a good indication of the degree of dispersion, with values near unity indicative of perfectly dispersed fibers, and values less than unity indicating a tendency for fiber clumping.
- Preliminary results of 2-point AC-IS on fresh FRC specimens suggest that the aforementioned AC-IS procedures for characterizing fiber dispersion in hardened FRCs can likewise be applied to the fresh state.

9.2 Comparative analysis

To understand the extent to which AC-IS predicts various fiber dispersion issues, image analyses were done on the specimens and the results of the two methods were compared. Fiber clumping and fiber orientation were characterized using the methods of the image analyses. Statistical point processes were employed to describe fiber clumping and second order orientation tensors for fiber orientation. AC-IS and image analysis results matched very well within experimental uncertainty. The two methods were compared by means of the measurement and data processing time as well as the damage made to the specimen under consideration. From the results the following conclusions can be drawn:

- AC-IS and image analysis give similar results, confirming the ability of AC-IS to detect various fiber dispersion issues.
- With AC-IS, it is possible to obtain general information about fiber dispersion by simply making 3-D measurements. On the other hand, a representative amount of cross-sections has to be analyzed for image analyses.
- Measurement and data processing is easier and faster with AC-IS than image analysis. Image analysis is also destructive, while no damage is made to specimen with AC-IS.

9.3 Large-scale application of AC-IS

Initial experiments provided detailed information about the use of AC-IS and the methods of evaluation. However, these experiments were on small lab-scale specimens. It was important to understand the ability of AC-IS for use on larger-scale FRC materials. For this purpose, a larger-scale application of AC-IS was done using a precast fiber-reinforced SCC beam, which was provided by a precast company. Comprehensive experiments were conducted on the beam. AC-IS measurements were obtained from the X and Z directions (Z direction is the casting direction). Matrix-normalized conductivity profiles were plotted for each direction and fiber orientation was evaluated by means of these profiles. Results suggest a preferred orientation of fibers in the plane that is perpendicular to the casting direction. This result was expected. The tendency of fibers to align perpendicular to the casting direction was reported by several other researchers in the literature. Image analysis was also conducted on several sections of the beam following AC-IS measurements. A straightforward image analysis method was used to characterize fiber orientation and the results of the two methods were compared. Splitting tensile tests and three-point bending tests were also performed to study the effects of fiber orientation on mechanical performance. Mechanical performance of the beam was found to be adversely affected by the preferred orientation of fibers. The following conclusions can be drawn from these results:

- AC-IS can be used to detect fiber dispersion issues in large-scale conductive FRC specimens.
- Preferred orientation of fibers results in non-homogenous material properties throughout a specimen. Therefore, the mechanical performance of composite materials can vary in different parts of the specimen.
- AC-IS shows considerable promise for use as a non-destructive and rapid method for fiber dispersion monitoring in industrial-scale FRC materials.

9.4 Fresh state properties of FRCs

Fiber dispersion is significantly affected by the fresh state properties of a composite. Therefore, an understanding of the fresh state properties is needed, so that fiber

dispersion can be controlled, which in turn provides a material with a better mechanical performance. Flow behavior is measured using rheometers. For this study, a new rheometer with a parallel plate configuration was designed and calibrated specifically for stiff fiber-reinforced cement-based materials. A plexi-glass wall was used to prevent test material from flowing away. The frictional effect of the wall was modeled. Results obtained with the new rheometer were verified using a standardized known-viscosity oil and by comparing measurements obtained with the parallel plate rheometer with those obtained using a commercial rheometer and values reported in the literature. The values measured using the new rheometer were within the same range as the values reported in the literature. Next, the effects of water-to-cement ratio, sand addition and fiber addition on the rheological characteristics were studied. Yield stress and viscosity decreased with increasing water-to-cement ratio and addition of sand, as was expected. On the other hand, unusual trends were observed with increasing fiber volume content. Generally, yield stress and viscosity are expected to increase with increasing fiber content. However, both parameters were found to decrease until a critical fiber volume was reached. Additional experiments, including drop table tests and tests on highly fluid materials and a Newtonian fluid (honey) were done to better understand the results obtained using the new rheometer. From these results, the following conclusions can be drawn:

- The new parallel-plate rheometer yields reasonable results. Measurements using the parallel plate rheometer fall within a reasonable range when compared with the values obtained from a commercial rheometer and those values reported in the literature.
- The frictional effect of the rheometer wall can be modeled using constitutive relations for the interfacial layer that forms between the wall and the bulk material. According to the resultant model, yield stress and viscosity values increase as the gap height increases.

- With stiff cementitious materials, high variations in yield stress and viscosity measurements are seen when vibration is not applied, most likely due to the uneven surfaces of the samples and the differing void contents. Repeatability

can be improved by applying vibration with normal compression to the sample before testing.

- For the steel fibers investigated, the Bingham rheological parameters decrease until a critical volume fraction is reached. This trend is explained by a coupling effect between the structural breakdown of the material, which occurs at low fiber volumes, and the mechanical interlocking of fiber, which occurs at higher volume fractions.

9.5 Correlation of fresh and hardened state properties by means of fiber dispersion

The effects of the fresh state properties on the fiber dispersion characteristics and mechanical performance of FRC materials are connected. The new rheometer was used to study fresh state properties of cement-based materials and AC-IS was employed to non-destructively study fiber segregation. Fiber segregation was also quantified in the fresh state by cutting the specimens into slices and washing the fibers out. Hardened state properties were studied by means of splitting tensile tests.

Fiber-reinforced concretes with various rheological properties were produced using different combinations of a superplasticizer (sp) and a viscosity modifying agent (vma). Different vibration times were applied to study the effects of vibration on the rheological parameters. The following conclusions can be drawn from the results:

- Vibration affects vertical distribution of fibers in FRC specimens. For the materials used in this study, the effect of vibration is more pronounced when longer fibers are used.

- The specimens containing using vma have a higher resistance to the segregation of fibers than the specimens with sp. However, the pore volume in these specimens is also higher, resulting in poor mechanical performance. The fresh state properties of these materials are described by a high yield stress and viscosity.

- SCC is more resistant to segregation than conventional concrete with fresh state characteristics that are described by a low yield stress and a high

viscosity. Low yield stress provides good placeability without vibration, while high viscosity ensures segregation resistance.

- Fresh state properties of FRC materials significantly affect fiber dispersion. Good dispersion of fibers and good mechanical performance can be made possible by controlling the fresh state properties.

- The custom designed and built parallel-plate rheometer, specifically designed for stiff FRC materials, was successfully used to describe flow behavior.

- This comprehensive experimental study made possible a better understanding of the use of AC-IS to monitor fiber dispersion characteristics and it was shown that AC-IS can be a good candidate to be used as a quality control method.

9.6 Future work

9.6.1 AC-IS

The use of AC-IS for fiber dispersion monitoring purposes is new and shows promise. The results of this study demonstrate that AC-IS can be an effective method for non-destructive and rapid monitoring of various fiber dispersion phenomena. Further research can be conducted to investigate the use of AC-IS when fiber type, size and shape vary. Specimen dimensions and fiber length/specimen size ratio are also important factors that should be studied. Research could also be conducted to further develop experimental set-ups for different fiber-matrix systems with various type/size/shape of fibers and various matrices.

9.6.2 Rheology

Recently, stiff FRC materials are increasingly employed in the civil engineering industry due to their superior properties by means of toughness, strength and durability. Hardened state properties of these materials are well investigated and extensive literature is available regarding the mechanical performance of these materials. Unfortunately, the fresh state properties are not well investigated and limited information is available in the literature. Developing a better understanding of the fresh state properties of stiff FRC materials was one of the major goals of this

thesis. A comprehensive study was conducted; remarkable results were found and reported. Only steel fibers were used in this study. Plastic fibers (for example; polypropylene, polyvinyl-alcohol) can be used in stiff cementitious matrices to investigate the effects of fiber type. Fiber shape and size can also be varied. Research can be conducted to relate the rheological parameters of FRC cement paste, to the FRC mortar and/or concrete.

REFERENCES

[1] **Balaguru, P.N. and Shah, S.P.**, 1992. Fiber-Reinforced Cement Composites. McGraw-Hill, New York.

[2] **Tasdemir, M.A. and Bayramov, F.**, 2002. Mechanical Behavior of High Performance Cement-Based Materials, *Istanbul Technical University Journal*, **1**, 125-144 (In Turkish).

[3] **Ozyurt, N., Ilki, A., Tasdemir, C., Tasdemir, M.A., and Yerlikaya, M.**, 2002. Mechanical Behavior of High Strength Steel Fiber Reinforced Concretes with Various Steel Fiber Contents, *Fifth International Congress on Advances in Civil Engineering*, Istanbul, Turkey, September 25-27, 885-894.

[4] **Nawy, E.G.**, 2001. Fundamentals of High-Performance Concrete. John Wiley & Sons, New York.

[5] **Shah, S.P., Sarigaphuti, M., and Karaguler, M.E.**, 1994. Comparison of Shrinkage Cracking Performance of Different Types of Fibers and Wiremesh, *Fiber Reinforced Concrete; Developments and Innovations*, Michigan, USA, 1-18.

[6] **Shah, S.P.**, 1991. Do Fibers Increase the Tensile Strength of Cement-Based Matrices?, *ACI Materials Journal*, **88**, 595-602.

[7] **Sun, W., Chen, H., Luo, X., and Qian, H.**, 2001. The Effect of Hybrid Fibers and Expansive Agent on the Shrinkage Permeability of High-Performance Concrete, *Cement and Concrete Research*, **31**, 595-601.

[8] **Banthia, N., Bindiganavile, V., and Mindess, S.**, 2003. Impact Resistance of Fiber-Reinforced Concrete: A Progress Report, *RILEM 4th International Workshop on High Performance Fiber-Reinforced Cement Composites (HPFRCC4)*, Ann Arbor, USA, June 15-18, 117-131.

[9] **Bayramov, F., Tasdemir, C., and Tasdemir, M.A.**, 2004. Optimisation of steel fibre reinforced concretes by means of statistical response surface method, *Cement and Concrete Composites*, **26**, 665-675.

[10] **Bentur, A.**, 1989, Fiber-Reinforced Cementitious Materials, in *Material Science of Concrete*, pp. 223-285, Ed. Skalny, J.P. The American Ceramic Society.

[11] **Mobasher, B., Stang, H., and Shah, S.P.**, 1990. Microcracking in Fiber-Reinforced Concrete, *Cement and Concrete Research*, **20**, 665-676.

[12] **Banthia, N., Moncef, A., Chokri, K., and Sheng, J.**, 1994. Micro Fiber-Reinforced Cement Composites, I. Uniaxial Tensile Response, *Canadian Journal of Civil Engineering*, **21**, 999-1011.

[13] **Ferraris, C.F.**, 1999. Measurement of the rheological properties of high performance concrete: state of the art report, *Journal of research of the national institute of standards and technology*, **104**, 461-478.

[14] **Naaman, A.E.**, 2003. Strain Hardening and Deflection Hardening Fiber Reinforced Cement Composites, *RILEM 4th International Workshop on High Performance Fiber Reinforced Cement Composites (HPFRCC4)*, Ann Arbor, USA., June 15-18, 95-113.

[15] **Chermant, J.L., Chermant, L., Coster, M., Dequiedt, A.S., and Redon, C.**, 2001. Some fields of applications of automatic image analysis in civil engineering, *Cement and Concrete Composites*, **23**, 157-169.

[16] **Yang, Y.**, 2002. Methods Study on Dispersion of Fibers in CFRC, *Cement and Concrete Research,*, **32**, 747-750.

[17] **Rapoport, R.J.**, 2002. Cellulose Fiber-Reinforced Cement Paste, Mortar, and Concrete, *PhD Thesis*, Northwestern University, Evanston, IL.

[18] **Akkaya, Y.**, 2000. Micro Structural Characterization of High Performance Fiber-Reinforced Cement Composites, *PhD Thesis*, Northwestern University, Evanston, IL.

[19] **Lawler, J.S.**, 2001. Hybrid fiber-reinforcement in mortar and concrete, *PhD Thesis*, Northwestern University, Evanston, IL.

[20] **Chung, D.D.L.**, 2000. Composite Materials for Electronic Functions, Trans Tech Publications, Zurich, Switzerland.

[21] **Chung, D.D.L.**, 2001. Applied Materials Science: Applications of Engineering Materials in Structural, Electronics, Thermal, and Other Industries, CRC Press, Boca Raton, FL.

[22] **Reza, F., Yamamuro, J.A., and Batson, G.B.**, 2004. Electrical Resistance Change in Compact Tension Specimens of Carbon Fiber Cement Compsites, *Cement and Concrete Composites*, **26**, 873-881.

[23] **Reza, F., Batson, G.B., Yamamuro, J.A., and Lee, J.S.**, 2003. Resistance Changes During Compression of Carbon Fiber Cement Composites, *Journal of Materials in Civil Engineering, ASCE*, **15**, 414-421.

[24] **Torrents, J.M., Mason, T.O., and Garboczi, E.J.**, 2000. Impedance Spectra of Fiber-Reinforced Cement-Based Composites, *Cement and Concrete Research*, **30**, 585-592.

[25] **Torrents, J.M., Mason, T.O., Peled, A., Shah, S.P., and Garboczi, E.J.**, 2001. Analysis of the Impedance Spectra of Short Conductive Fiber-Reinforced Composites, *Journal of Materials Science*, **36**, 4003-4012.

[26] **Christensen, B.J., Coverdale, R.T., Olson, R.A., Ford, S.J., Garboczi, E.J., Jennings, H.M., and Mason, T.O.**, 1994. Impedance Spectroscopy of Hydrating Cement-Based Materials: Measurement, Interpretation, and Application, *Journal of American Ceramic Society*, **77**, 2789-804.

[27] **Park, G., Cudney, H.H., and Inman, D.J.**, 2000. Impedance-based health monitoring of civil structural components, *Journal of Infrastructural Systems*, **6**, 153-160.

[28] **Dotelli, G. and Mari, C.M.**, 2001. The evolution of cement paste hydration process by impedance spectroscopy, *Materials Science and Engineering*, **A303**, 54-59.

[29] **Gu, P., Zhongzi, X., Xie, P., and Beaudoin, J.J.**, 1993. An A.C. Impedance spectroscopy study of micro-cracking in cement-based composites during compressive loading, *Cement and Concrete Research*, **23**, 675-682.

[30] **Peled, A., Torrents, J.M., Mason, T.O., Shah, S.P., and Garboczi, E.J.**, 2001. Electrical Impedance Spectra to Monitor Damage during Tensile Loading of Cement Composites, *ACI Materials Journal*, **98**, 313-322.

[31] **Stroeven, P. and Shah, S.P.**, 1978. Use of radiography - image analysis for steel fibre reinforced concrete, *RILEM Symposium 1978, Testing and Test Methods of Fibre Cement Composites*, New York, The University of Sheffield, England, April 5-7, 275-288.

[32] **Clarke, A. and Eberhardt, C.**, 1999. The representation of reinforcing fibres in composites as 3D space curves, *Composites Science and Technology*, **59**, 1227-1237.

[33] **Mlekusch, B.**, 1999. Fibre Orientation in Short-Fibre-Reinforced Thermoplastics. II. Quantitative Measurements by Image Analysis, *Composites Science and Technology*, **59**, 547-560.

[34] **Clarke, A.R. and Eberhardt, C.N.**, 2002. Microscopy Techniques for Materials Science, CRC Press LLC, Boca Raton.

[35] **Benson, S.D.P. and Karihaloo, B.L.**, 2003. CARDIFRC-Manifacture and constitutive behavior, *High Performance Fiber Reinforced Cement Composites (HPFRCC4)*, Ann Arbor, USA, June 15-18, 65-79.

[36] **Stroeven, P.**, 2000. Modelling of fibre dispersions in cementitious systems, *Fibre reinforced concretes, Fifth Rilem Symposium on Fibre - Reinforced Concretes*, Lyon, France, September 13-15, 419-428.

[37] **Mindess, S. and Young, J.F.**, 1981. Concrete. Prentice-Hall. Inc., Englewood Cliffs, NJ.

[38] **Mott, R.L.**, 2000. Applied Fluid Mechanics. Prentice-Hall, Inc., New Jersey.

[39] **Hackley, V.A. and Ferraris, C.F.**, 2001. Guide to Rheological Nomenclature: Measurements in Ceramic Particulate Systems, *NIST Special Publication 946*, U.S. Department of Commerce.

[40] **Geiker, M.L., Brandl, M., Thrane, L.N., Bager, D.H., and Wallevik, O.**, 2002. The Effect of Measuring Procedure on the Apparent Rheological Properties of Self-Compacting Concrete, *Cement and Concrete Research*, **32**, 1791-1795.

[41] **de Larrard, F., Ferraris, C.F., and Sedran, T.**, 1998. Fresh concrete: a herschel bulkley-material, *Materials and Structures*, **31**, 494-498.

[42] **Atzeni, C., Massidda, L., and Sanna, U.**, 1985. Comparison between rheological models for portland cement pastes, *Cement and Concrete Research*, **15**, 511-519.

[43] **Macosko, C.W.**, 1994. Rheology, Principles, Measurements, and Applications, Wiley-VCH, Inc., Canada.

[44] **Barnes, H.A., Hutton, J.F., and Walters, K.**, 1989. An Introduction to Rheology, Elsevier, Amsterdam.

[45] **Wallevik, O.H. and Gjorv, O.E.**, 1990. Development of Coaxial Cylinder Viscometer for Fresh Concrete, *Properties of Concrete, Proceeding of the RILEM Colloquium*, Hanover, October 1990, 213-224.

[46] **Coussor, P.**, 1993. Rheologie des boues et laves torrentielles - Etudes de dispersions et suspensions concentrees, *These de doctorat* de l'institut National Polytechnique de Grenoble, et Etudes du Cemagref. serie Montagne n5, Grenoble.

[47] **de Larrard, F., Hu, C., Sedran, T., Szitkar, J.C., Joly, M., Claux, F., and Derkx, F.**, 1997. A New Rheometer for Soft-to-Fluid Fresh Concrete, *ACI Materials Journal*, **94**, 234-243.

[48] **Struble, L.J., Puri, U., and Ji, X.**, 2001. Concrete Rheometer, *Advances in Cement Research*, **13**, 53-63.

[49] **Hu, C., de Larrard, F., Sedran, T., Boulay, C., Bosc, F., and Deflorenne, F.,** 1996. Validation of BTRHEOM, the New Rheometer for Soft-to-fluid Concrete, *Materials and Structures*, **29**, 620-631.

[50] **Beaupre, D.**, 1994. Rheology of High Performance Shotcrete, *PhD Thesis*, University of British Columbia, Canada.

[51] **Tatersall, G.H. and Bloomer, S.J.**, 1979. Further Development of the Two-Point test for Workability and Extension of Its Range, *Magazine of Concrete Research*, **31**, 202-210.

[52] **Li, V.C.**, 2000. Large Volume, High-Performance Applications of Fibers in Civil Engineering, *Journal of Applied Polymer Science*, **83**, 660-686.

[53] **Douglas, J.F. and Garboczi, E.J.**, 1995. Intrinsic Viscosity and the Polarizability of Particles Having a Wide Range of Shapes, in *Advances in Chemical Physics* Vol. XCI, Eds. Prigogine, I., & Rice, S.A., pp. 85-153, John Wiley & Sons., New York.

[54] **Johnson, D.H.**, 2001. Origins of the Equivalent Circuit Concept, *Proceedings of the IEEE,* **91***, 636-640.*

[55] **Woo, L.Y., Wansom, S., Hixson, A.D., Campo, M.A., and Mason, T.O.**, 2003. A Universal Equivalent Circuit Model for the Impedance Response of Composites, *Journal of Materials Science,* **38**, 2265-70.

[56] **Boukamp, B.A.**, 1990, Equivalent Circuit (EQUIVCRT.PAS), Netherlands.

[57] **Woo, L.Y.**, 2005. Characterizing fiber-reinforced composite structures using AC-Impedance Spectroscopy (AC-IS), *PhD Thesis,* Northwestern University, Evanston, IL.

[58] **Ozyurt, N., Woo, L.Y., Mu, B., Shah, S.P., and Mason, T.O.**, 2004. Detection of Fiber Dispersion in Fresh and Hardened Cement Composites, *Advances in Concrete Through Science and Engineering, An International Symposium During the RILEM Spring Meeting*, Northwestern University, Evanston, Illinois, March 21-24, on CD-ROM.

[59] **Woo, L.Y., Wansom, S., Ozyurt, N., Mu, B., Shah, S.P., and Mason, T.O.**, 2005. Characterizing Fiber Dispersion in Cement Composites Using AC-Impedance Spectroscopy, *Cement and Concrete Composites*, **27**, 627-636.

[60] **Akkaya, Y., Picka, J., and Shah, S.P.**, 2000. Spatial Distribution of Aligned Short Fibers in Cement Composites, *Journal of Materials in Civil Engineering*, **12**, 272.

[61] **Fleig, J. and Maier, J.**, 1996a. Finite Element Calculations of Impedance Effects at Point Contacts, *Electrochimica Acta*, **41**, 1003-1009.

[62] **Fleig, J. and Maier, J.**, 1996. Surface Conductivity Measurements on AgCl Single Crystals Using Microeletrodes, *Berichte der Bunsen-Gesellschaft-Physical Chemistry Chemical Physics*, **100**, 607-615.

[63] **Newman, J.**, 1966. Resistance for Flow of Current to a Disk, *Journal of the Electrochemical Society*, **113**, 501-502.

[64] **Bay, R.S. and Tucker III, C.L.**, 1992. Stereological Measurement and Error Estimates for Three-Dimensional Fiber Orientation, *Polymer Engineering and Science*, **32**, 240-253.

[65] **Diggle, P.J.**, 1983. Statistical Analysis of Spatial Point Patterns. Academic Press Inc., London.

[66] **Akkaya, Y.**, 2000. Micro structural characterization of high performance fiber reinforced cement composites,, *PhD Thesis*, Northwestern University, Evanston, IL.

[67] **Advani, S.G. and Tucker III, C.L.**, 1987. The Use of Tensors to Describe and Predict Fiber Orientation in Short Fiber Composites, *Journal of Rheology*, **31**, 751-784.

[68] **Eberhardt, C. and Clarke, A.**, 2001. Fibre-Orientation Measurements in Short-Glass-Fibre Composites. Part I: Automated, High Angular-Resolution Measurement by Confocal Microscopy, *Composites Science and Technology*, **61**, 1389-1400.

[69] **Zhu, Y.T., Blumenthal, W.R., and Lowe, T.C.**, 1997. Determination of Non-Symmetric 3-D Fiber Orientation Distribution and Average Fiber Length in Short-Fiber Composites, *Journal of Composite Materials*, **31**, 1287-1301.

[70] **Grunewald, S. and Walraven, J.C.**, 2004. "Case Studies with Self-Compacting Steel Fiber Reinforced Concrete," *Concrete Plant + Precast Technology (BFT)*, **70**, 18-27.

[71] **Krenchel, H.**, 1975. Fibre Spacing and Specific Fibre Surface, *RILEM, Symposium on Fibre Reinforced Cement and Concrete*, Lancaster, England, September 14-17, 69-79.

[72] **Kuder, K.G., Ozyurt, N., Mu, B., and Shah, S.P.**, 2004. The Rheology of Fiber-Reinforced Cement Paste Evaluated by a Parallel Plate Rheometer, *Advances in Concrete Through Science and Engineering*, Northwestern University, Evanston, IL, March 21-24, on CD-ROM.

[73] **Bird, R.B., Armstrong, R.C., and Hassager, O.**, 1987. Dynamics of Polymeric Liquids. John Wiley and Sons, New York.

[74] **Browne, R. and Bamforth, P.**, 1977. Tests to Establish Concrete Pumpability, *ACI Materials Journal*, **74**, 4-19.

[75] **Geiker, M.R., Brandl, M., Thrane, L.N., Bager, D.H., and Wallevik, J.**, 2002. The Effect of Measuring Procedure on the Apparent Rheological Properties of Self-Compacting Concrete, *Cement and Concrete Research*, **32**, 1791-1795.

[76] **Banfill, P.F.G.**, 2003. The Rheology of Fresh Cement and Concrete - A Review, *11th International Cement Chemistry Congress*, Durban, South Africa, May 11-16, 50-62.

[77] **Saak, A.W., Jennings, H.M., and Shah, S.P.**, 2001. The Influence of Wall Slip on Yield Stress and Viscoelastic Measurements of Cement Paste, *Cement and Concrete Research*, **31**, 205-212.

[78] **Yahia, A. and Khayat, K.H.**, 2003. Applicability of Rheological Models to High-Performance Grouts Containing Supplementary Cementitious Materials and Viscosity Enhancing Admixture, *Materials and Structures*, **36**, 402-412.

[79] **Lapasin, R., Papo, A., and Rajgelj, S.**, 1983. Flow Behavior of Fresh Cement Pastes: A Comparison of Different Rheological Instruments and Techniques, *Cement and Concrete Research*, **13**, 349-356.

[80] **Bui, V.K., Geiker, M.R., and Shah, S.P.**, 2003. Rheology of Fiber-Reinforced Cementitious Materials, *High Performance Fiber-Reinforced Cement Composites (HPFRCC4)*, Ann Arbor, MI, USA, June 15-18, 221-231.

[81] **Wallevik, O.H. and Gjorv, O.E.**, 1990. Development of coaxial cylinder viscometer for fresh concrete in *Properties of Concrete,* pp.213-224 Ed. Wierig, H.-J., Chapman and Hall, Hanover.

[82] **Banfill, P.F.G., Beaupre, D., Chapdelaine, F., de Larrad, F., Domone, P., Nachbaur, L., Sedran, T., Wallevik, O.H., and Wallevik, J.**, 2000, Comparison of concrete rheometers: International tests at LCPC (Nantes, France), *NIST Technical Report*, **NISTIR 6819**, National Institute of Standards and Technology, Gaithersburg, USA.

[83] **Tattersall, G.H. and Banfill, P.F.G.**, 1983. The Rheology of Fresh Concrete. Pittman, London.

[84] **ASTM C109-99**, 2000. Standard Test Method for Compressive Strength of Hydraulic Cement Mortars (Using 20in. or 50 mm Cube Specimens), *Annual Book of ASTM Standards*.

[85] **Sundararajakumar, P.R. and Koch, D.L.**, 1997. Structure and Properties of Sheared Fiber Suspensions with Mechanical Contacts, *Journal of Non-Newtonian Fluid Mechanics*, **73**, 205-239.

APPENDIX A

Fortran routine for calculation of $\hat{K}_E(r)$

```
C       PROGRAM DISTANCE
      DIMENSION X(8000),Y(8000),FN(8000),angle(8000)
      REAL angle
      REAL R
           REAL a
           REAL b
           REAL c
           REAL G
           REAl Q
           REAL k
           REAL l
      REAL n
           REAL m
      REAL F
           OPEN(20,FILE='e:413veri.txt',status='old')
           REWIND(20)
           OPEN(unit=30,FILE='e:1-413kisotropysonucQ60.txt',STATUS='new')
C
      I=0
1     read(20,*,END=5)XX,YY
      I=I+1
      X(I)=XX
      Y(I)=YY
      GOTO1
```

```
5       NOF=I
        do 2 i=1,NOF
        R=2.
C       a - x ve y icin alt kenar lifler siniri
C       b - x icin ust kenar lifler siniri
C       c - y icin ust kenar lifler siniri
        a=2.
        b=86.5
        c=86.
        G=1.571
        Q=1.047
        F=0.
        k=G-Q
        l=G+Q
        n=G-Q+3.14159
        m=G+Q+3.14159
C
    do 3 j=1,NOF
        if(i.eq.j) go to 3
        if(X(I).le.a) go to 3
        if(X(I).gt.b) go to 3
        if(Y(I).le.a) go to 3
        if(Y(I).gt.c) go to 3
C
        Dist=SQRT((x(i)-x(j))**2+(y(i)-y(j))**2)
        if(dist.gt.R) go to 3
        angle(I)=atan((y(i)-y(j))/(x(i)-x(j)))
        if(x(i).eq.x(j).and.y(i).eq.y(j)) angle(I)=0
        if(x(i).eq.x(j).and.y(i).lt.y(j)) angle(I)=1.5707
        if(x(i).eq.x(j).and.y(i).gt.y(j)) angle(I)=4.7123
```

```
        if(y(i).eq.y(j).and.x(i).gt.x(j)) angle(I)=angle(I)+3.14159
        if(y(i).eq.y(j).and.x(i).lt.x(j)) angle(I)=0
       if(y(i).lt.y(j).and.x(i).gt.x(j)) angle(I)=angle(I)+3.14159
       if(y(i).gt.y(j).and.x(i).lt.x(j)) angle(I)=angle(I)+6.28318
       if(y(i).gt.y(j).and.x(i).gt.x(j)) angle(I)=angle(I)+3.14159
        if(angle(I).lt.k) go to 3
        if(angle(I).gt.m) go to 3
        if((angle(I).gt.l).and.(angle(I).lt.n)) go to 3

        if(dist.le.R)F=F+1
3       continue

    FN(I)=F
    WRITE(*,*)I,FN(I)
2   continue
    WRITE(30,4)(FN(I),I=1,NOF)
4       FORMAT(F 8.1)
       STOP
    END
```

Fortran routine for calculation of *K* function

```
C       PROGRAM DISTANCE
      DIMENSION X(5000),Y(5000),FN(5000)
      REAL R
           REAL a
           REAL b
           REAL c
      REAL F
           OPEN(20,FILE='g:797kfuncrandom1932.txt',status='old')
           REWIND(20)
           OPEN(unit=30,FILE='g:1-797kfuncsonucrand2mm.txt',STATUS='new')
C
      I=0
1     read(20,*,END=5)XX,YY
      I=I+1
      X(I)=XX
      Y(I)=YY
      GOTO 1
5          NOF=I
      do 2 i=1,NOF
           R=2.
C          a - x ve y icin alt kenar lifler siniri
C          b - x icin ust kenar lifler siniri
C          c - y icin ust kenar lifler siniri
           a=2.
           b=81.9
           c=82.
           F=0.
```

```
C
      do 3 j=1,NOF
         if(i.eq.j) go to 3
         if(X(I).le.a) go to 3
         if(X(I).gt.b) go to 3
         if(Y(I).le.a) go to 3
         if(Y(I).gt.c) go to 3
C
         Dist=SQRT((x(i)-x(j))**2+(y(i)-y(j))**2)
         if(dist.gt.R) go to 3
         if(dist.le.R)F=F+1
3     continue

      FN(I)=F
      WRITE(*,*)I,FN(I)
2     continue
       WRITE(30,4)(FN(I),I=1,NOF)
4      FORMAT(F 8.1)
       STOP
       END
```

APPENDIX B

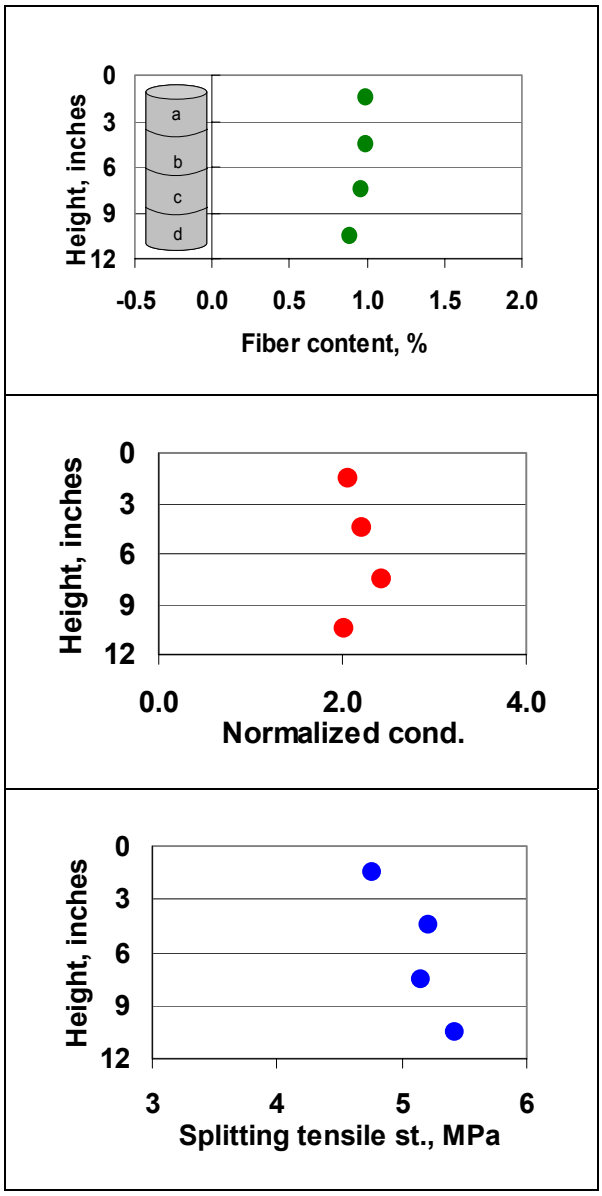

Figure B.1: Fiber content, matrix-normalized conductivity and tensile strength profiles for the design A_0

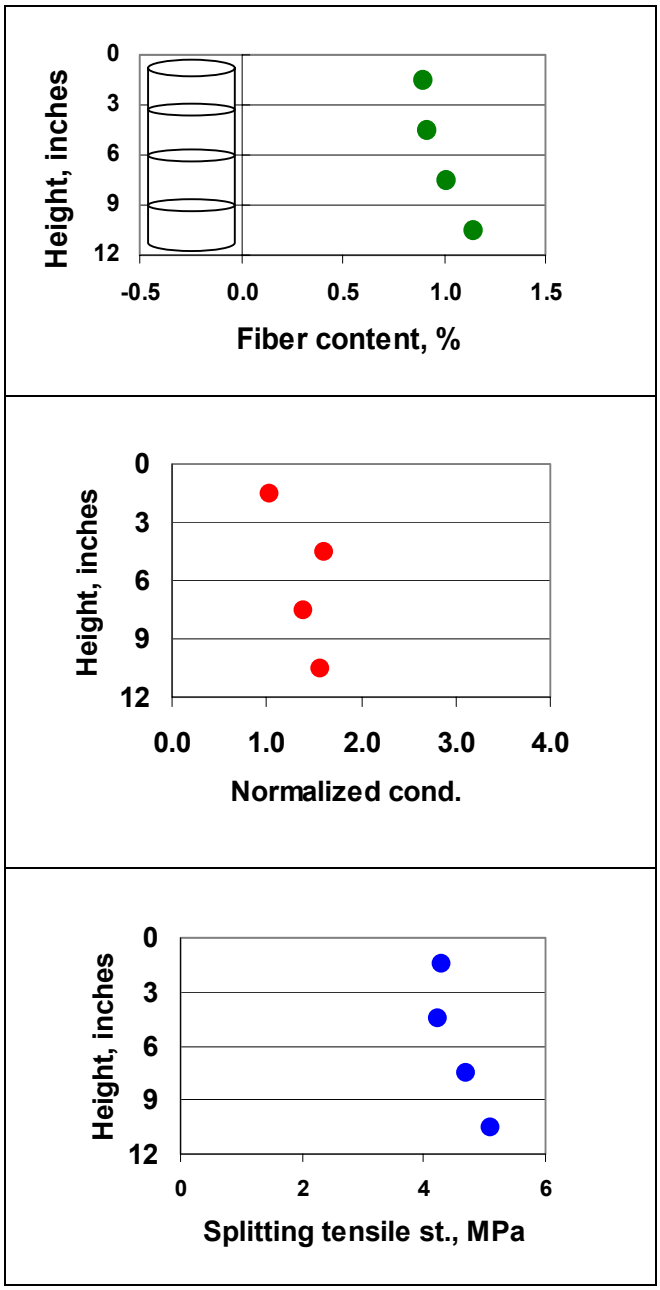

Figure B.2: Fiber content, matrix-normalized conductivity and tensile strength profiles for the design A_2 (6mm fibers)

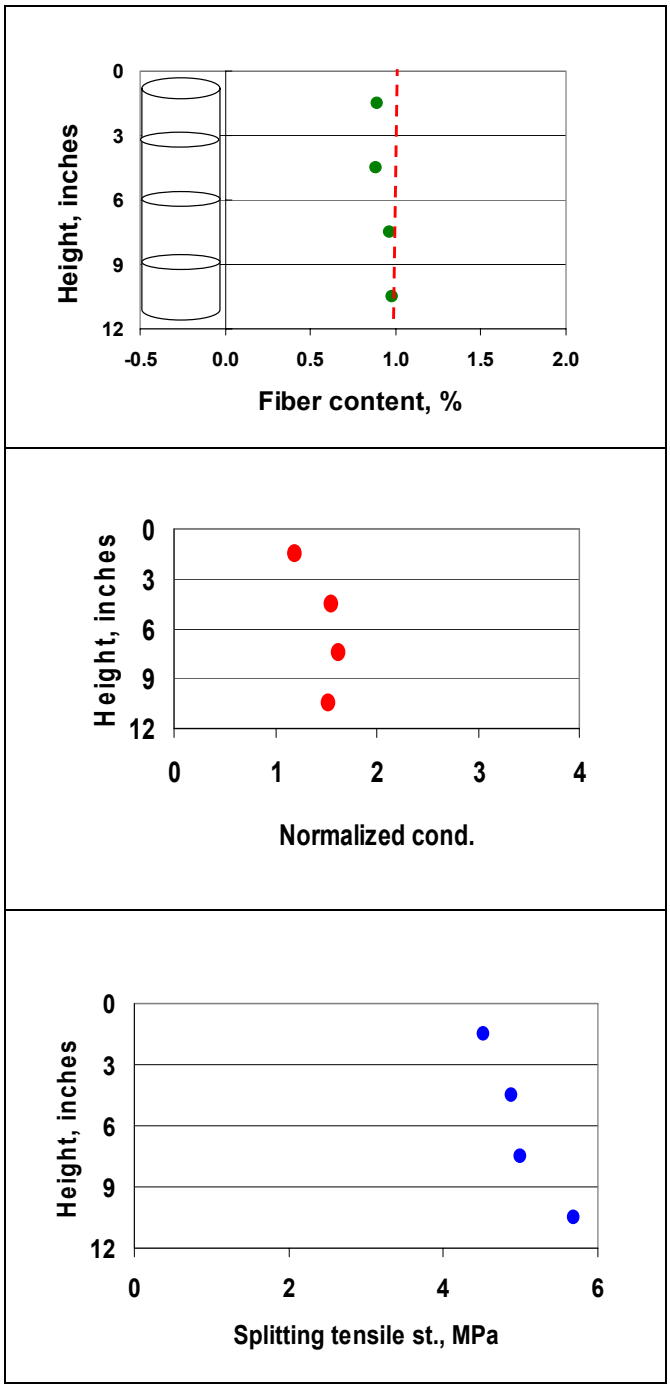

Figure B.3: Fiber content, matrix-normalized conductivity and tensile strength profiles for the design B_8

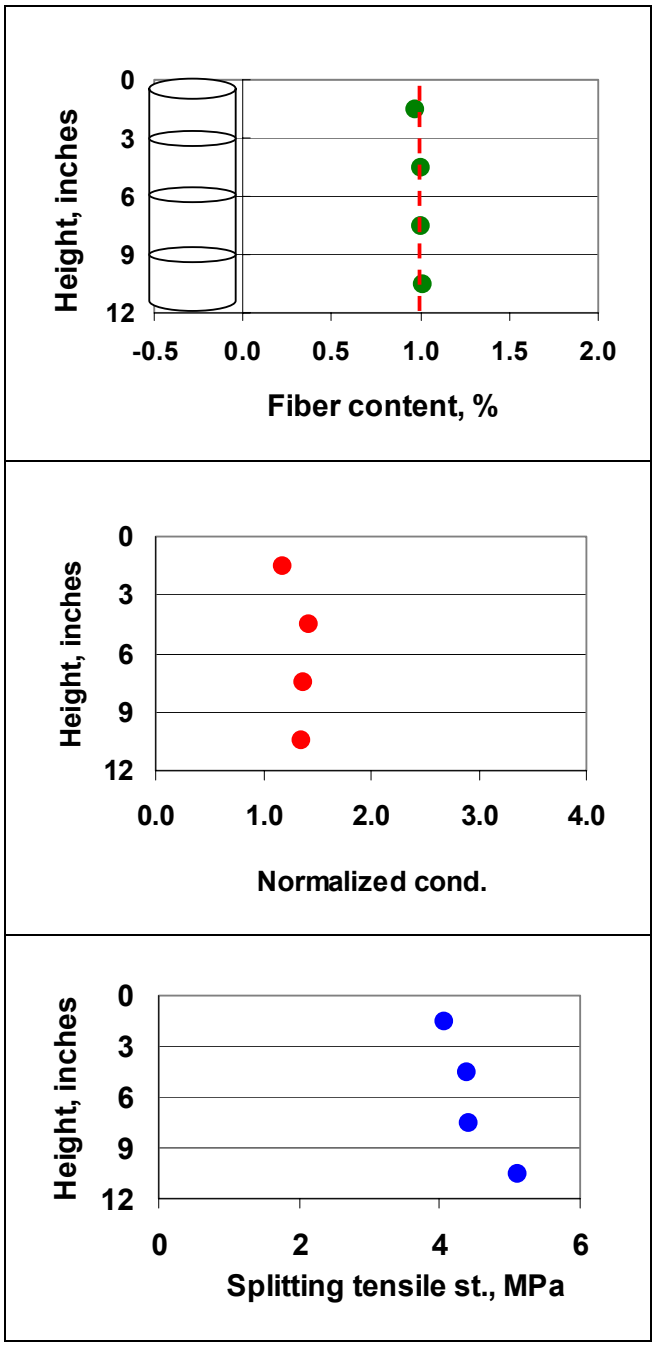

Figure B.4: Fiber content, matrix-normalized conductivity and tensile strength profiles for the design C_8

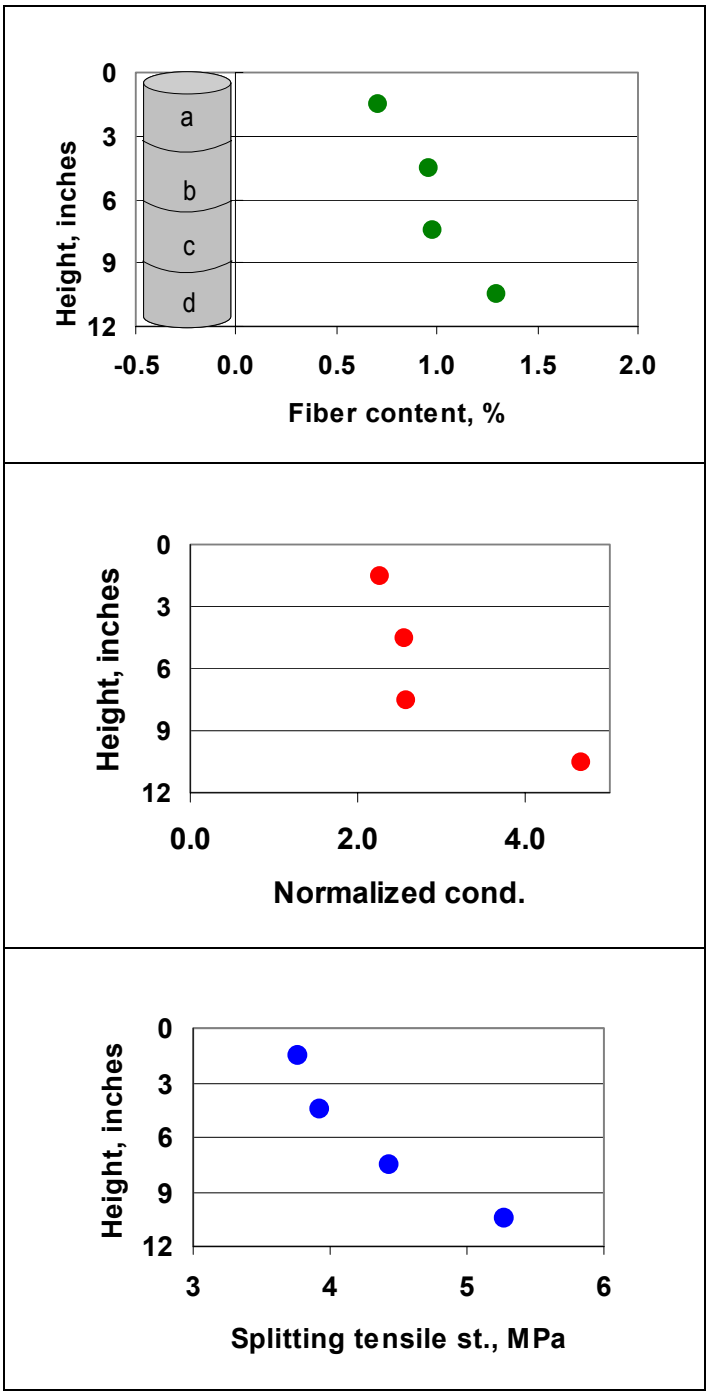

Figure B.5: Fiber content, matrix-normalized conductivity and tensile strength profiles for the design A_2 (40mm fibers)

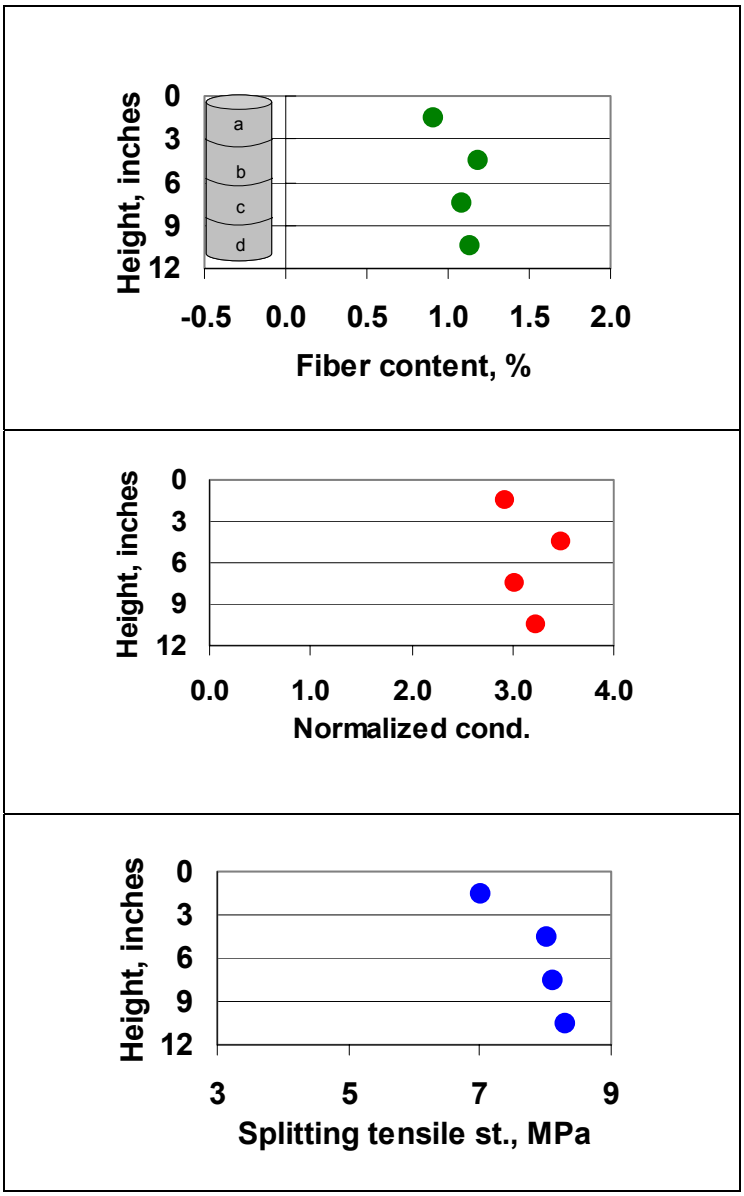

Figure B.6: Fiber content, matrix-normalized conductivity and tensile strength profiles for SCC

CURRICULUM VITAE

Nilüfer Özyurt was born in İstanbul in 1976. She graduated from İstanbul Technical University in 1998. She received her MSc. in structural materials in 2000 and started her PhD at İstanbul Technical University. She has been working as a research assistant in İstanbul Technical University Structural Materials Department since November 1999. She has also worked in the Center for Advanced Cement-Based Materials (ACBM) at Northwestern University as a pre-doctoral fellow between 2003-2005. She was awarded several grants during her PhD including TÜBİTAK (The Scientific and Technological Research Council of Turkey) NATO grant, and fellowships from İstanbul Technical University, Northwestern University and Tinçel Cultural Foundation. Her research interests include fiber-reinforcement and fiber dispersion in fiber-reinforced cement-based materials, rheology of stiff cementitious materials, non-destructive testing and high performance cement-based materials.

Publications

Papers in refereed journals:

Ozyurt, N., Mason, T.O., Shah, S.P., "Correlation of Fiber Dispersion, Rheology and Mechanical Performance of FRCs", Submitted to Cement and Concrete Composites, 2006.

Özyurt, N., Mason, T.O., Shah, S.P., "Non-Destructive Monitoring of Fiber Orientation using AC-IS: An Industrial Scale Application", Accepted for publication, February 2006.

Kuder, K., **Özyurt, N.**, Mu, B., Shah, S.P., "Rheology of Fiber-Reinforced Cementitious Materials", Submitted to Cement and Concrete Research, 2005.

Özyurt, N., Woo, L.Y., Mason, T.O., Shah, S.P., "Monitoring Fiber Dispersion in FRCs: Comparison of AC-Impedance Spectroscopy and Image Analysis", Accepted for publication, November 2005.

Woo, L.Y., Wansom, S., **Özyurt, N**., Mu, B., Shah, S.P., Mason, T.O., "Characterizing Fiber Dispersion in Cement Composites using AC-Impedance Spectroscopy", *Cement and Concrete Composites*, Vol. 27, No. 6, pp. 627-636, July 2005.

Atahan, H.N., Taşdemir, M.A., Taşdemir, C., **Özyurt, N**., Akyüz, S. "Mode I and Mixed Mode Fracture Studies in High Strength Mortar Using Disc Specimens", Materials and Structures, Vol. 38, No. 277, pp. 305-312, 2005.

Papers in International Conferences:

Woo, L.Y., Wansom, S., Mason, T.O., **Özyurt, N**., Mu, B., and S. P. Shah, "AC Impedance Spectroscopy for Nondestructive Evaluation of Fiber-Reinforced Cement Composites", Third International Conference on Construction Materials: Performance, Innovations and Structural Implications, Vancouver, Canada, August 22-24, 2005.

Özyurt, N., Woo, L.Y., Mu, B., Shah, S.P., Mason, T.O., "Detection of Fiber Dispersion in Fresh and Hardened Cement Composites", International Symposium: Advances in Concrete through Science and Engineering, (RILEM), Evanston, IL, March 21-24, 2004.

Kuder, K., **Özyurt, N.**, Mu, B., Shah, S.P., "The Rheology of Fiber-Reinforced Cement Paste Evaluated by a Parallel Plate Rheometer", International Symposium: Advances in Concrete through Science and Engineering, (RILEM), Evanston, IL, March 21-24, 2004.

Özyurt, N., İlki, A., Taşdemir, C., Taşdemir, M.A., "Mechanical Behavior of High Strength Steel Fiber Reinforced Concretes with Various Steel Fiber Contents", Fifth International Congress on Advances in Civil Engineering, September 25-27, 2002, Istanbul, Turkey.

Atahan, H.N., Tasdemir, M.A., Tasdemir, C., **Özyurt, N.**, Akyuz, S. "Fracture Studies in Reactive Powder Concrete" Second International Symposium on Cement and Concrete Technology in the 2000 s, September 6-10, 2000, İstanbul, Turkey, Volume 2, pp. 191-200.

Papers in National Conferences (in Turkish with English abstract):

Taşdemir, C., **Özyurt, N.**, Ertuğrul, C. ve Kara, G., "An Evaluation of the Effects of Crushed-Sand on the Concrete Properties", Chamber of Mining Engineers of Turkey, 3rd National Symposium on Crushed Stone", December 3-4, 2003 İstanbul.

Özyurt, N., Taşdemir, C., Kara, G. ve Ertuğrul, C., "The Effects of Crushed Sand Content on the Fly Ash Concrete Properties", Turkish Chamber of Civil Engineers, Istanbul, 5th National Symposium on Concrete, October 1-3, 2003, İstanbul, pp.293-301.

Akman, M.S., **Özyurt, N.**, "Effects of Sea Water on Concrete Impermeability of Shore Structures" IVth National Symposium of Shore Engineering, October 24-27, 2002, Antalya, Turkey, Volume1. pp. 3-18.

Konuk, H., **Özyurt, N.**, Taşdemir, C., Yüceer Z., Sönmez, R., "Load-bearing Properties of Lightweight Aggregate Concrete", Ith National Congress and Exhibition of Structural Materials, October 9-13, 2002, İstanbul, Turkey, Volume2. pp. 414-424.

Özyurt, N., Taşdemir, C., İlki, A., Şengul, Ö., Taşdemir, M.A., "Mechanical Behaviour of High Strength Cement Based Composites" XI.th National Mechanics Congress, September 6-10, 1999, Bolu, Turkey, pp. 687-696.